Viewing paleontology through a geochemical lens: 2 case studies

by

Brendan M. Anderson

B.A., Dartmouth College, 2009

Submitted to the Department of Geology

and the faculty of the Graduate School of The University of Kansas

in partial fulfillment of the requirements for the degree of

Master of Science

2013

Advisory Committee:

_____

Alison Olcott Marshall, Chair

_____

Craig P. Marshall

_____

Bruce S. Lieberman

_____

Randy Stotler

Date Defended: _____5/28/2013_____

The Thesis Committee for Brendan Matthew Anderson certifies that this is the approved version of the following thesis:

Viewing paleontology through a geochemical lens: 2 case studies

Advisory Committee:

_____
Alison Olcott Marshall, Chair

_____
Craig P. Marshall

_____
Bruce S. Lieberman

_____
Randy Stotler

Date Approved: 6/5/2013

Abstract

Geochemistry has become increasingly important to the field of paleontology. This thesis comprises two geochemical case studies examining questions at very different scales. The first examines possible controls on the formation of deposits where exceptional preservation of non-biomineralized tissues occurs throughout the Phanerozoic by the creation and analysis of a database of Phanerozoic *Konservat-Lagerstätten*. Potential controls examined include the influence of marine geochemistry, the availability of fossiliferous strata and evolutionary events. The second case study involves the application of Raman microspectroscopy in pathology and paleopathology. Raman microspectroscopy is used to demonstrate biotic origin for a new type of trace fossil, and to study the mineralogical changes that occur in bone presenting with osteomyelitis and hyperplastic bone marrow disease.

Table of Contents

Chapter 1

Introduction

Paleontology is an inherently multidisciplinary field, integrating both biological and geological information. Advances in geochemical techniques, as well as computing power, have allowed a variety of new questions to be answered respecting such diverse areas as mass extinctions, paleoecology, taphonomy and paleopathology. Analysis of large datasets, such as Macrostrat, containing over 21,000 North American Rock units (Peters and Gaines, 2012) and the Paleobiology Database (PaleoDB; http://Paleodb.org), containing over 1 million fossil occurrences (pbdb.org) and increased application of geochemical techniques, such stable isotope and biomarker analyses and the application of Raman spectroscopy, have provided new insights and generated new research questions in modern paleontology.

This thesis comprises two case studies examining questions at very different scales. The first examines possible controls on the formation of deposits where exceptional preservation of non-biomineralized tissues occurs throughout the Phanerozoic by the creation and analysis of a database of Phanerozoic *Konservat-Lagerstätten*. Potential controls examined include the influence of marine geochemistry, the availability of fossiliferous strata and evolutionary events. The second case study involves the application of Raman microspectroscopy in pathology and paleopathology. Raman microspectroscopy is used to demonstrate biotic origin for a new type of trace fossil, and to study the mineralogical changes that occur in bone presenting with osteomyelitis and hyperplastic bone marrow disease.

1. Database Techniques

Databases have been particularly important for recognizing patterns in paleodiversity. Sepkoski's 1981 figure depicting total familial marine diversity throughout the Phanerozoic

parsed into three evolutionary faunas may be the most reproduced figure in the history of Paleontology (Briggs and Crowther, 2003). In considering the biological veracity of the overall pattern, paleontologists have attempted to account for, and in some cases overcome, various biases in the fossil record using statistical techniques and the extensive data now available in the Paleobiology Database.The PaleoDB consists of individual fossil collections (genus- and species-level faunal lists), accompanied by geographic and geological information about these collections. These data have been used to assess the impact of mass extinctions, the existence of past latitudinal diversity gradients as well as habitat and substrate affinities (Alroy et al., 2008, Peters, 2008 Alroy, 2010, Anderson et al., 2011). Evolutionary processes such as turnover events, contemporaneous trends in multiple clades (e.g. increased shell durability) and extinction selectivity have also been examined (Kiessling and Aberhan, 2007, Foote et al., 2008, Bonuso and Bottjer, 2008, Clapham and Payne, 2011, Kosnik et al., 2011).

Datasets such as the PaleoDB are themselves subject to recognized limitations. Collections can be biased, both in the material available in the fossil record itself, as well as the data that is entered into the database (Wagner et al., 2007, Peters, 2008, Hannisdal and Peters, 2011, Kosnik et al., 2011). Numerous studies have attempted to assess the extent of biases in the geologic record, including continental flooding, rock volume or outcrop area, lithification biases, and biases resulting from heterogeneous data entry (Sepkoski et al., 1981, Ronov, 1994, Hendy, 2009, Alroy, 2008, Hannisdal and Peters, 2011). Attempts to correct for sampling inhomogeneities throughout the Phanerozoic record have recovered many of the previously noted features such as a general trend towards increasing diversity throughout the Phanerozoic and the end-Permian, end-Triassic and end-Cretaceous extinctions (Alroy et al., 2008).

2. Geochemical Techniques

Geochemical information, including molecules such as lipid biomarkers or biopolymers, and the molecular structure and isotopic abundances of organic and mineral specimens, preserved in fossils and the rock record in general can be informative about paleodiversity, taphonomy and paleoecology as well as the biology, diet and disease history of organisms (Macfadden and Cerling, 1996, Grice et al., 2005, Killops and Killops, 2005, Alroy, 2010). Techniques such as mass spectrometry and vibrational spectroscopy have increasingly been applied in paleontological contexts.

Mass spectrometry has been directly applied to paleontological samples to determine chemical or isotopic composition, but can also be utilized to identify biomarkers present in an environment (Stankiewicz et al., 1997, Brocks and Banfield, 2009). Biomarkers are recalcitrant organic molecules which can provide information needed to discriminate between hypotheses regarding paleoredox state, salinity and the nature of bacterial communities at the site of deposition (Killops and Killops, 2005, Brocks and Banfield, 2009). Biomarkers have been utilized to characterize potentially unusual environmental conditions associated with mass extinction events and sites of exceptional preservation (Grice et al., 2005, Hall et al., 2011). Stable isotope analyses have been used to examine paleoecology including feeding and migratory behaviors as well as environmental conditions (Quade et al., 1992, Koch et al., 1992, Koch et al., 1995, Sealy et al., 1995, Macfadden and Cerling, 1996, Hoppe et al. 1999, Yanes et al., 2008). Vibrational spectroscopy, including both infrared and Raman spectroscopy provides information on molecular composition and structure within a sample. These techniques have been applied to determine a sample's biogenicity, to study taphonomic effects and to study the thermal maturity of samples (Marshall et al., 1999, Gupta et al., 2007, Marshall et al., 2007, 2011, Thomas et al., 2011 Olcott Marshall et al., 2012, in review).

References

Alroy, J., 2010. The shifting balance of diversity among major marine animal groups. Science 329, 1191-1194.

Alroy, J., Aberhan, M., Bottjer, D.J., Foote, M., Fursich, F.T., Harries, P.J., Hendy, A.J.W., Holland, S.M., Ivany, L.C., Kiessling, W., Kosnik, M.A., Marshall, C.R., McGowan, A.J., Miller, A.I., Olszewski, T.D., Patzkowky, M.E., Peters, S.E., Villier, L., Wagner, P.J., Bonuso, N., Borkow, P.S., Brenneis, B., Clapham, M.E., Fall, L.M., Ferguson, C.A., Hanson, V.L., Krug, A.Z., Layou, K.M., Leckey, E.H., Nurnberg, S., Powers, C.M., Sessa, J.A., Simpson, C., Tomasovych, A., Visaggi, C.C., 2008. Phanerozoic trends in global diversity of marine invertebrates. Science 321, 97-100.

Anderson, B.M., Pisani, D., Miller, A.I., Peterson, K.J., 2011. The environmental affinities of marine higher taxa and possible biases in their first appearances in the fossil record. Geology 39, 971-974.

Bonuso, N., Bottjer, D.J., 2008. A test of biogeographical, environmental and ecological effect on Middle and Late Triassic brachiopod and bivalve abundance patterns. Palaios 23, 43-54.

Briggs, D., Crowther, P. Eds. 2003. Paleobiology II. Blackwell, Malden, MA.

Brocks, J.J., Banfield, J., 2009. Unravelling ancient microbial history with community proteogenomics and lipid geochemistry. Nature 7, 601-609.

Clapham, M.E., Payne, J.L., 2011. Acidifi cation, anoxia, and extinction: A multiple logistic regression analysis of extinction selectivity during the Middle and Late Permian. Geology 39, 1059-1062.

Erwin, D., 1994. The Permo-Triassic extinction. Nature 367, 231-236.

Foote, M., Crampton, J.S., Beu, A.G., Cooper, R.A., 2008. On the bidirectional relationship between geographic range and taxonomic duration. Paleobiology 34, 421-433.

Grice, K., Cao, C., Love, G.D., Bottcher, M.E., Twitchett, R.J., Grosjean, E., Summons, R.E., Turgeon, S.C., Dunning, W., Jin, Y., 2005. Photic zone euxinia during the Permian-Triassic superanoxic event. Science 307, 706-709.

Gupta, N.S., Tetlie, O.E., Briggs, D.E.G., Pancost, R.D., 2007. The fossilization of eurypterids: A result of molecular transformation. Palaios 22, 439-447.

Hall, P.A., McKirdy, D.M., Halverson, G.P., Jago, J.B. and Gehling, J.G., 2011. Biomarker and isotopic signatures of an early Cambrian Lagerstatte in the Stansbury Basin, South Australia. *Organic Geochemistry* 42, 1324-1330.

Hannisdal, B., Peters, S.E., 2011. Phanerozoic Earth system evolution and marine biodiversity. Science 334, 1121-1124.

Hendy, A.J.W., 2009. The influence of lithification on Cenozoic marine biodiversity trends. Paleobiology 35, 51-62.

Hoppe, K.A., Koch, P.L., Carlson, R.W., Webb, S.D., 1999. Tracking mammoths and mastodons: Reconstruction of migratory behavior using strontium isotope ratios. Geology 27, 439-442.

Kiessling, W., Aberhan, M., 2007. Environmental determinants of marine benthic biodiversity dynamics through Triassic-Jurassic time. Paleobiology 33, 414-434.

Killops, S., Killops, V., 2005. An introduction to organic geochemistry, 2nd ed. Blackwell, Malden, MA.

Koch, P.L., Halliday, A.N., Walter, L.M., Stearley, R.F., Huston, T.J., Smith, G.R., 1992. Sr isotopic composition of hydroxyapatite from recent and fossil salmon: The record of lifetime migration and diagenesis. Earth and Planetary Science Letters 108, 227-287.

Koch, P.L.H., J., Moss, C., Carlson, R.W., Fogel, M.L., Behrensmeyer, A.K., 1995. Isotopic tracking of the diet and home range of African elephants. Science 267, 1340-1343.

Kosnik, M.A., Alroy, J., Behrensmeyer, A.K., Fursich, F.T., Gastaldo, R.A., Kidwell, S.M., Kowalewski, M., Plotnick, R.E., Rogers, R.R., Wagner, P.J., 2011. Changes in shell durability of common marine taxa through the Phanerozoic: evidence for biological rather than taphonomic drivers. Paleobiology 37, 303-331.

Kurtén, B., Anderson, E., 1980. Pleistocene Mammals of North America. Columbia University Press, New York.

Macfadden, B.J., Cerling, T.E., 1996. Mamalian herbivore communities, ancient feeding ecology, and carbon isotopes: A 10 Million-year sequence from the Neogene of Florida. Journal of Vertebrate Paleontology 16, 103-115.

Marshall, C.P., Emery, J.R., Olcott Marshall, A., 2011. Haematite pseudomicrofossils present in the 3.5-billion-year-old Apex Chert. Nature Geoscience 4, 240-243.

Marshall, C.P., Rose, H.R., Lee, G.S.H., Mar, G.L., Wilson, M.A., 1999. Structure of organic matter in conodonts with different colour alteration indexes. Organic Geochemistry 20, 1339-1352.

Olcott Marshall, A., Wehrbein, R., Gonzalez, L., Lieberman, B., Lin, J., Marshall, C.P., *in review*. A molecular view of the Burgess Shale-type preservation mechanism.

Olcott Marshall, A., Wehrbein, R.L., Lieberman, B.S., Marshall, C.P., 2012. Raman spectroscopic investigations of Burgess Shale-type preservation: A new way forward. Palaios 27, 288-292.

PaleoDB. Available at: www.pbdb.org.

Peters, S.E., 2008. Environmental determinants of extinction selectivity in the fossil record. Nature 454, 626-629.

Peters, S.E., Gaines, R.R., 2012. Formation of the "Great Unconformity" as a trigger for the Cambrian explosion. Nature 484, 363-366.

Quade, J., Cerling, J.C., Barry, J.C., Morgan, M.E., Pillbeam, D.R., Chivas, A.R., Lee-Thorp, J.A., van der Merwe, N.J., 1992. A 16 million year record of paleodiet using carbon and oxygen isotopes in fossil teeth from Pakistan. Chemical Geology 94, 183-192.

Ronov, A.B., 1994. Phanerozoic transgressions and regressions on the continents: a quantitative approach based on areas flooded by the sea and areas of marine and continental deposition. American Journal of Science 294, 777-801.

Sealy, J., Armstrong, R., Schrire, C., 1995. Beyond lifetime averages: Tracing life histories through isotopic analysis of different calcified tissues from archaeological human skeletons. Antiquity 69, 290-300.

Sepkoski, J.J., 1981. A factor analytic description of the Phanerozoic marine fossil record. Paleobiology 7, 36-53.

Sepkoski, J.J., Bambach, R.K., Raup, D.M., Valentine, J.W., 1981. Marine diversity and the fossil record. Nature 293, 435-437.

Stankiewicz, B., Briggs, D., Evershed, R., 1997. Chemical composition of Paleozoic and Mesozoic fossil invertebrate cuticles as revealed by pyrolysis-gas chromatography/mass spectrometry. Energy and Fuels 11, 515-521.

Thomas, D.B., Fordyce, R.E., Frew, R.D., Gordon, K.C., 2007. A rapid, non-destructive method of detecting diagenetic alteration in fossil bone using Raman spectroscopy. Journal of Raman Spectroscopy 38, 1533-1537.

Thomas, D.B., McGoverin, C.M., Fordyce, E.R., RFrew, R.D., Gordon, K.C., 2011. Raman spectroscopy of fossil bioapatite - A proxy for diagenetic alteration of the oxygen isotope composition. Palaeogeography, Palaeoclimatology, Palaeoecology 310, 62-70.

Wagner, P.J., Aberhan, M., Hendy, A., Kiessling, W., 2007. The effects of taxonomic standardization on sampling-standardized estimates of historical diversity. Proceedings of the Royal Society, B 274, 439-444.

Yanes, Y., Delgado, A., Castillo, C., Alonso, M.R., Ibáñez, M., De la Nuez, J., Kowalewski, M., 2008. Stable isotope (δ18O, δ13C, and δD) signatures of recent terrestrial communities from a low-latitude, oceanic setting: Endemic land snails, plants, rain, and carbonate sediments from the eastern Canary Islands. Chemical Geology 249, 377-392.

Chapter 2

Global geologic, biologic and geochemical influences on the formation of Phanerozoic marine *Konservat-Lagerstätten*

1. Introduction

1.1 Significance of *Konservat-Lagerstätten*

Konservat-Lagerstätten are fossil deposits with exceptional preservation of less recalcitrant tissues (Seilacher, 1970). These exceptional localities offer key insights into paleoecology, paleodiversity and the biological affinities of fossil taxa (Allison, 1988b, Allison and Briggs, 1993, Butterfield, 2003, Nudds and Selden, 2008, Schiffbauer and Laflamme, 2012). Under normal circumstances only biomineralized or otherwise recalcitrant tissues such as sporopollenin and lignin are preserved in the fossil record, thus excluding organisms which do not produce such tissues from our understanding of fossil ecosystems (Briggs, 1991). This impact may be significant: one study of intertidal marine organisms found that 30% of genera lacked hard parts and would therefore be excluded from most of the fossil record (Schopf, 1978). Examining the Burgess Shale *lagerstätte,* Briggs (1991) notes that only 20% of genera are found in contemporaneous deposits that do not preserve soft tissues. Determining the factors which contribute to exceptional preservation is of paramount importance for the direction and growth of taphonomic and paleontological studies (Schiffbauer and Laflamme, 2012). This chapter examines possible geologic, biologic and geochemical controls on the formation of these deposits throughout the Phanerozoic.

Exceptionally preserved fossils from *Konservat-Lagerstätten* have also been significant for determining the biological affinity of taxa including conodonts and graptolites and continue to provide important information about the evolution of diverse groups of organisms (Sutton et al.,

2005, Siveter, 2008). *Konservat-Lagerstätten* have documented important evolutionary events, not only during the Cambrian radiation but through several important intervals in geologic history (Siveter, 2008, Schiffbauer and Laflamme, 2012). Stem group arthropods preserved in Cambrian *Konservat-Lagerstätten* such as the Burgess Shale and Chengjiang have been particularly important to debates about arthropod phylogeny and the evolution of the arthropod bodyplan (Edgecombe, 2010).

Allison and Briggs (1993) studied 44 *Konservat-Lagerstätten* and found these deposits to be unevenly distributed through time and that this distribution did not correlate with facies availability, outcrop area, paleolatitude or oceanic phosphate concentrations. Schiffbauer and Laflamme (2012) expanded this dataset and again find an uneven distribution through time, although potential geologic controls were not explored. The majority of studies which consider multiple marine *Konservat-Lagerstätten* focus on Burgess Shale-type preservation and consider numerous potential causes for preservation (e.g. Butterfield, 1990, Petrovitch, 2001, Gaines et al., 2008, Gaines and Droser, 2010, Van Roy et al., 2010, Gaines et al., 2012, Olcott Marshall et al., 2013, in review).

2. Exceptional Fossil Preservation

2.1 Preservation pathways

Preservation of less recalcitrant tissues can occur through many different pathways but relies on some form of stabilization, typically through mineralization occurring more rapidly than decay of these tissues. Multiple forms of mineralization may be present in the same deposits [e.g. different modes of mineralization associated with different tissue types or taxa (Butterfield et al., 2007, Powell, 2009, Briggs, 2003)], and even in different parts of the same organ [e.g. a pair of *Anomalocaris* eyes preserved as calcium phosphate and iron oxide, after pyrite (Paterson et al.,

2011)], which may indicate that a mechanism for slowing decay, permitting mineralization, may be the primary control on the formation of *Konservat-Lagerstätten*.

2.2 Decay Inhibition

Limiting decay is essential for exceptional fossil preservation. Factors which may slow decay include anoxia and limited bioturbation, which are generally viewed as necessary but not sufficient for exceptional fossil preservation (Allison and Briggs, 1993, Gaines et al., 2004, Gaines and Droser, 2010, Lin et al., 2010, Van Roy et al., 2010, Schiffbauer and Laflamme, 2012). Allison and Briggs (1991a, 1991b, 1993) also note that scavenging and bioturbation may themselves be limited under anoxic conditions. Of course anoxia alone is insufficient for exceptional preservation (Butterfield, 1990, Briggs, 2003), and experiments on modern organisms show that the carcasses of shrimp will be virtually destroyed in 25 weeks, even in systems which are allowed to rapidly become anoxic (Allison, 1988a), although this may provide enough time to allow decay-induced mineralization under special conditions. Microbial degradation in anoxic environments proceeds most rapidly through bacterial sulfate reduction (BSR). High sulfate levels may result in degradation rates as rapid as those of aerobic decay (Allison, 1988a, Allison, 1988b Canfield, 1994, Gaines et al., 2012), although environments with a low sulfate concentration have lower rates of BSR (Gill et al., 2007).

2.3 Stabilization

Stabilization, the process of replicating the form of labile tissues in a geologically stable manner, typically through mineralization (Allison, 1988b, Briggs, 2003), is essential for the preservation of a record of labile tissues through geologic time (Cai et al., 2012, Schiffbauer and Laflamme, 2012). If decay is slowed or inhibited but organic material remains in its original form, as occurs when a carcass is frozen or desiccated, or due to temporary geochemical

fluctuations such as hypersalinity, decay may resume at a normal pace if environmental conditions change. As such changes are essentially guaranteed over geologic timescales, the conversion of the organic material to a geologically stable form or the replication of labile tissues in minerals, either through authigenic mineralization or the stabilization of a mold, is the proximal cause of *Konservat-Lagerstätten* formation. The vast majority of Phanerozoic exceptionally preserved deposits are represented by four styles of preservation: Burgess Shale-type (BST) preservation, phosphatization, pyritization and preservation as an organic residue, outline or as other organic material. Imprints of soft tissues or exceptionally detailed molds and casts are also important in a number of localities throughout the Phanerozoic, as are calcification and dolomitization of labile tissues (Brett et al., 2012, Young et al., 2007, Etter, 2002).

2.4 Styles of Preservation

2.4.1 Burgess Shale-type preservation

Burgess Shale-type preservation is here defined as marine preservation where the initial mode of preservation was a two-dimensional carbonaceous compression preserving non-mineralized organic external structures but not internal tissues (Butterfield, 2003, Olcott Marshall et al., in review). It may be associated with some pyritized or phosphatized tissues, and occasionally both a present within the same part of an organism (Paterson et al., 2011). Mechanisms proposed for this type of preservation include clay templating or aluminosilicification (Orr et al., 1998, Gabbott et al., 2001, Butterfield et al., 2007, Anderson et al., 2011, Cai et al., 2012), iron templating (Petrovich, 2001) and sulfurization (Olcott Marshall et al., in review). Organic walled fossils from the Doushantuo Formation, which has undergone minimal metamorphism, are closely associated with aluminosilicate clays indicating that clay minerals may have been authigenic (Bristow et al., 2009, Anderson et al., 2011). Furthermore,

organic compressions are enveloped by aluminosilicates indicating they may be essential to preservation (Anderson et al., 2011). Butterfield (1990, 1995, Butterfield et al., 2007) argues that microbial autolytic and digestive enzymes may be suppressed by clay minerals. Clay minerals have been shown to stabilize structural polymers and to have high affinity for organic matter (Orr et al., 1998), but others feel it would be evolutionarily unlikely for bacteria to utilize extracellular enzymes that would be useless in the presence of clays (Petrovich, 2001). Additionally, this original clay model has been challenged because, with the exception of one study showing kaolinite and quartz can become adsorbed onto bacteria-associated lobster eggs, clay has not been shown to template organic materials under normal marine conditions (Martin et al., 2004, Butterfield et al., 2007). Furthermore, utilizing graptolites as an analogue for BST preservation, Page et al. (2008) showed that clay templates formed too late to account for decay retardation.

The iron templating model proposes that Fe^{2+} ions generated by Fe^{3+} reducing bacteria adsorbed onto biopolymers such as chitin can provide templates for the nucleation of iron rich minerals (Petrovich, 2001). This iron template could both partially protect the biopolymer allowing it to become a stable kerogen and aid in the formation of iron rich clay minerals (Petrovich, 2001). This theory nevertheless is not without its own concerns; when iron was added in a taphonomic study of shrimps decaying there was no effect on decay (Sagemann et al., 1999 cited in Briggs, 2003).

Gaines et al. (2008) and Olcott Marshall et al. (2013, in review) argue that conservation of organic C is primary based on enrichment of C in scanning electron microscope-energy dispersive X-ray spectroscopic elemental mapping (SEM-EDX) from 11 BST deposits and Raman spectra obtained from the Spence shale, Kaili biota, Chengjiang Biota and Pioche Shale

consistent with the preservation of original carbonaceous material. Cai et al., (2012) propose that both kerogenization and aluminosilicification may have important roles in BST preservation in different deposits but consider aluminosilicification to be a thin coating helping to stabilize carbonaceous material. Sulfurization, the cross-linking of organic molecules, usually polysaccharides, with sulfur, results in the formation of geologically stable macromolecules resistant to degradation (Kok, 2000). In modern anoxic sulphidic environments molecules can become sulphurized very quickly, sometimes even at the sediment-water interface (Wakeham, 1995).

2.4.2 Phosphatization

Phosphatization involves the replication of tissues, typically muscle or gut in calcium phosphate. In one experiment muscle tissue from arthropods, which has relatively high levels of phosphate, was successfully replicated in calcium phosphate under anoxic conditions, without the introduction of any additional phosphate (Briggs and Kear, 1993). Briggs and Kear (1993) proposed rapid overgrowth by microbial mats as one mechanism for isolating a carcass and maintaining the closed conditions required for a decay related drop in pH to induce this kind of mineralization. Allison and Briggs (1993) noted that the increase in largely phosphatized *Konservat-Lagerstätten* during the Jurassic does correspond roughly to a peak in global phosphate deposits but that increases in phosphate deposition during the Ordovician and Permian did not appear to increase the number of phosphatized *Konservat-Lagerstätten*. This may suggest that the decaying organism is the source of phosphate rather than the surrounding marine water, indicating the lack of a global geochemical control.

2.4.3 Pyritization

Pyritization consists of the partial replacement or encrusting of labile tissues in pyrite, usually related to limited bacterial sulfate reduction (Skinner, 2005). Pyritization may proceed extremely rapidly; experimental pyritization of plant material has shown it to occur in as little as 12 weeks, and when sediments are enriched in iron, pyritization can even replicate cellular structures (Grimes et al., 2001). The morphology of iron oxide pseudomorphs, used as a proxy for original pyrite crystal forms, has led some to believe that pyrite mineralization is likely related to decay by sulfate reducing bacteria (Gabbott et al., 2004, Van Roy et al., 2010). Putative autolithified bacteria have even been found in association with pyritic microenvironments in the Kinzers Formation (Skinner, 2005).

2.4.4 Other preservation of organic material

The marine Holzmaden fossil *lagerstätte* and numerous non-marine deposits preserve organic material as dark stains outlining skeletal material (Appendices 1 and 2), providing information on the anatomy of an organism (Frimmel et al., 2004, Selden and Nudds, 2004). At least some of these stains appear to be composed of bacterial films rather than the original soft parts of the organism (Cunningham, 1991, Rothschild and Martin, 2003).The Eocene Monte Bolca *lagerstätte* also appears to preserve organic matter, although the preservational mechanism is unclear (Allison and Briggs, 1991b).

2.4.5 Exceptionally detailed molds, casts and impressions

Exceptionally detailed impressions or molds which provide detailed information on non-mineralized tissues and organisms include three marine *Konservat-Lagerstätten* from the Cambrian (the Parker Slate, the Poleta Fm and the Wood Canyon Fm [Shaw, 1955, 1962, Hagadorn and Waggoner, 2000]), the Jurassic Solnhofen *lagerstätte* (Selden and Nudds, 2004) and the Eocene Fur Formation. (Bertelli et al., 2011, Petrulevičius et al., 2008).

3. Methods

In this study we expand the dataset of Phanerozoic *Konservat-Lagerstätten* to 77 marine localities (table 1) up from 32 in Allison and Briggs (1993) and 44 in Schiffbauer and Laflamme (2012).The database was assembled by examining the English language literature for published reports of exceptional fossil preservation. Here, *Konservat-Lagerstätten* were defined as localities where non-biomineralized tissues, excluding such recalcitrant tissues as graptolite periderm, sporopollenin and lignin, are preserved or replicated through means stable on geologic timescales, thus excluding bog deposits and frozen carcasses, consistent with the methodologies of Allison and Briggs (1993) and Schiffbauer and Laflamme (2012). For the purposes of this study, only marine and marginal marine localities were studied. Deposits in swamps, estuaries or other environments of less than normal salinity were characterized as such and separated from marine environments (Appendix 1). Exceptional faunas in lacustrine environments were excluded both due to the tendency for lacustrine environments to be removed from the rock record over time (Allison and Briggs, 1993) and due to their isolated nature. Individual lakes may exhibit widely varying chemistries peculiar to their particular geologic setting and are therefore not likely to be related to global processes. An important treatment of these deposits with regard to insects can be found in Smith (2012) and a representative list of such deposits can be found in Appendix 2. The majority of exceptional Ediacaran deposits are molds which are most likely related to microbial mats (Narbonne, 1998, Gehling 1999, Gehling et al., 2005, Narbonne, 2005, Darroch et al., 2012). The extensive microbial mat communities required for this type of preservation become rare in the Phanerozoic due to increased grazing and bioturbation, and therefore these deposits are not considered in this analysis (Narbonne, 1998, 2005). A representative list of such deposits can be found in Appendix 3.

Where single biotas may span large geographic areas but discrete and widely separated localities have been identified these deposits are regarded as distinct *Konservat-lagerstätten*. The presence of geographically widespread areas where exceptional preservation takes place is itself indicative of the extent of the phenomenon during a particular interval. Similarly, when the method of preservation changes significantly in different deposits within a geographically restricted area, each method of preservation is regarded as a distinct deposit. When the preservational method is the same but there is a formation level gap between periods of exceptional preservation these are also regarded as distinct deposits. No minimum number of recovered exceptionally preserved fossils was used, under the presumption that individual fossils recovered from less well studied sites may represent more extensive preservation of non-biomineralized tissues.

4. Database Trends

4.1 Secular Distribution

Consistent with Allison and Briggs (1993) and Schiffbauer and Laflamme (2012) we find an uneven distribution of *Konservat-Lagerstätten* through time (Figure 1). *Konservat-Lagerstätten* are most prevalent in the Cambrian, but are also relatively high in number during the Ordovician and Jurassic. The high incidence of Ordovician *Konservat-Lagerstätten* represents a departure from Allison and Briggs (1993), as their database only contained one Ordovician deposit, although this increase was detected in Schiffbauer and Laflamme (2012). The fewest *Konservat-Lagerstätten* occur in the Permian and Neogene. The large number of exceptionally preserved deposits from deltaic or swamp environments in the Carboniferous is also noteworthy (10 total deposits compared to 5, Appendix 1).

4.2 Geographic Distribution of *Konservat-Lagerstätten*

In order to assess potential geographic biases, the locations of the *Konservat-Lagerstätten* studied were plotted on paleogeographic maps for each period (Figures 2 and 3) (Blakey, 2003, Available at http://cpgeosystems.com/paleomaps.html). During the Paleozoic, *Konservat-Lagerstätten* are globally distributed (Figure 2). Cambrian deposits are located surrounding Laurentia, in Australia, South China and Baltica (Figure 2A). Ordovician deposits are located surrounding Laurentia, in Morocco, South Africa and Avalonia (Figure 2B). Silurian deposits occur in Laurentia, Baltica and Avalonia (Figure 2C). Devonian deposits occur in Australia, Laurentia and Baltica (Figure 2D).The Carboniferous and Permian are not shown as the dataset includes only two Carboniferous marine deposits, both from the United Kingdom, and only one Permian marine *Konservat- lagerstätte* (Buck Mountain in the United States).

During the Triassic and Cretaceous deposits still appear to be globally distributed but the Jurassic shows a significant geographic bias with seven out of eight deposits found in the European Epicontinental Sea (Figure 3). This distribution may mean that the disproportionately large number of Jurassic *Konservat-lagerstätten* are the result of conditions restricted to this epicontinental sea, rather than a global phenomenon. Only two Paleogene marine localities, both from the Eocene (the Fur Formation in Denmark and the Monte Bolca in Italy), and only one Neogene example, the Chita locality in Japan, were recorded in this dataset (Table 1).

4.3 Trends in Mineralization

Burgess Shale-type deposits dominate Cambrian *Konservat-lagerstätten*, representing 28 of the 34 Cambrian deposits (Table 1), decreases dramatically by the Ordovician and disappears from the marine fossil record after the Silurian (Figure 4). BST deposits make up roughly half of all Phanerozoic marine deposits considered in this study (35/77). Phosphatization is a common secondary mechanism for gut tissue in BST deposits during the Cambrian, but incidence of

phosphatization remains relatively constant throughout the Phanerozoic until the Tertiary. Phosphatizationt is, however, (as noted by Allison and Briggs, 1993) the primary mode of preservation for *Konservat-Lagerstätten* during the Jurassic (Figure 4). One Cambrian, one Ordovician, two Silurian, two Devonian, one Permian, one Triassic, five Jurassic and three Cretaceous marine Konservat-*Lagerstätten* have phosphatization as the primary preservational mechanism for labile tissues. Pyritization seems particularly important in the Ordovician (e.g. Van Roy et al., 2010, Botting et al., 2011) and two Cambrian, four Ordovician, three Devonian, one Carboniferous and one Jurassic deposit have pyritization as the primary preservational mechanism for labile tissues (Figure 4).

5. Influence of Geology

5.1 Time

The null hypothesis describing the distribution of exceptionally preserved deposits is that they are distributed randomly through geologic time. One of the first order controls on the distribution of any type of deposit among the periods of the Phanerozoic is the disparate lengths of these periods (ranging from ~20-80 million years). The rate of formation of these deposits, determined as the total number of deposits formed during a period divided by the duration (in million year increments) of the period is therefore used in all subsequent comparisons (Figure 5). Once this metric is applied, the Cambrian contains the highest rate of formation of these deposits. Additionally, the Ordovician and Silurian are also periods when significant numbers of exceptionally preserved deposits form, something not recovered in Allison and Briggs (1993), although Schiffbauer and Laflamme (2012) do note a significant number of Ordovician deposits. Rates of formation are much lower in the Devonian, decrease through the Carboniferous and reach a low in the Permian. In contrast to Schiffbauer and Laflamme (2012), which recorded

absolute numbers of deposits rather than rates of formation, the Silurian appears to be a more significant period for *Konservat-lagerstätten* formation and the Devonian and Cretaceous appear to be less significant periods of *Konservat-lagerstätten* formation. Although the Jurassic is the high point for Mesozoic and Cenozoic deposits, the rate of formation during this period does not reach the rate during the Cambrian, Ordovician and Silurian (Figure 5).

5.2 Fossiliferous Strata

Another possibility for explaining the uneven distribution of *Konservat-Lagerstätten* through time is that some fraction of fossiliferous strata will contain exceptionally preserved fossils. When the rate of formation for exceptional deposits is compared to the fraction of units deposited per Ma from each time period which are fossiliferous (Peters, 2007) it is clear that *Konservat-Lagerstätten* are not typical fossiliferous deposits (Figure 6). In particular the increase in fossiliferous deposits from the Cretaceous through the Tertiary corresponds to a decrease in the rate of formation for exceptional deposits.

Estimates of North American and European marine sedimentary outcrop area (Allison and Briggs, 1993) also shows little concordance with *Konservat-Lagerstätten* formation (Figure 7A), in agreement with the findings of Allison and Briggs (1993). Similarly, continental flooding is thought to correspond to times of sediment deposition within epicontinental seas, environments not only with greater potential for preservation than marginal marine environments, but also with increased chances for local anoxia or salinity changes due to sluggish circulation (Peters, 2007). However, estimates continental flooding through time (Ronov, 1994) do not show strong correspondence with the formation of *Konservat-Lagerstätten* (Figure 7B). Continental flooding is highest during the Ordovician and generally falls throughout geologic time with another peak during the Cretaceous (Ronov, 1994). *Konservat-Lagerstätten,* in contrast, show low rates of

formation during the Carboniferous and Permian and the highest rate of formation during the Mesozoic occurs in the Jurassic rather than the Cretaceous.

6. Influence of Biology

Bioturbation by infaunal organisms inhibits preservation both by direct disruption or consumption of carcasses and by delivering oxidants to the sediment (Butterfield, 1995, Gaines et al., 2004, Lyons and Gill, 2009, Gaines and Droser, 2010, Lin et al., 2010, Van Roy et al., 2010). Burrowing organisms both physically mix sediments and pump sea water through the subsurface (bioirrigation) which can aid in microbial decay (Lyons and Gill, 2009, Canfield and Farquhar, 2009). Canfield and Farquhar (2009) also link the increase in marine sulfate concentrations during the Phanerozoic to increased bioturbation. The increase in diversity of modern faunal organisms has been associated with increased burrowing (Bambach, 1993) and increased bioturbation has been proposed as a potential reason for the decline in *Konservat-Lagerstätten* formation after the Cambrian (e.g. Butterfield, 1995, Van Roy et al., 2010). The Paleozoic fauna included an increased number of infaunal classes relative to the Cambrian; however, the Modern fauna shows a dramatic increase in infaunal guilds and infaunal tiering (distribution of benthic organisms above and below the seafloor) (Bambach, 1983, Bottjer et al., 1996). Comparing diversity to marine *Konservat-Lagerstätten* formation shows no strong link between increased diversity of Sepkoski's modern fauna and decline in *Konservat-Lagerstätten* formation throughout the Phaerozoic, although the possibility that increasing bioturbation is influencing the decline in *Konservat-Lagerstätten* after the Cambrian may find some support (Figure 8).

Examining the trace fossil record also indicates that increased utilization of infaunal ecospace may be responsible for the dramatic reduction in post-Cambrian *Konservat-Lagerstätten*

formation. Bioturbation throughout the Cambrian of the Great Basin of the United States was largely limited to depths of less than 6 cm in carbonate environments, with dramatic increases in depth and extent of bioturbation in the Ordovician (Droser and Bottjer, 1988). Ichnofabric, the total sedimentary fabric resulting from bioturbation (Ekdale and Bromley, 1983, Droser and Bottjer, 1993), also shows a significant increase between the middle and upper Ordovician which has been interpreted as indicating increased infaunal activity during the early Paleozoic, at least with respect to inner shelf environments (Figure 9A) (Droser and Bottjer, 1989, Droser and Bottjer, 1993, Bottjer et al., 1996). The sections studied by Droser and Bottjer (1989) were deposited under similar physical conditions and increased average ichnofabric index value (indicating increased homogenization via bioturbation) was also accompanied by increasing size of trace fossils and changes in trace fossil types identified supporting this conclusion (Figure 9B) (Droser and Bottjer, 1989, Droser and Bottjer, 1993). Globally, the diversity of trace fossils increases gradually from the Cambrian through Silurian, with a major increase during the Cretaceous related to increased trace fossil diversity from the deep ocean environments (Figure 9C) (Sepkoski, 1981).

7. Geochemical Influences

7.1 Oxygen

Anoxia has long been considered a necessary but insufficient condition for most cases of exceptional preservation (Allison, 1988a, Allison, 1988b, Butterfield, 1990, Allison and Briggs, 1993, Briggs, 2003) although some localities may have been deposited under dysoxic conditions or beneath an oxygenated water column (Powell et al., 2003, Powell, 2009, McKirdy et al., 2011, Garson et al., 2012). Local marine anoxia may be related to either global oxygen levels (derived from the GeoCarbSulf model of Berner, 2009) or the distribution of recognized oceanic anoxic

events (OAEs) (Figure 10). Global atmospheric oxygen levels could have influenced the formation of hypoxic or dysoxic conditions (Berner et al., 2003) but do not appear to correlate with the rate of formation of exceptionally preserved fossil localities, excepting the high in the Permian corresponding to the lowest rate of *Konservat-lagerstätten* formation in the Phanerozoic and perhaps the higher incidence in the Jurassic corresponding to the lowest oxygen levels modeled for the Phanerozoic. OAE are concentrated in the Jurassic and Cretaceous and deposition during the Toarcian OAE, also known as the *Posidonienschiefer* OAE, after the *Posidonienschiefer Lagerstätte*, does correspond with exceptional fossil preservation. However the frequency of OAEs in the Cretaceous is significantly greater in the Cretaceous than the Jurassic and Paleozoic OAEs do not appear to correlate with formation of *Konservat-Lagerstätten* (Figure 10*).*

7.2 Sulfate

After oxygen, sulfate is the principle terminal electron acceptor for microbial decay in the marine realm, and BSR can occur as rapidly as aerobic decay (Allison, 1988a, Canfield, 1994, Gaines et al., 2012). When both oxygen and sulfate are limited decay is significantly slowed, increasing the window for fossilization (Hammarlund et al., 2011, Gaines et al., 2012). Low ocean sulfate concentrations have been proposed as essential for Burgess Shale-type (BST) preservation, either coupled with carbonate permeability barriers or incomplete oxygenation of the deep ocean (Gaines et al., 2012, Olcott Marshall et al., in review), but global marine sulfate concentration may influence the incidence of other types of exceptional fossil preservation as well. Low global marine sulfate concentrations may increase the chances for the development of sulfate-poor localities or sediments, shifting microbial decay to less efficient metabolic pathways such as methanogenesis and fermentation (Canfield, 1994, Pallud and Van Cappellen, 2006,

Gaines et al., 2012). This would therefore expand the window during which the labile tissues of a carcass remain intact and available for a variety of stabilizing mechanisms to record their morphology.

There is in fact a noticeable inverse correlation between marine sulfate concentrations and the formation of marine *Konservat-Lagerstätten* (Figure 11). Data are derived from mean values from halite fluid inclusions (Lownstein et al., 2003, some datapoints previously reported in Horita et al., 2002) and supplemented with values calculated for the Cambrian SPICE event, the early Ordovician and the Toarcian from isotopic data (Gill et al., 2007, Gill et al., 2011, Newton et al., 2011, Thompson and Kah, 2012, ranges shown in Appendix IV). Note also the high marine sulfate concentration during the Ediacaran which is recorded from fluid inclusions in Oman. High sulfate concentrations during the Ediacaran may have been important in limiting Burgess Shale-type preservation in this period (Olcott Marshall et al., in review). Sulfate concentrations were high during the Mid Paleozoic and Tertiary when exceptional fossil preservation was relatively rare and lower during the Cambrian, Ordovician and Jurassic when relatively large numbers of *Konservat-Lagerstätten* formed. Decreased rates of BSR due to low sulfate concentrations may have had a significant role in slowing decay and therefore providing opportunities for stabilization through mineralization or sulfurization. It is important to note however that similar sulfate concentrations in the Silurian and Cretaceous did not result in similar rates of *Konservat-lagerstätten* formation. This disparity may be related to the influence of biological controls, especially the influence of increased bioturbation (Bambach, 1993, Butterfield, 1995, Van Roy et al., 2010).

8. Conclusions

Phanerozoic marine *Konservat-Lagerstätten* continue to be an important source of paleobiologic information and represent an active area of research across the globe. As new localities and new geochemical information are published, additional insights into the conditions necessary for these deposits to form. Increased bioturbation may have influenced the steep decline in the rate of *Konservat-Lagerstätten* formation after the Cambrian. In contrast, global oxygen levels and oceanic anoxic events do not appear to have significantly influenced *Konservat-Lagerstätten* formation. The inverse correlation between low marine sulfate concentrations and *Konservat-Lagerstätten* formation could indicate that sulfate limitation is important for the majority of deposits where non-biomineralized tissues are preserved. Information on sulfate levels from event beds at 6 BST deposits compared with background intervals has demonstrated the importance of sulfate limitation in these deposits (Gaines et al., 2012). Additional data regarding sulfate levels from other types of *Konservat-Lagerstätten* are needed to further test this correlation.

References

Allison, P.A., 1988a. The Role of Anoxia in the Decay and Mineralization of Proteinaceous Macro-Fossils. Paleobiology 14, 139-154.

Allison, P.A., 1988b. Konservat-Lagerstatten - Cause and Classification. Paleobiology 14, 331-344.

Allison, P.A., Briggs, D.E.G., 1991a. The taphonomy of soft-bodied animals, in: Donovan, S.K. (Ed.), The processes of fossilization. Columbia University Press, New York, pp. 120-140.

Allison, P.A., Briggs, D.E.G., 1991b. Taphonomy of non-mineralized tissues, in: Allison, P.A., Briggs, D.E.G. (Eds.), Taphonomy: Releasing the data locked in the fossil record. Plenum Press, New York, pp. 26-70.

Allison, P.A., Briggs, D.E.G., 1993. Exceptional fossil record: Distribution of soft-tissue preservation through the Phanerozoic. Geology 21, 527-530.

Anderson, E.P., Schiffbauer, J.D., Xiao, S., 2011. Taphonomic study of Ediacaran organic-walled fossils confirms the importance of clay minerals and pyrite in Burgess Shale–type preservation. Geology 39, 643-646.

Bambach, R.K., 1983. Ecospace utilization and guilds in marine communities through the Phanerozoic, in: Tevesz, M.J.S., McCall, P.L. (Eds.), Biotic Interactions in Recent and Fossil Benthic Communities. Plenum, New York, pp. 719-746.

Bambach, R.K., 1993. Seafood through time: Changes in biomass, energetics and productivity in the marine ecosystem. Paleobiology 19, 372-397.

Berner, R.A., 2009. Phanerozoic Atmospheric Oxygen: New Results Using the Geocarbsulf Model. American Journal of Science 309, 603-606.

Berner, R.A., Beerling, D.J., Dudley, R., Robinson, J.M., Wildman, R.A., 2003. Phanerozoic atmospheric oxygen. Annual Review of Earth and Planetary Sciences 31, 105-134.

Bertelli, S., Chiappe, L.M., Mayr, G., 2011. A new Messel rail from the Early Eocene Fur Formation of Denmark (Aves, Messelornithidae). Journal of Systematic Palaeontology 9, 1477-2019.

Blakey, R. C., Carboniferous-Permian paleogeography of the assembly of Pangaea., *in* Proceedings XVth International Congress on Carboniferous and Permian Stratigraphy, Utrecht, the Netherlands, 2003, Royal Netherlands Academy of Arts and Sciences.

Blakey, R.C. Available at http://cpgeosystems.com/paleomaps.html

Bond, D., Wignall, P.B., Racki, G., 2004. Extent and duration of marine anoxia during the Frasnian, Famennian (Late Devonian) mass extinction in Poland, Germany, Austria and France. Geological Magazine 141, 173-193.

Botting, J.P., Muir, L.A., 2008. Unravelling causal components of the Ordovician Radiation: the Builth Inlier (central Wales) as a case study. Lethaia 41, 111-125.

Botting, J., Muir, L.A., Sutton, M.D., Barnie, T., 2011. Welsh gold: A new exceptionally preserved pyritized Ordovician biota. Geology 39, 879-882.

Bottjer, D.J., Schubert, J.K., Droser, M.L., 1996. Comparative evolutionary palaeoecology: assessing the changing ecology of the past. Geological Society, London, Special Publications 102, 1-13.

Brett, C.E., Zambito IV, J.J., Hunda, B.R., Schindler, E., 2012. Mid-Paleozoic Trilobite Lagerstatten: Models of diagenetically enhanced obrution deposits. Palaios 27, 326-345.

Briggs, D.E.G., 1991. Extraordinary fossils. American Scientist 79, 130-141.

Briggs, D.E.G., 2003. The role of decay and mineralization in the preservation of soft-bodied fossils. Annual Review of Earth and Planetary Sciences 31, 275-301.

Briggs, D.E.G., Kear, A.J. 1993. Fossilization of Soft Tissue in the Laboratory. Science 259, 1439-1442.

Briggs, D.E.G., Moore, R.A., Shultz, J.W., Schweigert, G., 2005. Mineralization of soft-part anatomy and invading microbes in the horseshoe crab *Mesolimulus* from the Upper Jurassic Lagerstatte of Nusplingen Germany. *Proceedings of the Royal Society* 272, 627-632.

Bristow, T.F., Kennedy, M.J., Derkowski, A., Droser, M.L., Jiang, G., Creaser, R.A., 2009. Mineralogical constraints on the paleoenvironments of the Ediacaran Doushantuo Formation. PNAS 106, 13190-13195.

Butterfield, N.J., 1990. Organic Preservation of Non-Mineralizing Organisms and the Taphonomy of the Burgess Shale. Paleobiology 16, 272-286.

Butterfield, N.J., 1995. Secular distribution of Burgess-Shale-type preservation. Lethaia 28, 1-13.

Butterfield, N.J., 2002. *Leanchoilia* guts and the interpretation of three-dimensional structures in Burgess Shale-type fossils. Paleobiology 28, 155-171.

Butterfield, N.J., 2003. Exceptional fossil preservation and the Cambrian explosion. Integrative and Comparative Biology 43, 166-177.

Butterfield, N.J., Balthasar, U., Wilson, L.A., 2007. Fossil Diagenesis in the Burgess Shale. Palaeontology 50, 537-543.

Cai, Y., Schiffbauer, J.D., Hua, H., Xiao, S., 2012. Preservational modes in the Ediacaran Gaojiashan Lagerstätte: Pyritization, aluminosilicification and carbonaceous compression. Palaeogeography, Palaeoclimatology, Palaeoecology 326-328.

Canfield, D.E., 1994. Factors influencing organic carbon preservation in marine sediments. Chemical Geology 114, 315-329.

Canfield, D.E., Farquhar, J., 2009. Animal evolution, bioturbation and the sulfate concentration of the oceans. PNAS 106, 8123-8127.

Crimes, T.P., Droser, M.L., 1992. Trace fossils and bioturbation: The other fossil record. Annual Review of Ecology and Systematics 23, 339-360.

Cunningham, C.R., 1991. Bacteria and algae as agents of exceptional preservation within the Hamilton fossil lagerstatte (Virgilian), Kansas. Geological society of America Abstracts with Programs, 345.

Darroch, S.A.F., LaFlamme, M., Schiffbauer, J.D., Briggs, D.E.G., 2012. Experimental formation of a microbial death mask. Palaios 27, 293-303.

Droser, M.L., Bottjer, D.J., 1988. Trends in depth and extent of bioturbation in Cambrian carbonate marine environments, western United States. Geology 16, 233-236.

Droser, M.L., and Bottjer, D.J., 1989. Ichnofabric of sandstones deposited in high-energy nearshore environments; measurement and utilization. Palaios 4, 598-604.

Droser, M.L., Bottjer, D.J., 1993. Trends and patterns of Phanerozoic ichnofabrics. Annual Review of Earth and Planetary Sciences 21, 205-225.

Dzik, J., Lendzion, K., 1988. The oldest arthropods of the East European Platform. Lethaia 21, 29-38.

Ekdale, A.A., Bromley, R.G., 1983. Trace fossils and ichnofabric in the Kjolby Gaard Marl, Upper Cretaceous, Denmark. Bulletin of the Geological Society of Denmark 31, 107-119.

Edgecombe, G.D., 2010. Arthropod phylogeny: An overview from the perspectives of morphology, molecular data and the fossil record. Arthropod Structure & Development 39, 74-87.

Etter, W., 2002. Monte San Giorgio: remarkable Triassic marine vertebrates, in: Bottjer, D.J., Etter, W., Hagadorn, J.W., Tang, C.M. (Eds.), Exceptional Fossil Preservation: A Unique View of Marine Life. Columbia University Press, New York.

Farrell, U.C., Briggs, D.E.G. , 2007. A Pyritized Polychaete from the Devonian of Ontario. proceedings of the Royal Society B: Biological Sciences 274, 499-504.

Farrell, U.C., Martin, M.J., Hagadorn, J.W., Whiteley, T., Briggs, D.E.G., 2009. Beyond Beecher's Trilobite Bed: Widespread pyritization of soft tissues in the Late Ordovician Taconic foreland basin. Geology 37, 907-910.

Frimmel, A., Oschmann, W., Schwark, L., 2004. Chemostratigraphy of the Posidonia Black Shale, SW Germany: Influence of sea-level variation on organic facies evolution. Chemical Geology 206, 199-230.

Gabbott, S.E., Norry, M.J., Aldridge, R.J., Theron, J.N., 2001. Preservation of fossils in clay minerals; a unique example from the Upper Ordovician Soom Shale, South Africa. Proceedings of the Yorkshire Geological Society 53, 237-244.

Gabbott, S.E., Xian-guang, H., Norry, M.J., Siveter, D.J., 2004. Preservation of Early Cambrian animals of the Chengjiang biota. Geology 32, 901-904.

Gaines, R.R., Briggs, D.E.G., Yuanlong, Z., 2008. Cambrian Burgess Shale–type deposits share a common mode of fossilization. Geology 36, 755-758.

Gaines, R.R., Droser, M.L., 2010. The paleoredox setting of Burgess Shale-type deposits. Palaeogeography, Palaeoclimatology, Palaeoecology 297, 649-661.

Gaines, R.R., Hammarlund, E.U., Hou, X., Qi, C., Gabbott, S.E., Zhao, Y., Peng, J., Canfield, D.E., 2012. Mechanism for Burgess Shale-type preservation. PNAS 109, 5180-5184.

Gaines, R.R., Kennedy, M.J., Droser, M.L., 2004. A new hypothesis for organic preservation of Burgess Shale taxa in the middle Cambrian Wheeler Formation, House Range, Utah. Palaeogeography, Palaeoclimatology, Palaeoecology 220, 193-205.

Garson, D.E., Gaines, R.R., Droser, M.L., Liddell, W.D., Sappen-Field, A., 2012. Dynamic palaeoredox and exceptional preservation in the Cambrian Spence Shale of Utah. Lethaia 45, 164-177.

Gehling, J.G., 1999. Microbial mats in terminal Proterozoic siliciclastics: Ediacaran death masks. Palaios 14, 40-57.

Gehling, J.G., Droser, M.L., Jensen, S., Runnegar, B.N., 2005. Ediacaran organisms: Relating form to function, in: Briggs, D.E.G. (Ed.), Evolving form and function: Fossils and Development, Proceedings of a Symposium Honoring Adolf Seilacher for his Contributions to Paleontology in celebration of his 80th birthday. Peabody Museum of Natural History, Yale University, New Haven, pp. 43-67.

Gill, B.C., Lyons, T.W., Jenkyns, H.C., 2011. A global perturbation to the sulfur cycle during the Toarcian Oceanic Anoxic Event. Earth and Planetary Science Letters 312, 484-496.

Gill, B.C., Lyons, T.W., Saltzman, M.R., 2007. Parallel, high-resolution carbon and sulfur isotope records of the evolving Paleozoic marine sulfur reservoir. Palaeogeography, Palaeoclimatology, Palaeoecology 256, 156-173.

Grimes, S.T., Brock, F., Rickard, D., Davies, K.L., Edwards, D., Briggs, D.E.G., Parkes, R.J., 2001. Understanding Fossilization: Experimental pyritization of plants. Geology 29, 123-126.

Hammarlund, E.U., Dahl, T.W., Harper, D.A.T., Bond, D.P.G., Nielsen, A.T., Bjerrum, C.J., Schovsbo, N.H., Schönlaubi, H.P., Zalasiewicz, J.A., Canfield, D.E., 2012. A sulfidic driver for the end-Ordovician mass extinction. Earth and Planetary Science Letters 331-332, 128-139.

Hagadorn, J.W., 2002. Burgess Shale-type localities: the global picture., in: Bottjer, D.J., Etter, W., Hagadorn, J.W., Tang, C.M. (Eds.), Exceptional Fossil Preservation: A Unique View of Marine Life. Columbia University Press, New York.

Hagadorn, J., Waggoner, B., 2000. Ediacaran fossils from the southwestern Great Basin, United States. Journal of Paleontology 74, 349-359.

Horita, J., Zimmermann, H., Holland, H.D., 2002. Chemical evolution of seawater during the Phanerozoic: Implications from the record of marine evaporites. Geochimica et Cosmochimica Acta 66, 3733-3756.

Jenkyns, H.C., 2010. Geochemistry of oceanic anoxic events. Geochemistry, Geophysics, Geosystems: G3 11, 1-30.

Kammer, T.W., Ausich, W.I., 2007. Soft-Tissue preservation of the hind gut in a new genus of cladid crinoid from the Mississippian (Visean, Asbian) at St. Andrews, Scotland. Palaeontology 50, 951-959.

Kok, M., Schouten, S., Damsté, J., 2000. Formation of insoluble, nonhydrolyzable, sulfur-rich macromolecules via incorporation of inorganic sulfur species into algal carbohydrates. Geochimica et Cosmochimica Acta 64, 2689-2699.

Lieberman, B.S., 2003. A new soft-bodied fauna: The Pioche Formation of Nevada. Journal of Paleontology 77, 674-690.

Lin, J., Zhao, Y., Rahman, I.A., Xiao, S., Wang, Y., 2010. Bioturbation in Burgess Shale-type *Lagerstatten* - Case study of trace fossil-body fossil association from the Kaili Biota (Cambrian Series 3), Guizhou, China. Palaeogeography, Palaeoclimatology, Palaeoecology 292, 245-256.

Lindgren, J., Everhart, M.J., Caldwell, M.W., 2011. Three-Dimensionally Preserved Integument Reveals Hydrodynamic Adaptations in the extinct marine lizard Ectenosaurus (Reptilia, Mosasauridae). PLoS One 6, e27343.

Liu, H.P., McKay, R.M., Young, J.N., Witzke, B.J., McVey, K.J., Liu, X., 2006. A new Lagerstätte from the Middle Ordovician St. Peter Formation in northeast Iowa, USA. Geology 34, 969-972.

Long, J.A., Trinajstic, K., Yong, G.C., Senden, T. 2008. Live birth in the Devonian period. Nature 453.

Lowenstein, T.K., Hardie, L.A., Timofeeff, M.N., Demicco, R.V., 2003. Secular variation in seawater chemistry and the origin of calcium chloride basinal brines. Geology 31, 857-860.

Loydell, D.K., Orr, P.J., Kearns, S.L., 2004. Preservation of soft tissues in Silurian graptolites from Latvia. Palaeontology 47, 503-513.

Lyons, T.W., Gill, B.C., 2009. The worm turned, and the ocean followed. PNAS 106, 8081-8082.

Martin, D., Briggs, D.E.G., Parkes, R.J., 2004. Experimental attachment of sediment particles to invertebrate eggs and the preservation of soft-bodied fossils. Journal of the Geological Society, London 161, 735-738.

McKirdy, D.M., Hall, P.A., Nedin, C., Halverson, G.P., Michaelson, B.H., Jago, J.B., Gehling, J.G., Jenkins, R.J.F, 2011. Paleoredox status and thermal alteration of the lower Cambrian (Series 2) Emu Bay Shale Lagerstatte, South Australia. Australian Journal of Earth Sciences 58, 259-272.

Moore, R.A., Lieberman, B.S., 2009. Preservation of early and Middle Cambrian soft-bodied arthropods from the Pioche Shale, Nevada, USA. Palaeogeography, Palaeoclimatology, Palaeoecology 277, 57-62.

Narbonne, G.M., 1998. The Ediacara biota: A terminal Neoproterozoic experiment in the evolution of life. GSA Today 8, 1-6.

Narbonne, G.M., 2005. The Ediacara biota: Neoproterozoic origin of animals and their ecosystems. Annual Review of Earth and Planetary Sciences 33, 421-442.

Newton, R.J., Reeves, E.P., Kafousia, N., Wignall, P.B., Bottrell, S.H., Sha, J.G., 2011. Low marine sulfate concentrations and the isolation of the European epicontinental sea during the Early Jurassic. Geology 39, 7-10.

Nudds, J., Selden, P., 2008. Fossil-Lagerstätten. Geology Today 24, 153-158.

Olcott Marshall, A., Wehrbein, R., Gonzalez, L., Lieberman, B., Lin, J., Marshall, C.P., in review. A molecular view of the Burgess Shale-type preservation mechanism.

Olcott Marshall, A., Wehrbein, R.L., Lieberman, B.S., Marshall, C.P., 2012. Raman spectroscopic investigations of Burgess Shale-type preservation: A new way forward. Palaios 27, 288-292.

Orr, P.J., Briggs, D.E.G., Kearns, S.L., 1998. Cambrian Burgess Shale Animals Replicated in Clay Minerals. Science 281, 1173-1175.

Page, A., Gabbott, S.E., Wilby, P.R., Zalasiewicz, J.A., 2008. Ubiquitous Burgess Shale–style "clay templates" in low-grade metamorphic mudrocks. Geology 36, 855-858.

Pallud, C., Van Cappellen, P, 2006. Kinetics of microbial sulfate reduction in estuarine sediments. Geochimica et Cosmochimica Acta 70, 1148-1162.

Paterson, J.R., Garcia-Bellido, D.C., Lee, M.S.Y., Brock, G.A., Jago, J.B., Edgecombe, G.D., 2011. Acute vision in the giant Cambrian predator *Anomalocaris* and the origin of compound eyes. Nature 480, 237-240.

Peters, S.E., 2007. The problem with the Paleozoic. Paleobiology 33, 165-181.

Petrovich, R., 2001. Mechanisms of fossilization of the soft-bodied and lightly armored faunas of the Burgess Shale and of some other classical localities. American Journal of Science 301, 683-726.

Petrulevičius, J.F., Wappler, T., Wedmann, S., Rust, J., Nel, A., 2008. New Megapodagrionid Damselflies (Odonata: Zygoptera) from the Paleogene of Europe. Journal of Paleontology 82, 1173-1181.

Powell, W., 2009. Comparison of geochemical and distinctive mineralogical features associated with the Kinzers and Burgess Shale formations and their associated units. Palaeogeography, Palaeoclimatology, Palaeoecology 277, 127-140.

Powell, W., Johnston, P.A., Collom, C.J., 2003. Geochemical evidence for oxygenated bottom waters during deposition of fossiliferous strata of the Burgess Shale Formation. Palaeogeography, Palaeoclimatology, Palaeoecology 201, 249-268.

Ronov, A.B., 1994. Phanerozoic transgressions and regressions on the continents: a quantitative approach based on areas flooded by the sea and areas of marine and continental deposition. American Journal of Science 294, 777-801.

Rothschild, B.M., Martin, L.D., 2003. Skeletal Impact of Disease. Bulletin of the New Mexico Museum of Natural History and Science 33, 1-226.

Sagemann, J., Bale, S.J., Briggs, D.E.G., Parkes, R.J., 1999. Controls on the formation of authigenic minerals in association with decaying organic matter: An experimental approach. Geochimica et Cosmochimica Acta 63, 1083-1095.

Sansom, R.S., Freedman, K., Gabbott, S.E., Aldridge, R.J., Purnell, M.A., 2010. Taphonomy and affinity of an enigmatic Silurian vertebrate, *Jamoytius kerwoodi* White. Palaeontology 53, 1393-1409.

Schiffbauer, J.D., Laflamme, M., 2012. Lagerstätten through time: A collection of exceptional preservational pathways from the terminal neoproterozoic through today. Palaios 27, 275-278.

Schopf, R.J.M., 1978. Fossilization potential of an intertidal fauna: Friday Harbor, Washington. Paleobiology 33, 165-181.

Selacher, A., 1970. Begriff und Bedeutung der Fossil-Lagerstätten: Neues Jahrbuch für Geologie und Paläontologie . Monatshefte 7, 34–39.

Selden, P.A., Nudds, J., 2004. Evolution of Fossil Ecosystems. Manson Publishing, London.

Sepkoski, J.J., Bambach, R.K., Raup, D.M., Valentine, J.W., 1981. Marine diversity and the fossil record. Nature 293, 435-437.

Shaw, A.B., 1955. Paleontology of Northwestern Vermont V. The Lower Cambrian Fauna. Journal of Paleontology 29, 775-805.

Shaw, A.B., 1962. Paleontology of Northwestern Vermont IX. Fauna of the Monkton Quartzite. Journal of Paleontology 36, 322-345.

Siveter, D., 2008. The Silurian Herefordshire Konservat-Lagerstätte: a unique window on the evolution of life. Proceedings of the Shropshire Geological Society 13, 58-61.

Siveter, D.J., Briggs, D.E.G., Sutton, M.D., 2010. An exceptionally preserved myodocopid ostracod from the Silurian of Herefordshire, UK. proceedings of the Royal Society B: Biological Sciences 277, 1539-1544.

Skinner, E.S., 2005. Taphonomy and depositional circumstances of exceptionally preserved fossils from the Kinzers Formation (Cambrian), southeastern Pennsylvania. Palaeogeography, Palaeoclimatology, Palaeoecology 220, 167-192.

Smith, D.A., 2012. Exceptional preservation of insects in lacustrine environments. Palaios 27, 346-353.

Steiner, M., Zhu, M., Zhao, Y., Erdtmann, B.-D., 2005. Lower Cambrian Burgess Shale-type fossil associations of South China. Palaeogeography, Palaeoclimatology, Palaeoecology 220, 129-152.

Sutton, M.D., Briggs, D.E.G., Siveter, D.J., Siveter, D.J., 2005. Silurian brachiopods with soft-tissue preservation. Nature 436, 1013-1015.

Takashima, R., Nishi, H., Huber, B.T., Leckie, R.M., 2006. Greenhouse world and the Mesozoic ocean. Oceanography 19, 64-74.

Tanabe, K., Mapes, R., Sasaki, T., Landman, N., 2000. Soft-part anatomy of the siphuncle in Permian prolecanitid ammonoids. Lethaia 33, 83-91.

Thompson, C.K., Kah, L.C., 2012. Sulfur isotope evidence for widespread euxinia and a fluctuating oxycline in Early to Middle Ordovician greenhouse oceans. Palaeogeography, Palaeoclimatology, Palaeoecology 313-314, 189-214.

Van Roy, P., Orr, P.J., Botting, J.P., Muir, L.A., Vinther, J., Lefebvre, B., el Hariri, K., Briggs, D.E.G., 2010. Ordovician faunas of Burgess Shale type. Nature 465, 215-218.

von Bitter, P.H., Purnell, M.A., Tetreault, D.K., Stott, C.A., 2007. Eramosa Lagerstätte—Exceptionally preserved soft-bodied biotas with shallow-marine shelly and bioturbating organisms (Silurian, Ontario, Canada). Geology 35, 879-882.

Wakeham, S., Damsté, J., Kohnen, M., Deleeuw, J., 1995. Organic sulfur-compounds formed during early diagenesis in Black-Sea sediments. Geochimica et Cosmochimica Acta 59, 521-533.

Williams, M.E., 1998. A new specimen of *Tamiobatis vetustus* (Chondrichthyes, Ctenacanthoidea) from the Late Devonian Cleveland Shale of Ohio. Journal of Vertebrate Paleontology 18, 251-260.

Young, G.A., Rudkin, D.M., Dobrzanski, E.P., Robson, S.P., Nowlan, G.S., 2007. Exceptionally preserved Late Ordovician biotas from Manitoba, Canada. Geology 35, 883-886.

Zhang, X., Shu, D., Li, Y., Han, J., 2001. New sites of Chengjiang fossils: Crucial windows on the Cambrian explosion. Journal of the Geological Society, London

Figures

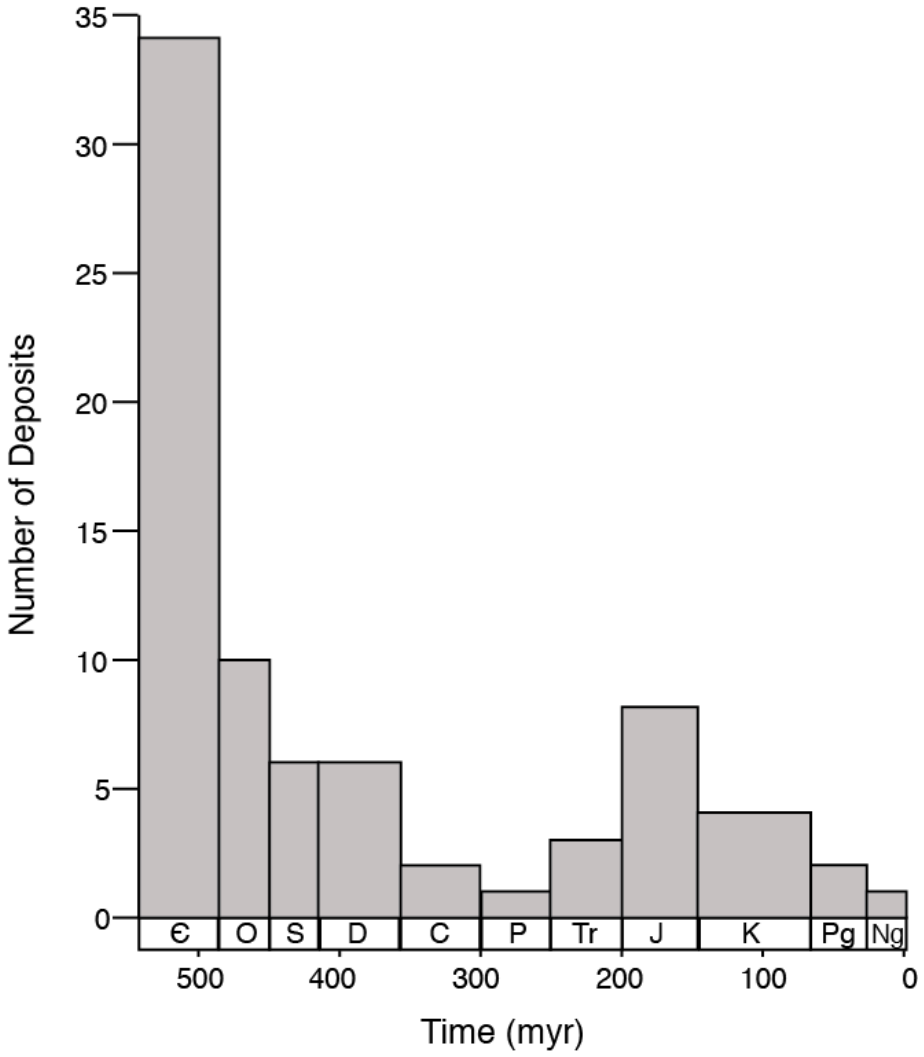

Figure 1: Secular distribution of Phanerozoic marine *Konservat-Lagerstätten* listed in Table 1.

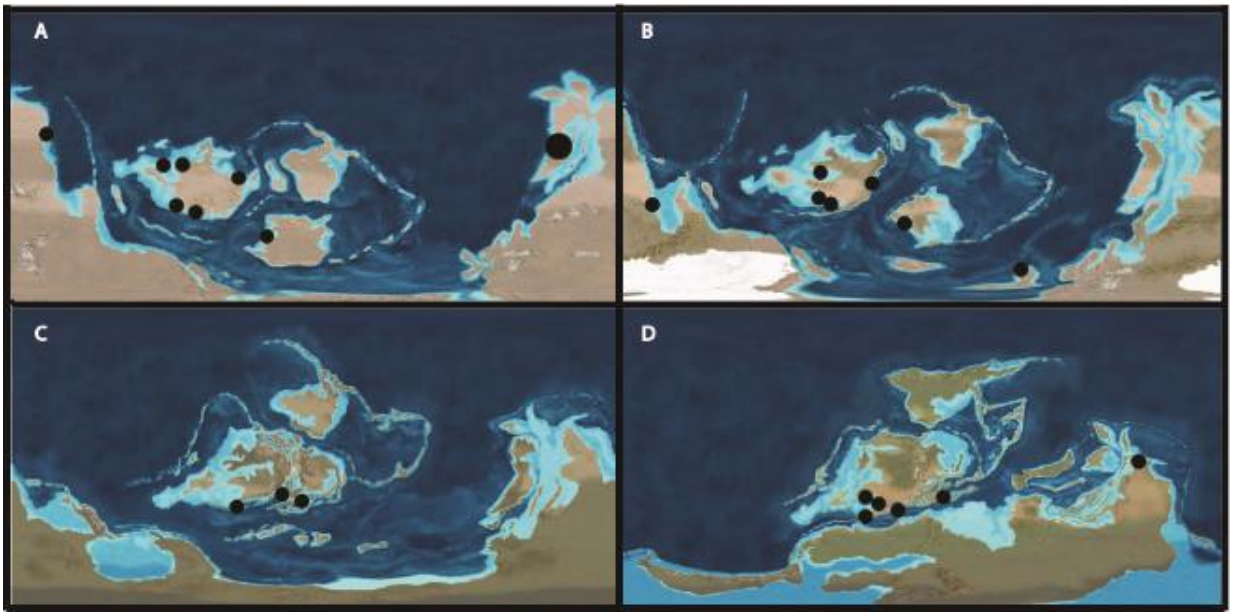

Figure 2: Paleogeographic distributions of Paleozoic *Konservat-Lagerstätten.* A. Cambrian B. Ordovician C. Silurian D. Devonian. Paleogeographic maps modified from Blakey (2003) and Blakey (Available at http://cpgeosystems.com/paleomaps.html).

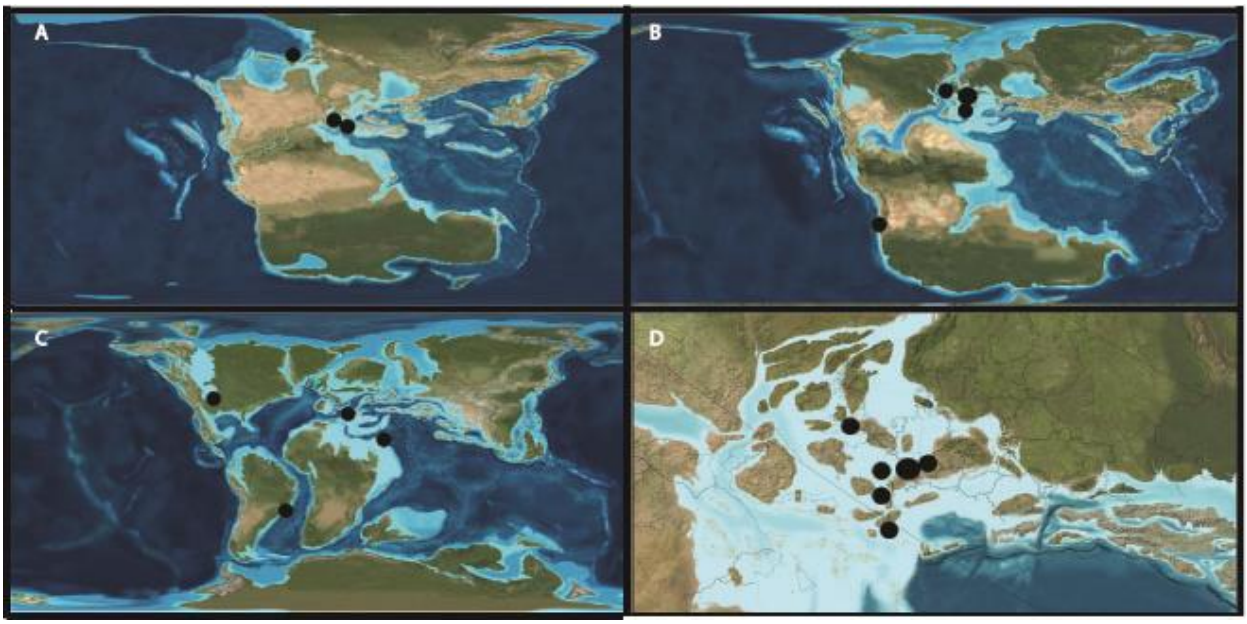

Figure 3: Geographic distribution of Mesozoic marine *Konservat-Lagerstätten*. A. Triassic B. Jurassic C. Cretaceous. D. Enlarged view of Jurassic Europe. Modified from Blakey, 2003 and Blakey, R.C., Available at http://cpgeosystems.com/paleomaps.html.

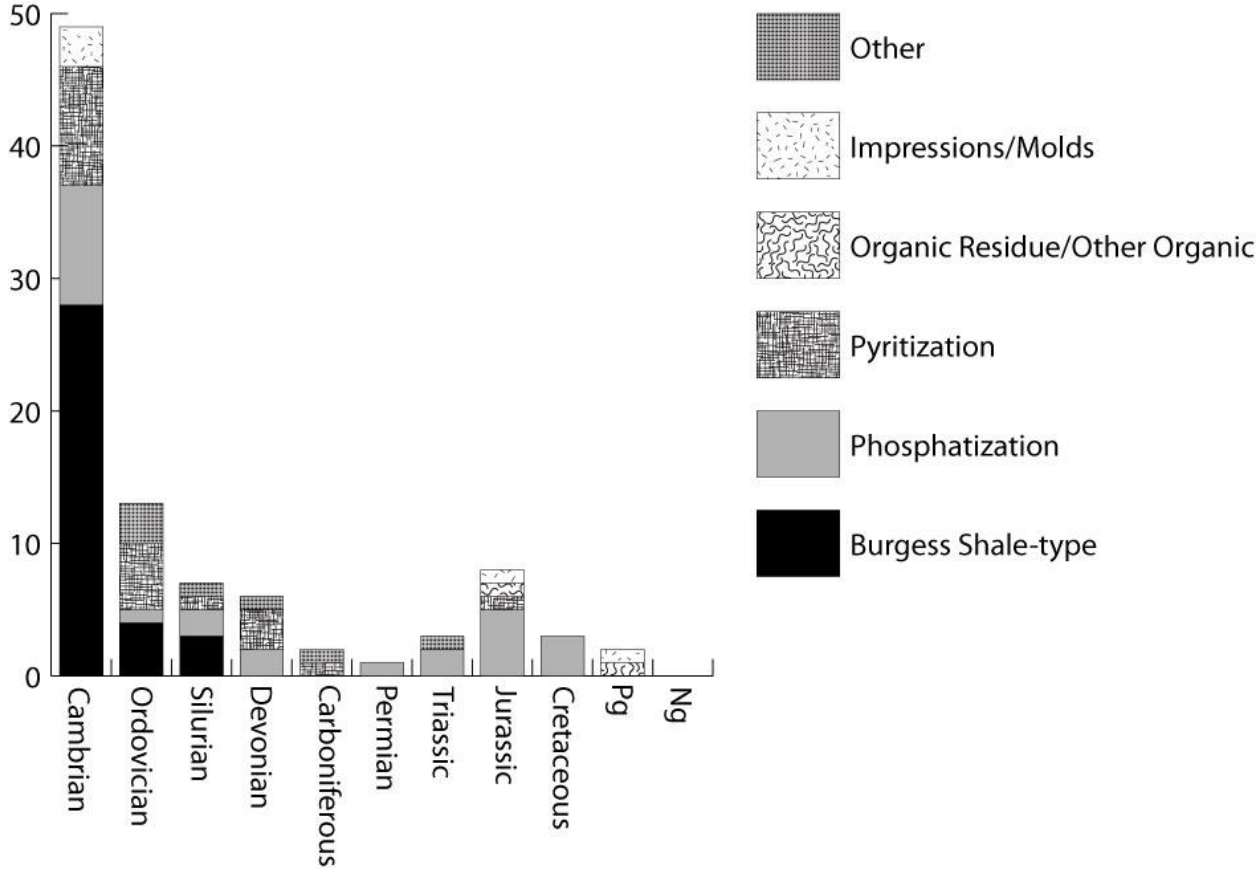

Figure 4: Styles of preservation for marine *Konservat-Lagerstätten* where taphonomic data is available. Where multiple styles of preservation are present in a single locality all are represented.

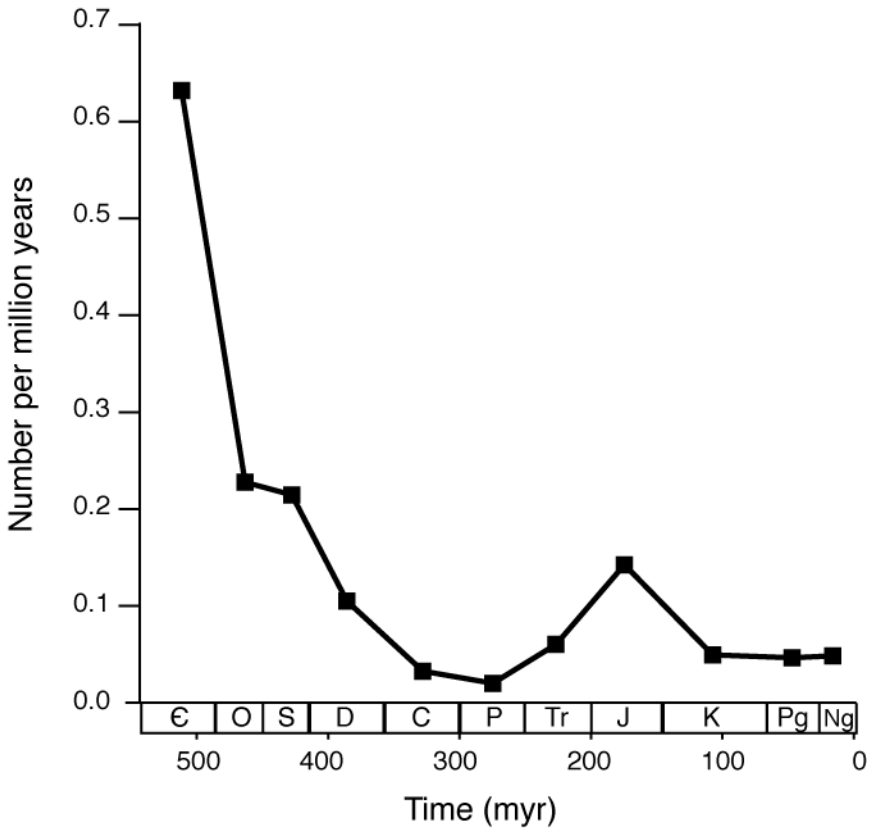

Figure 5: Rate of formation of *Konservat-Lagerstätten* per million years for each period of the Phanerozoic.

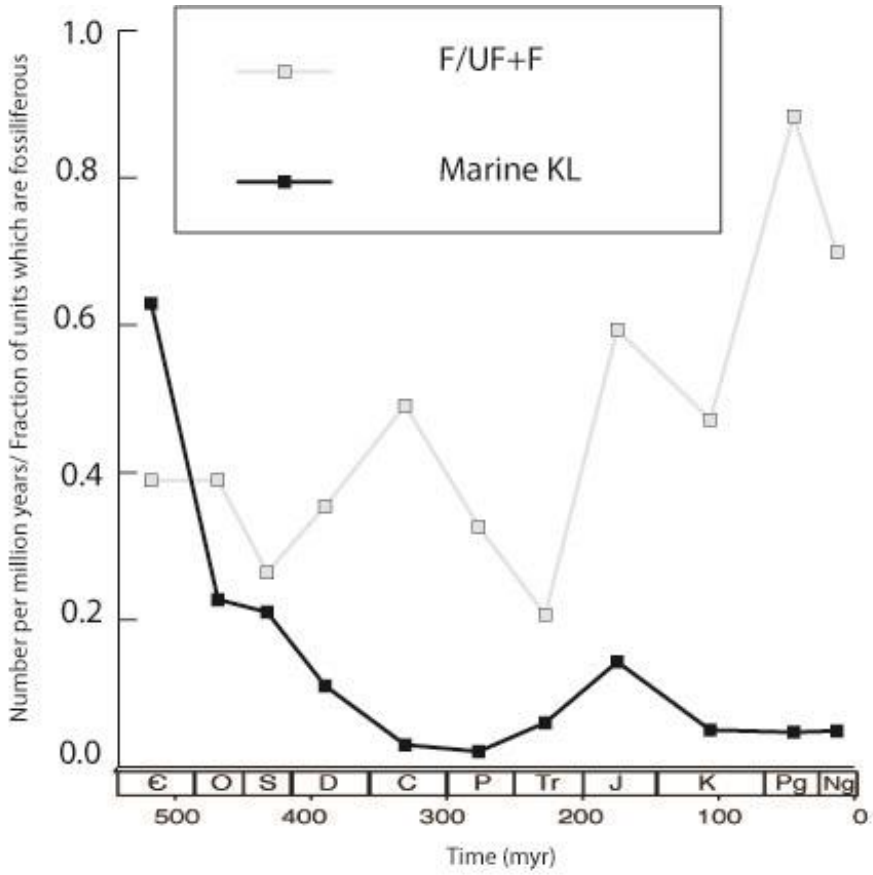

Figure 6: Marine *Konservat-Lagerstätten*/Ma (black) plotted with the fraction of units for each time period which are fossiliferous according to a georef search (gray), modified from Peters, 2007.

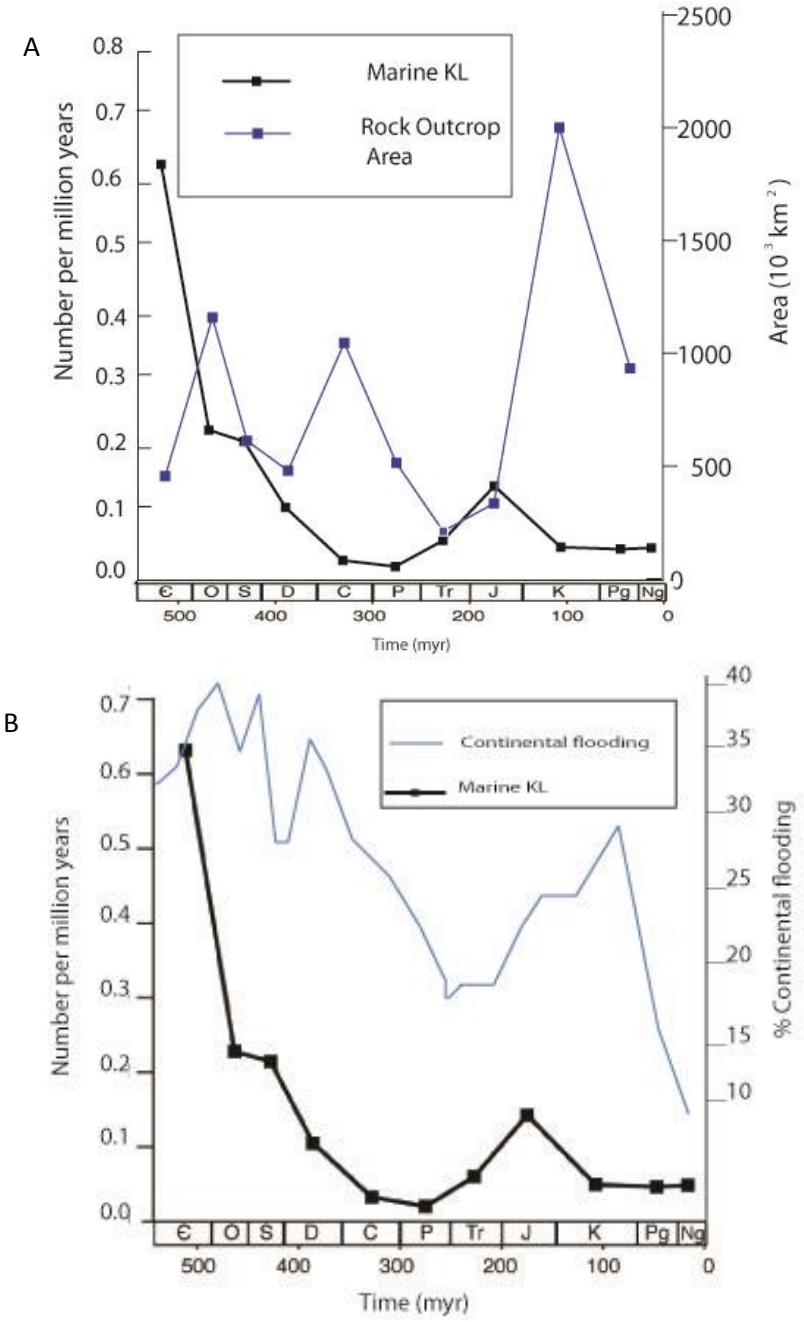

Figure 7: A. Marine *Konservat-Lagerstätten*/Ma (black) plotted with estimates of North American and European nonmetamorphosed marine sedimentary rock outcrop area modified from Allison and Briggs (1993). B. Marine *Konservat-Lagerstätten*/Ma (black) plotted with estimates of percent continental flooding (blue) modified from Ronov (1994).

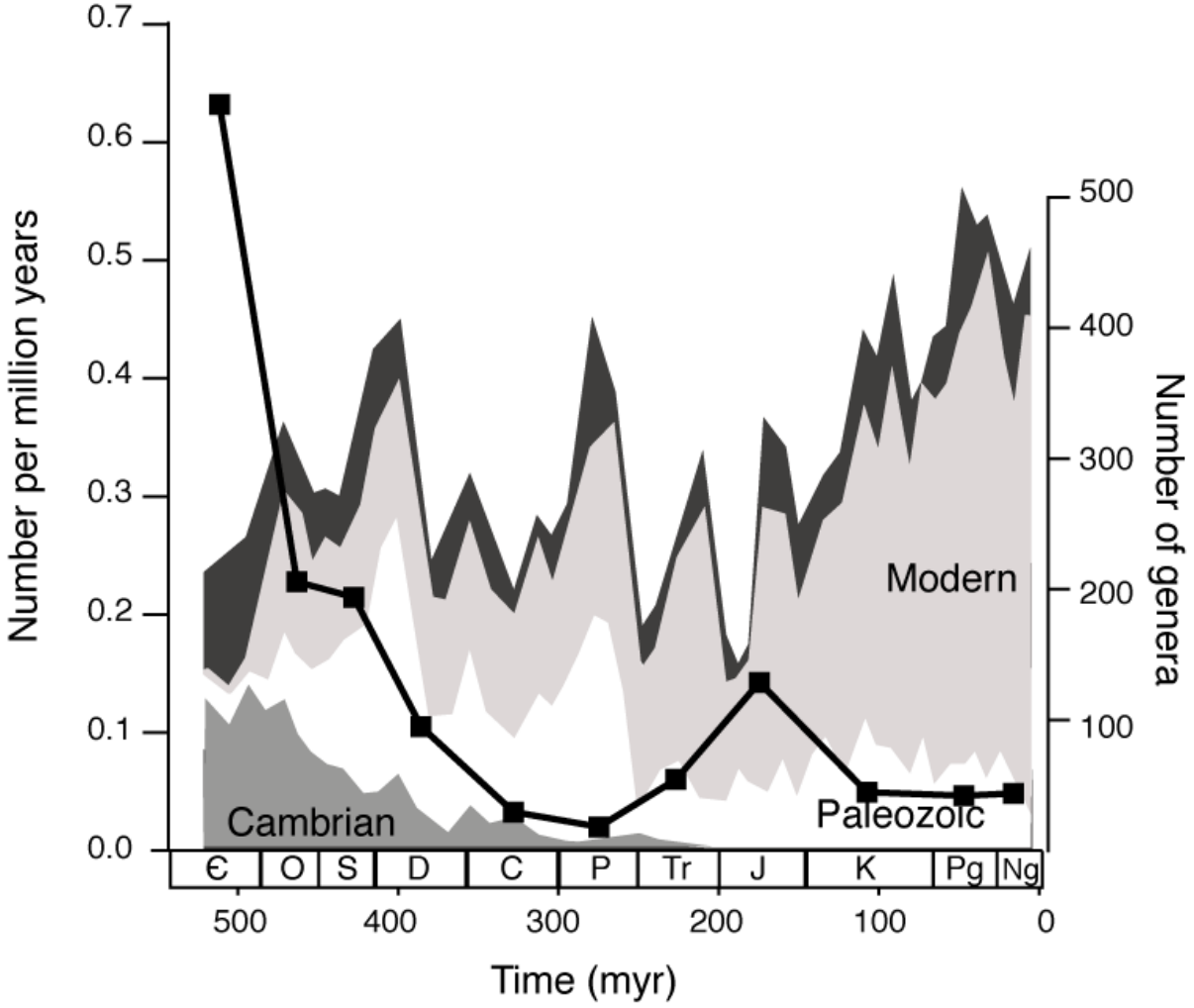

Figure 8: Marine *Konservat-Lagerstätten*/Ma (black) plotted with a sampling-standardized Phanerozoic diversity curve for Sepkoski's three marine evolutionary faunas (modified from Alroy, 2010).

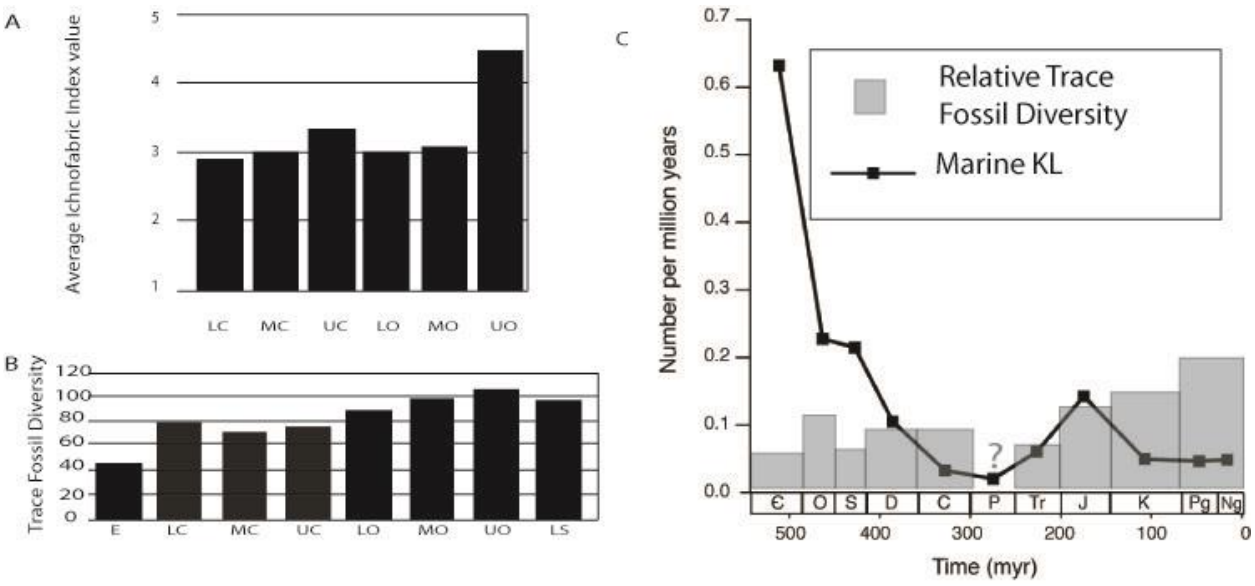

Figure 9: Trace fossil diversity through time. A. Average ichnofabric index in carbonate sediments from the Great Basin from the Lower Cambrian through the Upper Ordovician. (LC= Lower Cambrian, MC= Upper Cambrian, LO= Lower Ordovician, MO= Middle Ordovician, UO= Upper Ordovician, LS= Lower Silurian) Modified from Droser and Bottjer (1993). B. Total trace fossil diversity changes from the Ediacaran through the Lower Silurian (E= Ediacaran, LC= Lower Cambrian, MC= Upper Cambrian, LO= Lower Ordovician, MO= Middle Ordovician, UO= Upper Ordovician, LS= Lower Silurian). Modified from Crimes and Droser (1992). C. Number of *Konservat-Lagerstätten* per million years compared with changes in trace fossil diversity over the Phanerozoic. No data were available from the Permian. Modified from Sepkoski et al. (1981).

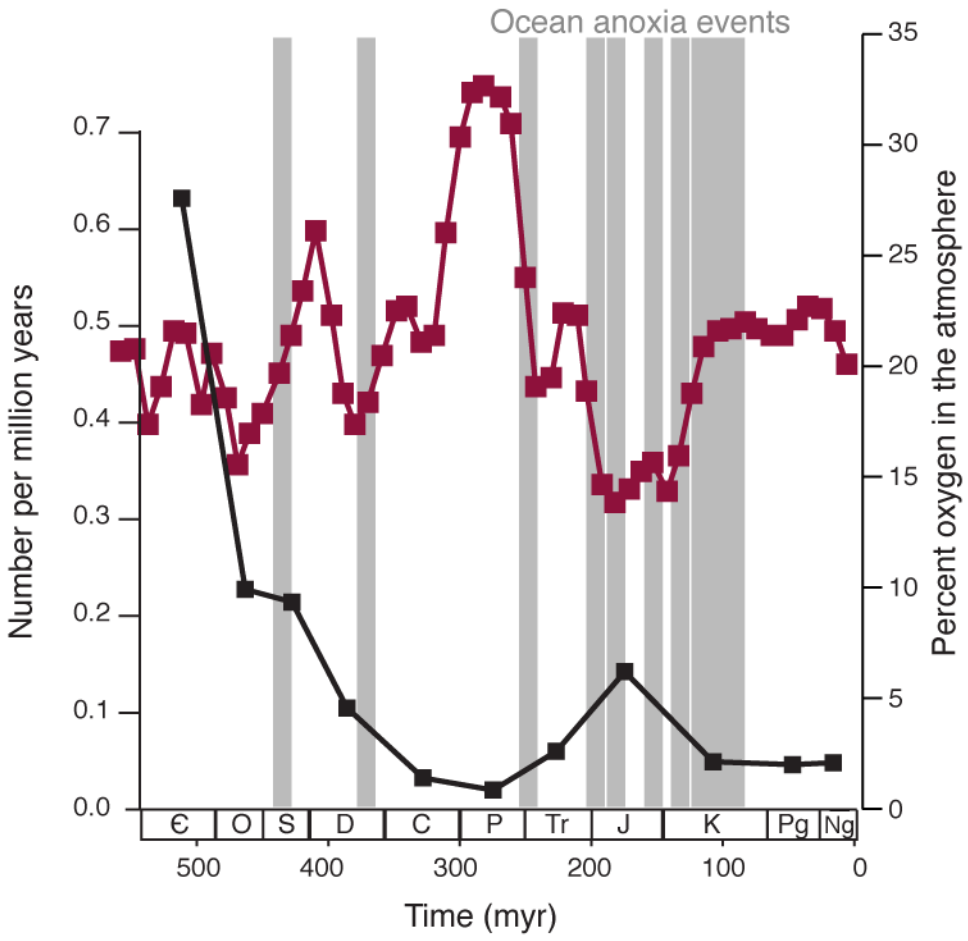

Figure10: Marine *Konservat-Lagerstätten*/Ma (black) plotted with estimates for global atmospheric oxygen derived from the GeoCarbSulf model of Berner, 2009 (red) and marine anoxia events (gray). Ages of ocean anoxia events from Bond et al. (2004) Takashima et al. (2006) and Jenkyns (2010).

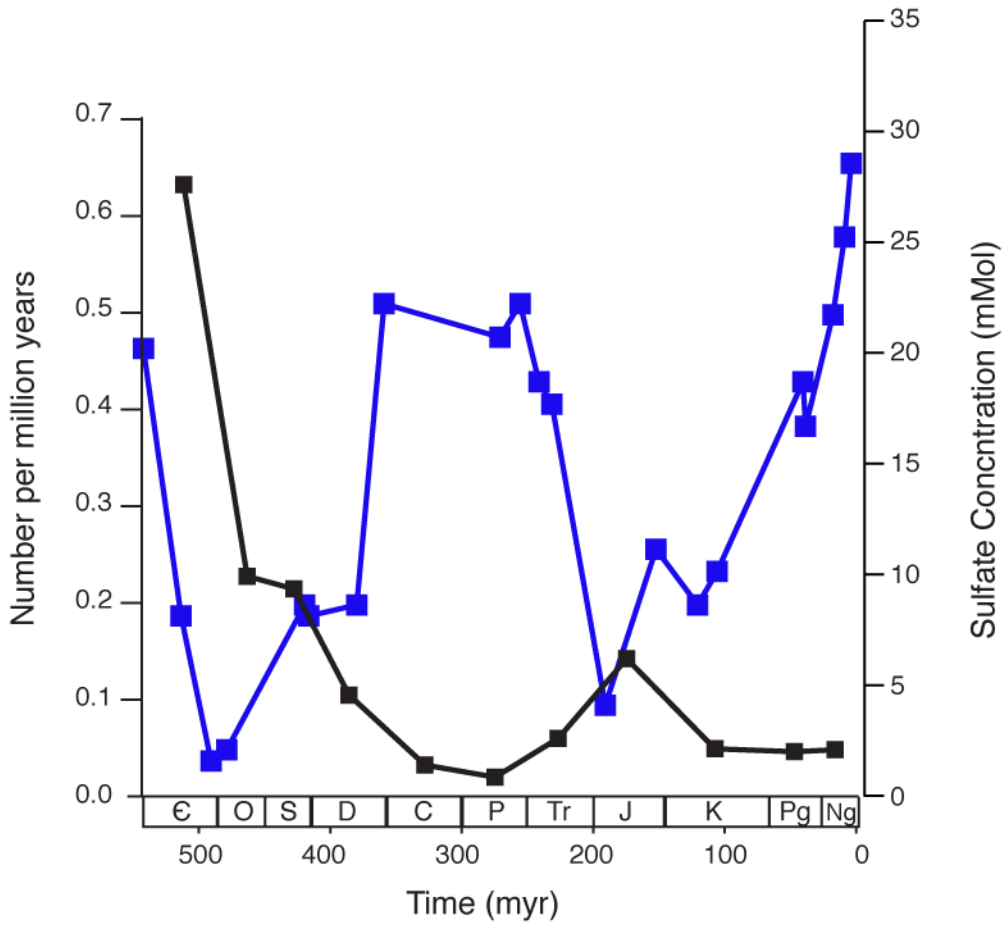

Figure11: Rate of *Konservat-Lagerstätten* formation (black) and estimated marine sulfate concentration (blue). Sulfate data from Lowenstein et al., 2003 (some data previously reported in Horita et al., 2002), Gill et al., 2007, Newton et al., 2010 , Gill et al., 2011 and Thompson and Kah, 2012.

Table 1: Phanerozoic Marine *Konservat-Laggerstätten*. BST= Burgess Shale-type.

DEPOSIT	AGE	ENVIRONMENT	PRIMARY MODE OF PRESERVATION	EXAMPLE REFERENCES	LOCATION
Anning	Cambrian	Marine	BST and pyritized	Zhang et al., 2001	China
Balang (Kaili Fm)	Cambrian	Marine	BST	Gaines et al., 2008	China
Bianmachong Fm	Cambrian	Marine	Iron oxide, some phosphatized	Steiner et al., 2005	China
Buen Fm (Sirius Passet Fauna)	Cambrian	Marine	BST, some phosphatized muscle and gut tissue (now silica)	Butterfield, 1995; Butterfield, 2002	Greenland
Burgess Shale (Stephen Fm)	Cambrian	Marine	BST, Some phosphatized tissue	Butterfield, 1995	Canada
Cengong (10km SE of Cengong, E Guizhou)	Cambrian	Marine	BST	Steiner et al., 2005	China
Chengjiang (Maotianshan Shale, Maanshan, Xiaolantian and Dapotou)	Cambrian	Marine	BST, pyritized, phosphatized	Steiner et al., 2005; Gabbott et al., 2004	China
Dayong	Cambrian	Marine	Iron oxide, some phosphatized	Steiner et al., 2005	China
Deze	Cambrian	Marine	BST	Steiner et al., 2005	China
Emu Bay Shale	Cambrian	Marine	BST and Iron oxide (after pyrite); some phosphatized	McKirdy et al., 2011	Australia
Haikou (Ercaicun, Mafang, Dazicun)	Cambrian	Marine	BST	Steiner et al., 2005	China
Jinning (Meishucun/ Badaowan)	Cambrian	Marine	BST	Steiner et al., 2005	China
Kaili	Cambrian	Marine	BST, Iron oxides (after pyrite)	Butterfield, 1995	China
Kinzers	Cambrian	Marine	BST, pyritized	Butterfield, 1995	USA
Latham Shale	Cambrian	Marine	BST	Hagadorn, 2002	USA

Marjum Fm	Cambrian	Marine	BST, some phosphatized	Butterfield, 1995	USA
Metaline Fm	Cambrian	Marine	BST	Gaines et al., 2008	USA
Mount Cap	Cambrian	Marine	BST	Butterfield, 1995	Canada
Nazhang (Malong County, Canglangpu Fm)	Cambrian	Marine	BST and pyritized	Steiner et al., 2005	China
Niutitang Fm (Zhongnan, Zunyi)	Cambrian	Marine	BST	Steiner et al., 2005	China
Orsten Anthraconites (Alum Shale Fm.)	Cambrian	Marine	Phosphatized in calcareous nodules	Allison and Briggs, 1991b	Sweden
Parker Slate	Cambrian	Marine	Impressions and Molds	Shaw, 1955; Shaw, 1962	USA
Pioche	Cambrian	Marine	BST, iron oxides	Lieberman, 2003; Moore and Lieberman, 2009	USA
Poleta Fm (White Mountains)	Cambrian	Marine	Impressions	Hagadorn, 2002	USA
Qujing county locality	Cambrian	Marine	BST	Steiner et al., 2005	China
Sapushan (Wuding County)	Cambrian	Marine	BST	Steiner et al., 2005	China
Spence Shale (Langston Fm)	Cambrian	Marine	BST, some phosphatized	Butterfield, 1995	USA
“Thin” Stephen Fm	Cambrian	Marine	BST	Caron et al., 2010	Canada
Wheeler Fm	Cambrian	Marine	BST	Butterfield, 1995	USA
Wood Canyon Fm. (Salt Spring Hills, Kelso Mountains)	Cambrian	Marine	Impressions	Hagadorn and Waggoner, 2000; Hagadorn, 2002	USA
Wulongqing Fm	Cambrian	Marine	BST	Steiner et al., 2005	China
Zawiszany Fm. (NE Poland)	Cambrian	Marine	BST	Dzik and Lendzion, 1988	Poland
Zawiszyn Fm	Cambrian	Marine	BST	Hagadorn, 2002	Poland
Zhongnan (Zunyi, Guizhou)	Cambrian	Marine	BST	Steiner et al., 2005	China
Airport Cove	Ordovician	Marine	BST	Young et al., 2007	Canada
Fezouata Biota	Ordovician	Marine	BST Carbonaceous compressions associated with iron oxide pyrite pseudomorphs,	Van Roy et al., 2010	Morocco

			large siliceous concretions		
Frankfort Shale (Beecher's Bed and Jo's quarry)	Ordovician	Marine	Pyritized	Allison and Briggs, 1991b	USA
Llanfawr Mudstones	Ordovician	Marine	Pyritized	Botting and Muir, 2008	UK
Oland	Ordovician	Marine	Phosphatized	Allison and Briggs, 1991b	Sweden
Soom Shale	Ordovician	Marine	Clay replacement of carbonaceous material	Hagadorn, 2002	South Africa
Walcott Rust	Ordovician	Marine	Some calcified Trilobite appendages	Brett et al., 2012	USA
Whetstone Gulf Fm. (Martin Quarry)	Ordovician	Marine	Pyritized	Farrell et al., 2009	USA
William Lake	Ordovician	Restricted marine	Molds, dolomite or pyrite replacement	Young et al., 2007	Canada
Winneshiek (St. Peter Fm.)	Ordovician	Restricted marine	BST	Liu et al., 2006	USA
Herefordshire	Silurian	Marine	Calcite in nodules	Siveter et al., 2010	UK
Downtown Castle Sandstone Fm (Much Wenlock, Shropshire)	Silurian	Restricted marine	Phosphatized	Allison and Briggs, 1991b	UK
Eramosa	Silurian	Marine	Phosphatized and BST Carbonaceous Compressions (Sulphurized) each dominate in different localities	von Bitter et al., 2007	Canada
Lesmahagow	Silurian	Restricted marine	BST	Sansom et al., 2010	UK
Dobele Fm	Silurian	Marine	2D Carbonaceous compressions in pyritized rhabdosomes	Loydell et al., 2004	Latvia
Saaremaa	Silurian	Restricted marine	No published taphonomic data found	Allison and Briggs, 1991b	Estonia
Arkona Shale	Devonian	Marine	Pyritized	Farrell and Briggs, 2007	Canada
Carnic Alps	Devonian	Marine	Phosphatized	Allison and Briggs, 1991b	Italy
Cleveland Shale	Devonian	Marine	Calcified Cartilage	Allison and Briggs, 1991b; Williams, 1998	USA

Gogo Fm	Devonian	Marine	Phosphatized	Long et al., 2008	Australia
Hunsruck	Devonian	Marine	Pyritized	Selden and Nudds, 2004	Germany
Wissenbach	Devonian	Marine	Pyritized	Allison and Briggs, 1993	Germany
Bearsden (Manse Burn Fm, Shrimp Member)	Carboniferous	Marine	Cartilage/calcified cartilage	Allison and Briggs, 1991b	UK
St. Andrews (Witch Lake)	Carboniferous	Marine	Iron oxide (inferred, after pyrite, one fossil)	Kammer and Ausich, 2007	UK
Buck Mountain (Arcturus Fm)	Permian	Marine	Phosphatized	Tanabe et al., 2000	USA
Monte San Giorgio	Triassic	Restri	Articulated skeletons, Calcified Cartilage, rarely phosphatized digestive tracts	Etter, 2002	Switzerland/ Italy
Spitsbergen	Triassic	Marine	Phosphatized	Allison and Briggs, 1991b	Svalbard
Montral-Alcovar	Triassic	Restricted marine	No published taphonomic data found	Allison and Briggs, 1991b	Spain
Cerin	Jurassic	Restricted Marine	Phosphatized beneath microbial mats	Allison and Briggs, 1991b	France
Christian Malford (Oxford clay)	Jurassic	Marine	Phosphatized	Allison and Briggs, 1991b	UK
Cordillera de Domeyko	Jurassic	Marine	Phosphatized	Allison and Briggs, 1991b	Chile
Holzmaden (Posidonienschiefer/ Posidonia shale)	Jurassic	Marine	(Rarely) preserved skin outlining articulated skeletons	Frimmel et al., 2004	Germany
Nusplingen	Jurassic	Restricted Marine	Phosphatized	Briggs et al., 2005	Germany
Osteno	Jurassic	Marine	Phosphatized	Allison and Briggs, 1991b	Italy
Solnhofen	Jurassic	Restricted marine	Impressions, possibly associated with bacterial films	Selden and Nudds, 2004	Germany

Voulte-sur-Rhone	Jurassic	Marine (epicontinental)	Pyritized	Allison and Briggs, 1991b	France
Hakel	Cretaceous	Marine	Phosphatized	Allison and Briggs, 1991a	Lebanon
Santana	Cretaceous	Marine	Phosphatized (cryptocrystaline francolite) in carbonate concretions	Allison and Briggs, 1991b	Brazil
Smoky Hill Chalk (Niobara)	Cretaceous	Marine	Phosphatized	Lindgren et al., 2011	USA
Hvar	Cretaceous	Intertidal Restricted Marine	No published taphonomic data found	Allison and Briggs, 1991b	Croatia
Fur Fm. (Mo Clay)	Eocene	Marine	Imprints of insects	Petrulevičius et al., 2008; Bertelli et al., 2011	Denmark
Monte Bolca	Eocene	Restricted marine or lagoonal	Organic material appears to be preserved but preservational mechanism has not been well studied	Allison and Briggs, 1991b	Italy
Chita (Morozaki Fm)	Miocene	Marine	No published taphonomic data found	Allison and Briggs, 1991b	Japan

Chapter 3

Paleopathological investigations utilizing Raman microspectroscopy

1. Introduction

1.1 Paleopathology

Paleopathology, as defined by Sir Armand Ruffer in 1913, is the "science of the diseases which can be demonstrated in human and animal remains in ancient times" (Swinton, 1981, Rothschild and Martin, 2006). According to Waldron (1995), the term may have been first used by Dr. Schufeldt in Popular Science Monthly in 1893, but Sir Ruffer is regarded as the father of the field (Rothschild and Martin, 2006). Paleopathology bridges the gap between human and veterinary medicine and paleontology and has been particularly useful for the field of epidemiology (Rothschild and Martin, 2006). Studying the paleontological and archeological history of a disease may provide insights into the nature and transmission of the disease which are difficult to resolve from modern data alone (e.g. the discovery of the likely origin of rheumatoid arthritis in a highly localized area of pre-Columbian North America) (Rothschild and Woods, 1990, Rothschild and Martin, 2006). The hypothesis that natural selection may favor more benign pathogens, as suggested by Ewald (1988) but considered controversial by Rothschild and Martin (2006), has also been tested with information from paleopathologic studies. Information on posture and gait can be garnered from the study of pathological information (Rothschild and Martin, 2006). In addition, the study of paleopathology also allows some evidence for diet and behavior to be gleaned from the fossil record which may otherwise have remained speculative (Rothschild and Martin, 2006, Rothschild and Storrs, 2003, Rothschild, 2011, Rothschild et al., 2012, Dominguez-Rodrigo et al. 2012).

In this study Raman spectroscopy was used to examine three pathologies. A section of skull from a human suffering from porotic hyperostosis from the Wedda archaeological site in Sri Lanka was characterized with respect to mineralogical changes associated with pore formation. The tibia of a modern artiodactyl suffering from osteomyelitis was also examined. A spherical mass from the Oligocene Cedar Creek formation represented a possible urolith and Raman microspectroscopy was utilized to determine whether the sample was biogenic or abiotically generated.

However, paleopathology has its own limitations. In nearly all cases, diagnoses must be made based on skeletal data alone (although soft tissues are occasionally preserved in the fossil record as documented in chapter 2). Additionally, it is important to properly distinguish pathologies from taphonomic effects (Rothschild and Martin, 2006). Confusing subtle changes with diagenesis may lead to an underestimation of disease frequencies or distributions (Rothschild and Rothschild, 1999, Rothschild and Martin, 2006). The ease of discriminating between pathology and taphonomic effects in part depends upon the nature of the pathology. Osteoarthritis exposes trabecular bone through abrasion in a manner indistinguishable from taphonomic processes (Rothschild, 2013). Common taphonomic effects include shrinkage cracks, damage from scavengers, crushing and chemical alteration from interaction with groundwater (Trueman et al., 2002, Rothschild and Martin, 2006, Thomas et al., 2007). When exposed bones desiccate shrinking collagen results in the formation of cracks following the bone fabric (Rothschild and Martin, 2006). These cracks can subsequently be sites of frost wedging, reducing the bone to shards (Rothschild and Martin, 2006). Gnawing results in bone shards being pressed into the toothmarks, and is typically localized to the ends of bones (Rothschild and Martin, 2006). Insects, such as dermestid beetles, may also leave holes or depressions in bone,

which may exhibit shallow, sinuous grooves from mandibular "gnawing" (Roberts and Rogers, 1997, Rothschild and Martin, 2006). Taphonomic crushing results in a pattern of fractures across the entire fossil, including a distinctive pattern of microfractures with all fractures corresponding to one loading pattern (Rothschild and Martin, 2006). It is also related to the lithology of the matrix. Sandstones typically resist compression while shales are more prone to compression (Rothschild and Martin, 2006). Crushing in limestones depends on clay content and rate of lithification (Rothschild and Martin, 2006). Taphonomic processes of course do not lead to the formation of reactive bone tissue (intramembranous bone formed in response to stress which may be lamellar or woven) (Rubin and Strayer, 2011, Rothschild, 2013).

Despite these limitations some conditions have been successfully studied not only in archaeological and subfossil (a term applied to samples dating from 1000 to 5000 years before present) remains but also in several Mesozoic clades (Tanke and Rothschild, 2002, Rothschild and Martin, 2006). Bone injury and repair has been documented in every major dinosaur clade (Tanke and Rothschild, 2002, Straight et al., 2009). Straight et al. (2009) were able to determine that hadrosaurs repaired damaged bones by filling the breaks with cartilaginous tissue that can then mineralize, similar to repair mechanisms in many reptiles, but not birds, which fill fractures with solid fibrous tissue instead. By screening Tyrannosaurid phalanges held at the Royal Tyrrel Museum, Rothschild et al. (1997) were able to determine that Tyrannosaurids may have suffered from gout at rates similar to those observed in birds (Schlumberger, 1959).

Pathologies related to decompression syndrome have been noted in ichthyosaurs and plesiosaurs (Rothschild et al., 1997, Straight et al., 2009, Rothschild et al., 2003, Rothschild and Storrs, 2003, Rothschild et al., 2012). Decompression syndrome, commonly called caisson's disease or 'the bends,' can cause areas of bone subsidence identifiable in the fossil record

(Rothschild and Storrs, 2003). This pathology has been recognized in mosasaurs, plesiosaurs, ichthyosaurs and fossil turtles (Rothschild and Martin, 1987, Rothschild and Storrs, 2003, Rothschild et al., 2012). As organisms are only susceptible to this disease if they are repetitive deep divers or rapidly change depths this pathology has been particularly useful for inferring behavior. Ichthyosaurs, in contrast, show a distinct increase in incidence of avascular necrosis in the Late Jurassic and Cretaceous when compared with the Triassic and Early Jurassic, indicating an absence of physiological adaptations to diving in this group while rapid depth changes became more common (Rothschild et al., 2012). Rothschild et al. (2012) attribute this to the evolution of large, fast predators, such as advanced sharks, in the Late Jurassic as well as the radiation of fast-swimming, agile teleost fish as a potential prey item. The absence of adaptations to protect against decompression syndrome, such as those found in modern cetaceans, may in turn have contributed to the extinction of these organisms (Rothschild et al., 2012). These studies have provided insights into the predispositions of certain taxa to diseases, environmental and evolutionary pressures.

1.2 Bone Structure

Bones contain both organic and mineral phases. The organic matrix is primarily collagen with lesser amounts of non-collagenous proteins, which are nevertheless essential to the mineralization process (Boskey, 2007). Spaces between individual collagen molecules and fibrils accommodate the mineral particles of bone (Hodge, 1989, Boskey, 2007). Specialized cells called osteoblasts are responsible for mineralizing this extracellular collagen matrix of bone (Boskey, 2007). These cells then transform into osteocytes when engulfed in minerals. Osteoclasts are specialized cells which remove bone minerals and matrix, regulating the resorption of bone (Boskey, 2007). The mineral crystals of bone are platy hydroxylapatite

[$(Ca)_{10}(PO_4)_6(OH)_2$] and have lengths of 20-50 nm and widths of 12-20 nm (Glimcher, 2006, Boskey, 2007). The initial crystals appear to be round, growing longer with age with the long *c*-axes of apatite crystals parallel to the axis of the associated collagen fibril (Boskey, 2007, Hong et al., 2009). The only phase present is highly substituted apatite in all but the youngest bone, where amorphous calcium phosphate is present (Boskey, 2007). Biologic hydroxylapatite is distinct from geologic hydroxylapatite in its small crystal size, high degree of CO_3^{2-} substitution, OH^- deficiency and increased solubility (Boskey, 2007).

At the macroscale, the long bones consist of a flat cylinder of cortical (compact) bone surrounding trabecular (cancellous bone) (Figure 2). Other bones vary in structure (e.g. the skull typically has less trabecular bone, while vertebrae are primarily trabecular bone) (Rothschild and Martin, 2006, Boskey, 2007). The exterior surface of the cortex is termed the periosteum, which appears amorphous (except for penetrating vascular structures) with underlying lamellar (presenting as concentric layers) bone in some reptiles (Rothschild and Martin, 2006). The individual struts within marrow are termed trabeculae (Boskey, 2007). The thin plates within cortical bone are termed lamellae (Boskey, 2007). The bone surrounding blood vessels is termed an osteon unit (Boskey, 2007). Trabeculae appear to be oriented randomly but are known to be aligned along principle stress directions as a result of cells forming and resorbing bone due to functional stimuli (Martin et al., 1998, Hong et al., 2009). Minerals are deposited onto the collagen matrix either through intramembranous ossification, involving the mineralization of fibrous tissue, or by endochondral ossification, involving the digestion and replacement of calcified cartilaginous tissue (Stewart et al., 2002, Rothschild and Martin, 2006). Endochondral ossification occurs in most bones while intramembranous ossification occurs in the formation of the flat bones of the skull (calvaria) and in injury repair (Stewart et al., 2002). The mineral to

matrix ratio in cortical bone is higher than in trabecular bone (Khan et al., 2013). In contrast to lamellar bone, apatite crystals within trabecular bone do not appear to have a preferred orientation of the *c*-axis (Rubin et al., 2003, Hong et al., 2009). Crystal orientation within trabecular bone appears to change even within single plates, indicating that they are multi-crystalline with low angle grain boundaries, in contrast to lamellar bone (Hong et al., 2009).

Bone has a limited number of responses to disease and so it is difficult to assign a particular lesion to a particular cause (Rothschild and Martin, 2006). All diseases which can produce the observed skeletal changes must be considered, even if they only rarely produce such changes (Rothschild and Martin, 2006). "Porosity," for example, is a term used in paleopathology to denote the presence of macroscopically identifiable discontinuities in bone surfaces including holes, pores, pits, vascular channels and trabecular bone visible due to erosion, is a poorly defined term with a variety of meanings in fields outside of paleopathology (Rothschild 2013). This phenomenon has no identifiable clinical correlation and Rothschild (2013) argues should be discarded (Rothschild, 1997, Rothschild and Martin, 2006, Rothschild 2013). Decreases in bone density can be the result of osteoporosis, vitamin D deficiency, vitamin C deficiency, congenital disorders, endocrine disorders, liver disease or tumors (Rothschild, 1982, Resnick and Niwayama,1988, Rothschild and Martin, 2006). Increases in bone density can include osteopetrosis, myelosclerosis, fluorosis, Paget's disease, bone islands, osteoma (benign bone tumors), heavy metal poisoning, lymphoblastoma and metastatic osteoblastic carcinoma (Rothschild, 1982, Resnick, 2002, Rothschild and Martin, 2006). "Growth arrest" lines form across the marrow cavity when growth surges occur after as little as two weeks of starvation with refeeding (Park, 1964, McHenry, 1968, Rothschild and Martin, 2006). Disruptions to the cortex are referred to as erosion (Rothschild and Martin, 2006). Periosteal reactions (formation of new

bone within the periosteum in response to injury or illness) may be initiated by trauma, hyperemia, hemorrhage, infection [pyogenic (pus generating) bacteria, syphilis, yaws, tuberculosis, fungal diseases and rubella], inflammation of blood vessels, neoplasia, scurvy and venous or arterial insufficiency (Rothschild and Martin, 2006).

1.3 Pathologies examined

1.3.1 Porotic Hyperostosis

Porotic hyperostosis (overgrowth of bone) causes the development of penetrating holes of variable size with the appearance of exposed marrow trabeculae. Porotic hyperostosis often affects a large area of the parietal bones, the occipital squama and occasionally the frontal bone (Stuart-Macadam, 1989, Dominguez-Rodrigo et al., 2012). Cranial bones affected by porotic hyperostosis show thinning or obliteration of the outer table (Dominguez-Rodrigo et al., 2012, Grauer 2012). Enlargement of hematopoietic (blood cell producing) marrow thins the external lamina and exposes the diploë (cancellous tissue of the skull) followed by hypertrophic growth of the trabecular bone. Enlargement of the trabecular bone eventually results in a "hair-on-end" phenomenon (Figure 3) (Resnick, 2002, Rothschild and Martin, 2006, Dominguez-Rodrigo et al., 2012). This presentation is most frequently associated with parasitic infections and hemolytic anemia (Caffey, 1957, Resnick, 2002, Rothschild and Martin, 2006). Certain parasitic infections (e.g., hookworm) produce blood loss, stimulating marrow production of new blood (Stransky and Quintos, 1947). The bone marrow subsequently produces red blood cells that poorly transport oxygen, so the marrow becomes hyperplastic in an effort to produce more oxygen carrying capacity (e.g., more red blood cells, but still poorly functional or potentially destroyed before maturation) (Rivella, 2009). The process is referred to as ineffective erythropoiesis

(Lanzkowsky, 1968, Rivella, 2009). Porotic hyperostosis is a frequently recognized archaeological phenomenon (Angel, 1978, Von Endt and Ortner, 1982, Rothschild and Martin, 2006, Dominguez-Rodrigo et al., 2012). The earliest recognized case of porotic hyperostosis was documented in a 1.5 million year old Hominin skull from Olduavai Gorge, Tanzania (Dominguez-Rodrigo et al., 2012).

The relationship between anemia and porotic hyperostosis is controversial (Rothschild and Martin, 2006, Dominguez-Rodrigo et al., 2012). Iron deficiency can cause hypoplastic marrow (underdevelopment of marrow due to reduced cell number), not hyperostosis, but bone marrow hyperplasia causes porotic hyperostosis and depletes the body's nutrient stores (Rothschild and Martin, 2006). Iron stores are typically the most rapidly depleted, resulting in anemia (Rothschild and Martin, 2006). The rate of skull changes in patients with iron deficiency is very low (<1%), which is not consistent with archaeological evidence for populations with incidences as high as 50% (Eng, 1958, Lanzkowsky, 1968, Rothschild and Martin, 2006). In contrast it has only rarely been observed in modern human foragers (Lallo et al., 1977, Dominguez-Rodrigo et al., 2012). This phenomenon has been associated with hemolytic, rather than iron deficiency anemia, as red blood cells in patients presenting with this phenomenon have significantly shortened half-lives (Lanzkowsky, 1968, Rothschild and Martin, 2006) and with ineffective erythropoiesis or blood loss related to parasitic infections/infestations. Archaeological sites with high incidences of porotic hyperostosis still require further explanation, but may be related to genetic hemolytic anemia, hemoglobinopathies or residual of parasitic infection/infestation (Rothschild and Martin, 2006, Dominguez-Rodrigo et al., 2012). Interpretation of localities with high frequencies (up to 88% of 0-10 year olds) remains unclear (Akins, 1986, Stodder, 1987, Rothschild and Martin, 2006).

1.3.2 Osteomyelitis

Osteomyelitis, resulting from non-specific bone infection, causes a filigree bone reaction and can produce draining abscesses (Rothschild and Martin, 2006, Rothschild, 2013). Non-pyogenic forms include mycobacterial diseases such as tuberculosis, brucellosis and fungal disorders (Rothschild et al., 2006). Acute pyogenic infections most often affect the long bones of children, near metaphyses, with the femur and tibia being the most commonly affected bones (Rothschild et al., 2006). Bone infections have been documented in reptiles including mosasaurs, *Allosaurus* , *Dilophosaurus* and mammals including Paleocene condylarth *Periptychus carinidens*, Miocene rhinoceros, *Metaxytherium jordani* (sea cow) and *Hydrodamalis* (Steller's sea cow) (Libed and Lucas 2000, Rothschild and Martin, 2006). Brucellosis and tuberculosis have also been documented to cause osteomyelitis in mammals (Rothschild and Martin., 2006).

Bones may develop abscess cavities, sometimes termed Brodie's abscesses. They are typically spherical or elliptical with the long axis parallel to the long axis of the bone (Rothschild and Martin, 2006). The margins are typically well defined and occasionally associated with widening of the bone (Rothschild and Martin, 2006). Infection induced inflammation can also interfere with blood flow, resulting in the formation of blood clots and necrosis (Rothschild and Martin, 2006). The necrotic bone can then be isolated by a dense sheath of tissue termed a sequestrum (Rothschild and Martin, 2006). The periosteum responds to inflammation by forming new bone, which also becomes infected, forming a draining outlet (Rothschild and Martin, 2006). Infection typically destroys bone faster than it can be rebuilt, leading to a fibrous appearance with disorganized trabeculae (Rothschild and Martin, 2006).

1.3.3 Uroliths

Urolith is the generic term given to stones formed within the urinary tract, including both kidney and bladder stones (Sellés-Martínez, 1996, Rothschild et al., *in review*). Several varieties of stones are known: Staghorn (resembling a stag's antlers) calculi are recognized as resembling a cast of the renal pelvis; urate stones, which do not contain calcium; rare cysteine stones, which is not calcified; and calcium phosphate, hydroxylapatite and/or oxalate stones, which present as mammillated (mulberry appearance), laminated, faceted (when multiple stones are present, similar to multiple gall stones), or as spiculated calcific stones of uniform internal density (Finco et al., 1970, Clark, 1974, Greene and Scott, 1983, Jones and Hunt, 1983, Rothschild et al., *in review*). Bladder stones may be crystalline or amorphous with variable ammounts of organic compounds between layers (D'Alessio et al., 2005). Such stones have been found in numerous species in the contemporary, historical and archeological record including humans and contemporary mammals (Clark 1974, Jones and Hunt 1983, Calle 1988, Morris and Rodgers 1989, Dyer et al. 1998), including dogs (Finco et al., 1970, Clark 1974, Calle 1988,), the maned wolf (Bush and Bovee 1978), cats (Bohonowych et al., 1978), the hog, *Sus scrofa* (Rothschild et al., *in review*), the Asian small clawed otter *Aonyx cinerea* (Calle 1988), raccoon *Procyon lotor* (Page and Probst 1981), ferrets, weasels, and mink *Mustela vison* (Sompolinsky 1950), harbor seal *Phoca vitulina* (Stroud 1979), and non-domesticated llama *Lama glama* (Kock and Fowler 1982) (Rothschild et al., *in review*).

The oldest previously reported stones were from humans dating to 8500 years before present based on ^{14}C dating [Shattock 1905, Piperno, 1976 (cited in D'Alessio et al., 2005), Shah and Whitfield, 2002, D'Alessio et al., 2005]. These samples were found in a Mesolithic grave site at Uzzo Cave (Trapani, Western Sicily) within the pelvis of a 20-25 year old male

(D'Alessio et al., 2005). No uroliths have been reported older than the Holocene (Rothschild et al., *in review*).

2. Materials and Methods

2.1 Porotic hyperostosis

In order to better understand this phenomenon a section of human skull (KU Natural History Museum (KUNHM), teaching collection) from the Wedda site in Sri Lanka was analyzed using Raman microspectroscopy (Figures 7 and 8). Caldwell (2012) notes that the material surrounding the hole, rather than the hole itself, is of interest, thus the bone around the openings were examined and compared with the more fibrous trabecular bone and smooth areas on the samples surface (Figure 8).

2.1.2 Osteomyelitis

The sample (KUNHM, teaching collection) examined here is an artiodactyl (cloven-hooved) mammal (*Gen. sp. Indet.*) tibia presenting with osteomyelitis with a draining outlet (Figure 9). The sample was sectioned longitudinally in order to perform Raman microspectroscopic analysis of the interior. Spectra were collected from locations within the cortical bone, throughout the trabecular bone, with special emphasis on the region corresponding to the draining tract (Figure 10). Sites 1, 2 and 7 represent cortical bone (Figure 10). Sites 3, 5, 6 and 8-11 represent trabecular bone (Figure 10). Site 4 may be an example of dead cortical bone absorbed into the expanding trabecular bone (Figure 10).

2.1.3 Uroliths

The sample examined here (KUVP 148307) is a possible urolith (Figure 4). The sample is a 3 cm diameter spheroid, found by E. Galbreath in massive grey mudstones of the Early Oligocene Cedar Creek Formation in Northeastern Colorado. The locality contains well preserved skeletal remains of fossil tortoises and fossil mammals including archaic artiodactyls (entelodonts and oreodonts), primitive horses and rhinos (*Mesohippus, Hyracodon* and *Subhyracodon),* and archaic carnivores (creodonts, hesperocyonine canids, nimravids) (Galbreath, 1953, Rothschild et al., *in review*). Carbonate concretions have been noted, typically associated with fossil soil horizons, however phosphatic nodules have not been reported (Rothschild et al., *in review*). The distinctive spherical shape suggested a biological origin, and on the basis of size and shape, it was originally catalogued as a fossil egg (Rothschild et al., *in review*).

The sample was examined macroscopically and compared with urolith and bezoar [stomach stones composed of hair (tricho-) or plant fibers (phyto-)] (Sooy et al. 1997, Yasar et al. 2005) samples curated by the Armed Forces Institute of Pathology (AFIP) (Rothschild et al., in review). It was then molded using silicone rubber and embedded in plaster to keep it from breaking up while being sectioned.

2.2 Raman Microspectroscopy

Raman microspectroscopy has become increasingly important in paleontology due to its nondestructive nature and ability to detect both inorganic and organic molecules *in situ* with a spatial resolution as small as 1 μm. Raman spectroscopy involves impinging monochromatic light in the ultraviolet, visible or near-infrared region and measuring light which has been scattered inelastically (Raman scattered). This effect was predicted by A. Smekel (1923, cited in

De Beer et al., 2011) but first observed by C.V. Raman and K.S. Krishnan (1928). The original experiment used sunlight focused with a telescope on a scattering material (Raman and Krishnan, 1928). A blue-violet filter was applied to incident light and a yellow-green filter was used to limit light reemitted by the scattering materials (Raman and Krishnan, 1928). The change in wavelength from the incident wavelength corresponds to a change in the vibrational state of the molecule and is influenced by the masses of the attached atoms, the nature of the bond and the symmetry of the molecule. Raman shift (Δ cm^{-1}) can provide a fingerprint for identifying both organic and inorganic molecules (e.g. Marshall et al., 2010, Olcott Marshall et al., 2012).

2.2.1 Hydroxlapatite

Hydroxylapatite [$Ca_{10}(PO_4)_6(OH)_2$] (Figure 1) is the most common biological apatite, while fluorapatite is the most common geologic form (Dyar etal., 2008). The majority of apatites [$Ca_5(PO_4)_3(F,Cl,OH)$] are hexagonal (dipyramidal), however end-member chloroapatite and some hydroxylapatites may be monoclinic (Hughes et al., 1990, Dyar et al., 2008). Apatite shows extensive solid solution with both anions and cations, and in fact approximately half of the elements in the periodic table have been found in apatites (Dyar et al., 2008). PO_4^{3-} may be substituted by AsO_4^{3-} but also by CO_3^{2-} + (F^- or OH^-) groups forming carbonated apatites (Deer et al., 1992). SiO_4^{4-} and SO_4^{2-} may also substitute for PO_4^{3-}, but these substitutions must be coupled with cationic substitutions (Klein and Dutrow, 2008).

2.2.2 Raman Microspectroscopy of Apatite

The ν_1 P-O symmetric stretching mode of the PO_4^{3-} tetrahedron occurs at ~962 Δ cm^{-1} and is the dominant Raman active mode of biological hydroxylapatite (Thomas et al., 2011). Two types of CO_3^{2-} substitutions occur. Type A substitutions occur when OH- is substituted by

trigonal planar CO_3^{2-} and type B occur when PO_4^{3-} is substituted by CO_3^{2-} (Penel et al., 1998). CO_3^{2-} substitutions decrease crystallinity (e.g. crystallite size and degree of lattice perfection) and increase the solubility of hydroxylapatite in acidic environments (Pucéat et al., 2004, Khan et al., 2013). The ν_1 P-O symmetric stretching mode of the PO_4^{3-} tetrahedron in hydroxylapatite occurs at ~960 Δ cm^{-1} in type B carbonated apatites (Penel et al., 1998, Stewart et al., 2002, Wopenka and Pasteris, 2005). Type A carbonated apatites exhibit a ν_1 P-O symmetric stretching mode of the PO_4^{3-}tetrahedron at ~957 Δ cm^{-1} with a shoulder at ~947 Δ cm^{-1} (Penel et al., 1998). This variation can be attributed to different environments for the PO_4^{3-} tetrahedra as well as changes in crystallography (Figure 5) (Penel et al., 1998). Weak ν_3 P-O anti-symmetric stretching modes of the PO_4^{3-} tetrahedron in apatite occur at ~1076, ~1061, ~1053, ~1046, ~1040 and ~1029 Δ cm^{-1} (Awonusi et al., 2007). However a band ~1070 Δ cm^{-1} corresponding to a ν_1 C=O symmetric stretching mode of the CO_3^{2-} ion for type B substitutions can envelop these bands (Penel et al., 1998, Awonusi et al., 2007). Weak bands between 568 and 617 Δ cm^{-1} are assigned to ν_4 O-P-O bending modes of the PO_4^{3-} tetrahedron (Khan et al., 2013). In hydroxylapatite, ν_2 O-P-O bending of the PO_4^{3-} tetrahedron has a moderately intense mode at ~430 Δ cm^{-1} and weak modes at ~449 and 452 Δ cm^{-1} (Khan et al., 2013). In a type A carbonated apatite, ν_2 O-P-O bending of the PO_4^{3-} tetrahedron exhibits several weak modes ~440 Δ cm^{-1} (Khan et al., 2013). Weak ν_4 O-P-O bending modes of the PO_4^{3-} tetrahedron in apatite occur between 568 and 617 Δ cm^{-1} (Khan et al., 2013). Weak bands present at 715 and 689 Δ cm^{-1} are assigned to ν_4 C=O=O bending modes of trigonal planar CO_3^{2-} ions in type B carbonated apatite (Awonusi et al., 2007). OH stretching modes occur ~3573 Δ cm^{-1} (Penel et al., 1998). Modes observed ~1003 Δ cm^{-1} in biological hydroxylapatites have been assigned to the ν_1 P-O symmetric stretching mode of HPO_4^{2-} (Penel et al., 1998).

Crystallinity is the size of crystallites and the degree of lattice perfection (Pucéat et al., 2004). Relative crystallinity for apatite can be approximated by calculating Crystallinity $Index_{(Raman)}$ values following the procedure of Pucéat et al. (2004), although this index does not provide information on crystallite size. The full width half maximum (FWHM) (the bandwidth at ½ maximum intensity) of the ν_1 P-O symmetric stretching mode of the PO_4^{3-} tetrahedron is compared to the average FWHM of magmatic apatites such that CI_{Raman} = 4.9/[Full width half maximum (FWHM) of the ν_1 P-O symmetric stretching mode of the PO_4^{3-} tetrahedron]. The value of 4.9 cm^{-1} corresponds to the average FWHM of the ν_1 P-O symmetric stretching mode of the PO_4^{3-} tetrahedron in magmatic apatites collected with 514.5 and 632.8 nm lasers (Pucéat et al., 2004). Little variation was observed between these two wavelengths, and FWHM collected with a 1064 nm laser also have an average FWHM ~4.9 (Thomas et al., 2011), however as measurements were not conducted with a 785 nm laser CI_{Raman} values calculated for magmatic apatites may not be perfectly analogous. CI_{Raman} values close to 1 are considered high for biological apatites, while those below 0.5 are considered low (Pucéat et al., 2004). Values reported by Pucéat et al., (2004) range from 0.25 to 1.44, with higher CI_{Raman} in fossil rather than modern apatites.

A comparative study of human and sheep cortical bone revealed no significant differences in Raman spectra (Rehman et al., 1995), however Pucéat et al. (2004) do detect variations in relative crystallinity between clades, as determined by FWHM measurements of the dominant ν_1 P-O symmetric stretching mode of the PO_4^{3-} tetrahedron in apatite. Well crystallized apatites have a narrow band while those composed of smaller crystallites or with high CO_3^{2-} content have broader bands (Pucéat et al., 2004). Both inter- and intraclade variation in

crystallinity may be larger than crystallinity changes due to diagenesis and so it is not possible to discriminate between unaltered and diagenetically modified samples (Pucéat et al., 2004).

Other PO_4^{3-} containing crystals which may be present in bone samples include hydroxylapatite precursors and calcium pyrophosphate dihydrate. Hydroxylapatite precursors include dicalcium phosphate dihydrate (brushite) ($CaHPO_4 \cdot 2H_2O$), a monoclinic mineral with a dominant ν_1 P-O symmetric stretching mode for the PO_4^{3-} tetrahedron at ~985 Δ cm^{-1}, amorphous calcium phosphate $Ca_9(PO_4)_6 \cdot xH_2O$, with a ν_1 P-O symmetric stretching mode for the PO_4^{3-} tetrahedron at ~952 Δ cm^{-1}, octacalcium phosphate [$Ca_8H_2(PO_4)_6 \cdot 5H_2O$], which consists of alternating apatitic and hydrated layers, with a ν_1 P-O symmetric stretching mode of the PO_4^{3-} tetrahedron, mode at ~957 Δ cm^{-1}, and β-Tricalcium phosphate [$Ca_3(PO_4)_2$], a rhombohedral structure with ν_1 P-O symmetric stretching modes for the PO_4^{3-} tetrahedron at~ 948 and ~970 Δ cm^{-1} (Markovic, 2001, Stewart et al., 2002, Yashima et al., 2003, Khan et al. 2013). Calcium pyrophosphate dehydrate (CPPD) ($Ca_2P_2O_7 \cdot H_2O$) is one of the most common calcium containing crystals associated with bone disorders. CPPD crystals are triclinic and the mineral has a diagnostic ν_1 P-O symmetric stretching mode at ~1049 Δ cm^{-1} (Maugars et al., 1994, Chen et al., 2009).

Possible diagenetic changes in bone include Sr^{2+} and F^- substitutions for Ca^{2+} and OH^- respectively as well as additional CO_3^{2-} substitutions (Thomas et al., 2007, 2011). In life, bones typically have less than 0.1 wt% accessory ions but interactions with groundwater can induce ionic substitutions (Trueman et al., 2003, Wopenka and Pasteris, 2005, Thomas et al., 2007). These substitutions have predictable effects on the ν_1 P-O symmetric stretching mode of the PO_4^{3-} tetrahedron. Increasing Sr^{2+} substitution redshifts (reduces Raman shift) the position of this band (Thomas et al., 2011). Increasing CO_3^{2-} substitution also redshifts the position of this band,

but also increases bandwidth due to increased heterogeneity within the unit cell (Thomas et al., 2007, 2011). F^- substitutions blueshift (increase the Raman shift) the position of this band, due to the increased electronegativity of fluorine relative to the oxygen of the replaced hydroxide ion and the decreased distance between this ion and the oxygen atoms within the PO_4^{3-} tetrahedron (Calderin et al., 2003, Thomas et al., 2011). These changes are summarized in Figure 6.

2.2.3 Raman Spectroscopy Parameters

Raman point-spectra were collected using a Renishaw *inVia* Reflex Raman Microprobe with a Peltier-cooled charge-coupled device detector. The microscope optics for the Raman system are based on a Leica DM-LM microscope. A 785 nm 300 mW air-cooled near-IR diode laser oriented normal to the sample was used to excite the sample. Utilizing a near-IR laser to excite the sample reduces autofluorescence associated with the organic components of bone (Stewart et al., 2002, Khan et al., 2013). Calibration of the Raman shift is achieved by recording the Raman spectrum of the crystalline silicon Si-Si LO lattice mode at 520.5 Δ cm^{-1} for one accumulation and 10 s (Sui et al., 1992). If necessary, an offset correction is performed to ensure that the position of the band is at 520.50±0.10 Δ cm^{-1}. Spectra were collected with the 785 nm laser focused with a 20x refractive glass objective lens for and 1 - 20 accumulations of 10- 30 s. Laser power ranged from 0.5-10% in order to optimize the signal to noise ratio while limiting autofluorescence. Parameters used for each sample can be found in Table 1. Baseline corrections were performed in GRAMS/AI version 8 using a multi-point linear level only function. Deconvolution of bands into component mixed Gausian-Lorentzian bands were performed in GRAMS/AI version 8 using a linear baseline and 50 iterations to minimize the chi-squared value (e.g. Figure 11) (e.g. Awonusi et al., 2007). When spectra were normalized for comparison, spectra were first baseline corrected using a multi-point linear baseline correction function and

then normalized to the most intense peak in WIRE version 3.3 with a lower limit of 0 and an upper limit of 1.

3. Results

3.1 Porotic Hyperostosis

As apatites are anisotropic (possessing crystals which have properties that differ according to the direction of measurement) the orientation of the *c*-axes relative to the polarization of the incident laser may alter the resultant spectra. To test this possibility, spectra were collected with the laser either parallel or perpendicular to the *c*-axis at site 2 and normalized to the most intense band (Figure 12). No significant differences were observed in this sample. Raman spectra from sites 1-5 displayed bands ~985 and ~961 Δ cm^{-1} (Figure 13-17). The band present ~961 Δ cm^{-1} is assigned to the dominant ν_1 P-O symmetric stretching mode of the PO_4^{3-} tetrahedron in apatite (Penel et al., 1998). Band positions observed for this mode ranged from 960.44 to 961.79 Δ cm^{-1} and FWHM ranged from 10.73 cm^{-1} to 14.69 cm^{-1} (table 2, Figure 18). Crystallinity Index (Raman) values ranged from 0.334 to 0.457. The band present at ~986 Δ cm^{-1} is assigned to ν_1 P-O symmetric stretching mode of the PO_4^{3-} tetrahedron in an apatite precursor such as dicalcium phosphate dihydrate ($CaHPO_4 \cdot 2H_2O$) (Stewart et al., 2002). The band at ~1002 Δ cm^{-1} in the Raman spectra obtained from sites 1 and 2 is assigned to the ν_1 P-O symmetric stretching mode of HPO_4^{2-} (Pennel et al., 1998). The band ~1071 Δ cm^{-1} present in spectra obtained from sites 1 and 2 corresponds to both ν_3 P-O anti-symmetric stretching modes (1029, 1034, 1041, 1048, 1057, 1064, 1077 Δ cm^{-1}) and a ν_1 C=O symmetric stretching mode for CO_3^{2-} ions in type B substitutions in apatite (~1070 Δ cm^{-1}) (Awonusi et al., 2007). Comparing the spectra, there is an obvious difference in the relative intensity of the ~985 and ~960 Δ cm^{-1}

bands (band height of the ~960 Δ cm^{-1} band/band height of the ~985 Δ cm^{-1} band) between smooth areas (15.2 and 6.60for sites 1 and 2, respectively) and the boundaries of the pores (0.36 and 0.74 for sites 3 and 4, respectively), with the pore boundaries being most similar to the most cancellous bone (0.35, site 5) (Figures 13-17).

3.2 Osteomyelitis

Raman spectra were obtained from the cortical bone at site 1 with the laser either parallel or perpendicular to the *c*-axis and normalized to the most intense band in order to test for polarization effects (Figure 19). Fluorescence varied significantly between these spectra and so baseline corrections were performed prior to normalizing the spectra to the most intense band. This experiment shows that bands at ~ 960 Δ cm^{-1}, assigned to the ν_1 P-O symmetric stretching mode of the PO_4^{3-} tetrahedron in apatite, and ~1030 and 1046 Δ cm^{-1} assigned to ν_3 P-O anti-symmetric stretching modes, are depolarized (Khan et al., 2013). This is consistent with the findings of Kazanci et al. (2007) that the intensity of the ν_1 P-O symmetric stretching mode of the PO_4^{3-} tetrahedron in apatite in cortical bone is sensitive to orientation.

Raman spectra obtained from the artiodactyl sample (KUNHM, teaching collection) all contained bands at ~985 and ~961 Δ cm^{-1} (Figures 20-30). The band ~961 Δ cm^{-1} is assigned to the dominant ν_1 P-O symmetric stretching mode of the PO_4^{3-} tetrahedron in apatite (Penel et al., 1998). Band position ranged from 960.10 to 962.10 Δ cm^{-1} and FWHM ranged from 13.46 cm^{-1} to 16.06 cm^{-1} (table 3, Figure 31). Crystallinity Index (Raman) values ranged from 0.305 to 0.364.

The band present at ~986 Δ cm^{-1} is assigned to the dominant ν_1 P-O symmetric stretching mode of the PO_4^{3-} tetrahedron in an apatite precursor such as dicalcium phosphate dihydrate ($CaHPO_4 \cdot 2H_2O$) (Stewart et al., 2002). The bands present at ~1003 Δ cm^{-1} in spectra

obtained from sites 1, 2, 4, 5, 7, 9, 10 and 11 are assigned to the ν_1 P-O symmetric stretching mode of HPO_4^{2-} (Penel et al., 1998). The broad bands present at ~1071 Δ cm^{-1} in spectra obtained from sites 1, 2, 4, 5, 7, 9,10 and 11 correspond to both ν_3 P-O anti-symmetric stretching modes (1029, 1034, 1041, 1048, 1057, 1064, 1077 Δ cm^{-1}) and the ν_1 C=O symmetric stretching mode for CO_3^{2-} in type B substitutions in apatite (~1070 Δ cm^{-1}) (Penel et al., 1998, Awonusi et al., 2007). A shoulder ~947 Δ $cm^{-1}$was present in spectra from sites 1, 2 (cortical bone) 7, 10, 11 (healthy trabecular), and site 9 (diseased trabecular) but not in 3, 5, 6 or 8(diseased trabecular) or 4 (relict cortical). These may be assigned to either the ν_1 P-O symmetric stretching mode for the PO_4^{3-} tetrahedron in tricalcium phosphate or type A carbonated apatites. Shoulders present ~970 Δ cm^{-1} would appear to favor the former (whereas type A carbonated apatites exhibit a band at ~957 Δ cm^{-1}), however it is not possible to resolve mixed Gausian-Lorentzian bands present at these band positions. Examining the 2nd derivative indicates that peaks may be present ~975 Δ cm^{-1} for site 1 and ~973 Δ cm^{-1} for site 2, while there are no indications of a peak present ~970 Δ cm^{-1} in 2nd derivative plots of spectra obtained from sites 7,9, 10,11 (Appendix V).

3.3 Urolith

The sample (KUVP 148307) is composed of five 0.5-0.8 mm layers (Figure 4). The layers tend to separate and fall off (Figure 4A). This was similar to observations on animal (both human and non-human) bladder stones (Figure 4C) in the collections of the Armed Forces Institute of Pathology (AFIP) (Rothschild et al., *in review*). This feature results in part from the decay of organic material that had once bonded the layers of the urolith and is diagnostic for uroliths when compared to inorganic concretions (Rothschild et al., *in review*). Non-biologically derived concretions may also show concentric layers but usually with abrupt changes in mineralogy and crystal size (Mozley 1996). The external surface lacks evidence of linear

structures (e.g., hair, plant fibers typical of bezoars), but is covered by small "bumps," giving it a "mammary" appearance (Rothschild et al., *in review*). A cross-sectional view of the fossil reveals the layers to be composed of crystals oriented perpendicular to the surface of the mass (Figure 4B), an arrangement characteristic of uroliths (Rothschild et al., *in review*). When sectioned, the fossil stone showed a hollow center (1.5 cm diameter) with a small, phosphatic pillar extending into the cavity (Figure 2B). It is unlikely that the pillar resulted from dissolution/re-precipitation or as an artifact of the sectioning process, as it extended focally on a narrow base from the inner wall of the urolith. This is consistent with bladder stones, some of which have fluid filled centers (Khoury et al., 2005). A similar cavity with a pillar (Figure 4D) was noted in a bladder stone from a hog, *Sus scrofa* (AFIP 6072) (Rothschild et al., *in review*).

Organic material was detected via Raman microspectroscopy, both within the central phosphatic pillar (Figure 32) and in multiple locations in the outer layers (Figures 33, 34). Bands present between 1100 and 1600 Δ cm^{-1} are assigned to C-C, and C=C stretching modes of Hlic aromatic hydrocarbons (PAHs) (Mapelli et al., 1999, Olcott Marshall et al., 2012). The band at ~962 Δ cm^{-1} is assigned to the ν_1 P-O symmetric stretching mode of the PO_4^{3-} tetrahedron in apatite, (Edwards et al., 1995, Penel et al., 1998, Thomas et al., 2011). The band present at ~985 Δ cm^{-1} is assigned to the ν_1 P-O symmetric stretching mode of the PO_4^{3-} tetrahedron in an apatite precursor such as dicalcium phosphate dihydrate (Stewart et al., 2002). The sediments surrounding the fossil were carbonate-rich mudstones that have not produced phosphatic concretions of inorganic origin (Rothschild et al., *in review*).

4. **Discussion**

4.1 Porotic Hyperostosis

Spectra collected from the smooth areas (sites 1 and 2) and "pore" boundaries (sites 3 and 4) showed distinct differences in chemistry, with the relative intensity of the apatite (Figures 13-17, table 4). It is intriguing that the boundaries of the "pores" have spectra similar to the thread-like projections while smooth areas differ in composition. It is possible that these differences may be due to interaction with groundwater as the boundaries to the pores and the trabeculae have higher surface area to volume ratios. Fluoride substitution, for example, could blueshift the ν_1 P-O symmetric stretching mode of the PO_4^{3-} tetrahedron in apatite (Thomas et al., 2011). Nevertheless, band positions were still within the parameters found for modern bone and not necessarily indicative of diagenetic alteration (Pucéat et al., 2004, Thomas et al., 2011).

Alternatively, the smooth areas may represent patches of less altered or relict cortical bone. The reduced intensity of the v_1 P-O symmetric stretching mode of the PO_4^{3-}tetrahedron within apatite with respect to the mode assigned to the v_1 P-O symmetric stretching mode of the PO_4^{3-} tetrahedron in apatite precursors in the cancellous bone sites may be related to a reduced ability of osteoblasts to mineralize the rapidly expanding trabecular bone normally, especially in a nutrient poor environment. Investigating modern medical samples which have not been exposed to groundwater utilizing Raman microspectroscopy could resolve whether the changes observed within this sample are diagenetic or related to the pathology itself.

4.2 Osteomyelitis

The apatite in trabecular bone presenting with osteomyelitis does not appear to vary significantly in composition when compared with healthy trabecular bone or cortical bone. Crystallinity Index values ranged from 0.312 to 0.324 for cortical bone, from 0.291 to 0.364 for healthy trabecular bone and from 0.305 to 0.346 for diseased trabecular bone. As the variation in

CI_{Raman} among sites in healthy bone encompasses observed CI_{Raman} values from diseased bone CI_{Raman} does not appear to be influenced by this pathology. The band ~1070 Δ cm^{-1} assigned to the combination of a ν_1 C=O symmetric stretching mode of the CO_3^{2-} ion in type B carbonated apatites and ν_3 P-O anti-symmetric stretching modes of the PO_4^{3-} tetrahedron in apatite was present in all cortical bone spectra as well as spectra from healthy trabecular bone (sites 10 and 11) and diseased trabecular bone at sites 5 and 9, but absent from sites 3, 6, 8 (diseased trabecular bone) (Awonusi et al., 2007). Increased CO_3^{2-}content may also increase the FWHM and redshift the P-O ν_1 band in apatite, which may account for these differences.

Spectra obtained from Site 6 (the trabecular bone directly around the drain) had a distinctly different appearance (Figure 25) which may be related to differing chemical conditions at the abscess. This change is reminiscent of the change observed in the porotic hyperostosis "pores," however a decrease in the intensity of the ~961 Δ cm^{-1} ν_1 P-O symmetric stretching mode of the PO_4^{3-} tetrahedron in apatite relative to the ~985 Δ cm^{-1} ν_1 P-O symmetric stretching mode of the PO_4^{3-} tetrahedron in apatite precursors observed in these spectra also occurs in the polarization experiments conducted on this sample. Overall, variations in band positions and FWHM/crystallinity between healthy and diseased localities do not exceed variations within these groups (Figure 31).

When these data from both the porotic hyperostosis (PH) sample and the osteomyelitis (OM) sample are compared the smooth locations from the PH sample lie closer to the ranges ascribed to cortical bone and healthy trabecular bone (Figure 35). OM site 6 does appear to have more similarity to the PH pore boundaries and thread-like trabecular bone than to trabecular bone within the OM sample, however it is unclear whether this is associated with biological changes or if the location of site 6 near the abscess allowed the material to be altered in a similar fashion.

Crystallinity Index values calculated for these samples were also compared with values derived from Pucéat et al., (2004) for reptile, modern and fossil fish (Figure 36). CI_{Raman} values for the samples examined here fell within the range observed by Pucéat et al., (2004), but tended to be lower. The difference in observed means was not greater than that observed by Pucéat et al., (2004) between clades and so it is unclear if this increased disorder can be ascribed to biological differences (either evolutionary or pathologically derived) or to alteration. A third possibility remains that the difference in excitation wavelength is responsible for these differences as Pucéat et al., (2004) utilized 514.5 and 632.8 nm lasers to collect their spectra.

4.3 Urolith

The sample most closely resembles uroliths both in structure and composition when compared with abiotic sedimentary structures and bezoars (Rothschild et al., *in review*). Detection of organic compounds (PAHs) within the sample supports a biological origin for the stone (Rothschild et al., *in review*). Other diagnostic considerations included bezoars, gall stones and non-spherical, non-uniformly calcified masses (Appendix VI), which are easily distinguishable from the sample (Rothschild et al., *in review*). No trace of fibers was found in the specimen, exluding bezoars from consideration (Rothschild et al., *in review*). Gallstones may be single or multiple, the latter revealing facets at points of contact with other stones (Schwaier et al., 1979, Zhou et al., 1997, Rothschild et al., *in review*). Single gallstones are solid, composed of plate-like cholesterol crystals or organic components that do not crystallize (Rothschild et al., *in review*).

D'Alessio et al. (2005) have also noted that the determination of chemical composition of bladder stones can provide insights about dietary changes, metabolic disorders and climate as

their composition partly depends on these factors. Bladder stones are more common in communities with diets high in grain or rice and low in animal proteins, or with vitamin A or B6 deficiencies (D'Alessio et al., 2005). Alkaline urine pH results in the formation of struvite (magnesium ammonium phosphate), calcium phosphate, ammonium urate or calcite stones, wheras an acidic urine pH leads to stones composed of calcium oxylate and amorphous urates (D'Alessio et al., 2005). High animal protein intake, protracted fasting and intense exercise produce more acidic urine, while grains, rice, fruit and urinary concentration due to hot climates produce alkaline urine (D'Alessio et al., 2005). Raman bands associated with apatite and brushite suggest that this stone formed in an alkaline environment.

5. Conclusion and Future Work

Bladder stones are relatively common in ancient populations (Steinbock, 1989, D'Alessio et al., 2005) and so a nondestructive means of rapidly assessing their chemical composition and structure such as Raman microspectroscopy may prove useful for studying diets in ancient populations. The current example appears to be the oldest recognized urolith. Fossil uroliths may not be uncommon as they can be easily confused with ordinary sedimentary concretions (Rothschild et al., in review). In particular, articulated skeletal material should be searched for possible uroliths directly associated with their animal of origin. Such associated stones have the potential of being an important archive for internal physiology—an aspect of fossil organisms that has proven difficult to access.

Unfortunately the limited responses of bone to disease at the macroscale appear to be reflected in bone mineralization as well. Osteomyelitis does not appear to induce significant changes in bone mineralization. Porotic hyperostosis may induce changes in the chemical

composition of bone, however without unaffected bone tissue from the afflicted individual the extent of these changes is difficult to determine. Differential alteration of the pore boundaries and thread-like trabeculae also cannot be excluded as a possibility.

As the greatest influence on CI_{Raman} appears to be the biologic origin of the apatite (Pucéat et al., 2004), in future studies additional skeletal material should be collected from the individual organisms afflicted by these conditions. Observing the nature of apatite mineralization in porotic hyperostosis in modern samples which have not undergone diagenetic alteration may provide further insight into the nature of this disease, however the exceptionally rare nature of this disease in the modern world makes this prospect unlikely.

References

Akins, N., 1986. A biocultural approach to human burials from Chaco Canyon, New Mexico. Reports of the Chaco Center, National Park Service, Santa Fe, New Mexico.

Angel, J., 1978. Porotic hyperostosis in the eastern Mediterranean. Medical College of Virginia Quarterly 14, 10-16.

Awonusi, A., Morris, M.D., Tecklenburg, M.M.J., 2007. Carbonate assignment and calibration in the Raman spectrum of apatite. Calcified Tissue International 81, 46-52.

Barrett, P.M., Upchurch, P., 2001. Feeding mechanisms and changes in sauropod paleoecology through time. Journal of Vertebrate Paleontology 21, 32A.

Bohonowych, R.O., Parks, J.L., Greene, R.W., 1978. Features of cystic calculi in cats in a hospital population. Journal of the American Veterinary Medical Association 173, 301-303.

Boskey, A.L., 2007. Mineralization of Bones and Teeth. Elements 3, 385-391.

Bush, M., Bovee, K.C., 1978. Cystinuria in a maned wolf. Journal of the American Veterinary

Medical Association 173, 1159-1162.

Caffey, J., 1957. Cooley's anemia: A review of the roentgenographic findings in the skeleton. American Journal of Roentgenology 78, 381-391.

Calderin, L., Stott, M.J., Rubio, A., 2003. Electronic and crystallographic structure of apatites. Physical Review B 67, 13406-13412.

Calle, P.P., 1988. Asian small-clawed otter (*Aconyx cinerea*) urolithiasis prevalence in North America. Zoo Biology 7, 233-242.

Clark, W., 1974. The distribution of canine urinary calculi and their recurrence following treatment. Journal of Small Animal Practice 15, 437-444.

Chen, K.-H., Li, M.-J., Cheng, W.-T., Balic-Zunic, T., Lin, S.-Y., 2009. Identification of monoclinic calcium pyrophosphate dihydrate and hydroxyapatite in human sclera using Raman microspectroscopy. Journal of Experimental Pathology 90, 74-78.

D'Alessio, A., Bramanti, E., Piperno, M., Naccarato, G., Vergamini, P., Fornaciari, G., 2005. An 8500-year-old bladder stone from Uzzo Cave (Trapani): Fourier transform-infrared spectroscopy analysis. Archaeometry 47, 127-136.

De Beer, T., Burggraeve, A., Fonteyne, M., Saerens, L., Remon, J.P., Vervaet, C., 2011. Near infrared and Raman spectroscopy for the in-process monitoring of pharmaceutical production processes. International Journal of Pharmaceutics 417, 32-47.

Deer, W., Howie, R., Zussman, J., 1992. An introduction to the rock-forming minerals, 2nd ed. Pearson Education, Ltd, New York.

Dyar, M.D., Gunter, M., Tasa, D., 2008. Mineralogy and optical mineralogy. Mineralogical Society of America, Chantilly.

Dyer, R.B., Chen, M.Y., Zagoria, R.J., 1998. Abnormal calcifications in the urinary tract.

RadioGraphics 6, 1405-1424.

Edwards, H.G.M., Williams, A.C., Farwell, D.W., 1995. Palaeodental Studies Using FT-Raman Spectroscopy. Biospectroscopy 1, 29-36.

Eng, L., 1958. Chronic iron deficiency anaemia with bone changes resembling Cooley's anemia. Acta Hematologica 19, 263-268.Ewald, P., 1988. Cultural vectors, virulence and the emergence of evolutionary epidemiology. Oxford Surveys in Evolutionary Biology 5, 215-245.

Finco, D.R., Rosin, E., Johnson, K.H., 1970. Canine urolithiasis: a review of 133 clinical and 23 necropsy cases. Journal of the American Vetrinary Medicine Association 157, 1225-1228.

Galbreath, E.C., 1953. A contribution to the Tertiary geology and paleontology of northeastern Colorado. The University of Kansas Paleontological Contributions: Vertebrata 4, 1-120.

Glimcher, M.J., 2006. Bone: Nature of the calcium phosphate crystals and cellular structural, and physical chemical mechanisms in their formation, in: Sahai, N., Schoonen, M.A.A. (Eds.), Medical Mineralogy and Geochemistry. Reviews in Mineralogy and Geochemistry, pp. 223-282.

Greene, R.W., Scott, R.C., 1983. Diseases of the bladder and urethra, in: Etinger, S.J. (Ed.), Textbook of Veterinary Internal Medicine, 2nd ed. WB Saunders, Philadelphia.

Hodge, A.J., 1989. Molecular models illustrating the possible distributions of 'holes' in simple systematically staggered arrays of type I collagen molecules in native-type fibrils. Connective Tissue Research 21, 137-147.

Hong, S.I., Hong, S.K., Kohn, D.H., 2009. Nanostructural analysis of trabecular bone. Journal of materials science. Materials in medicine 20, 1419-1426.

Hughes, J., Cameron, M., Crowley, K., 1990. Crystal structures of natural ternary apatites: Solid solution in the Ca.(POJTX(X : F, OH, Cl) system. American Mineralogist 75, 295-304.

Jones, C.J., Hunt, R.D., 1983. Veterinary Pathology, 5th ed. Lea & Febiger, Philadelphia.

Kazanci, M., Wagner, H., Manjubala, N., Gupta, H., Paschalis, E., Roschger, P., Fratzl, P., 2007. Raman imaging of two orthogonal planes within cortical bone. Bone 41, 456-461.

Khan, A., Awais, M., Khan, A., Tabassum, S., Chaudhry, A., Rehman, I., 2013. Raman spectroscopy of natural bone and synthetic apatites. Applied Spectroscopy Reviews 48, 329-355.

Khoury, A.E., Salomon, M., Doche, R., Soboh, F., Ackerley, C., Jayanthi, R., McLorie, G., Mittelman, M., 2005. Stone formation after augmentation cystoplasty: The role of intestinal mucus. Journal of Urology 158, 1133-1137.

Klein, C., Dutrow, B., 2008. The Manual of Mineral Science, 23 ed. John Wiley & Sons, Hoboken.

Kock, M.D., Fowler, M.E., 1982. Urolithiasis in a three-month-old llama. Journal of the American Veterinary Medical Association 181, 1411.

Krauss, D.A., 2001. An analysis of the feeding habits of herbivorous dinosaurs through the examination of phytoliths trapped on tooth grinding surfaces. Journal of Vertebrate Paleontology 21, 69A.

Lanzkowsky, P., 1968. Radiologic features of iron deficiency anemia. American Journal of Diseases of Children 116, 16-29.

Libed, S., Lucas, S., 2000. Paleopathology of a Paleocene periptychid (Mammalia; Condylarthra) jaw from the San Juan Basin, New Mexico. New Mexico Museum of Natural History and Science Bulletin 16, 151-153.

Mapelli, C., Castiglioni, C., Meroni, E., Zerbi, G., 1999. Graphite and graphite compounds: Vibrational spectra from oligomers to real materials. Journal of Molecular Structure 480-481, 615-620.

Markovic, M., 2001. Octacalcium Phosphate Carboxylates, in: Chow, L., Eanes, E. (Eds.), Octacalcium Phosphate. Monographs in Oral Science. Karger, Basel, pp. 77-93.

Martin, R.B., Burr, D.B., Sharkey, N.A., 1998. Skeletal tissue mechanics. Springer, New York.

Maugars, Y.M., Peru, L.F., el Messaoudi, B., Michaud, G.O., Berthelot, J.M., Prost, A.M., Daculsi, G., 1994. Pelvic pseudotumoral calcium pyrophosphate dihydrate deposition: an ultrastructural study. The Journal of rheumatology 21, 573-576.

"Bone." *Merriam-Webster.com.*. 2013. http://www.merriam-webster.com/dictionary/bone (3 April 2013).

Morris, A.G., Rodgers, A.L., 1989. A probable case of prehistoric kidney stone disease from the northern Cape Province, Africa. American Journal of Physical Anthropology 79, 521-527.

Mozley, P.S., 1996. The internal structure of carbonate concretions in mudrocks: A critical evaluation of the conventional concentric model of concretion growth. Sedimentary Geology 103, 85-91.

Nakano, T., Kaibara, K., Tabata, Y., Nagata, N., Enomoto, S., Marukawa, E., Umakoshi, Y., 2002. Unique alignment and texture of biological apatite crystallites in typical calcified tissues analyzed by microbeam X-ray diffractometer system. Bone 31, 479-487.

Olcott Marshall A, Wehrbein RL, Lieberman BS, Marshall CP (2012) Raman spectroscopic investigations of Burgess Shale-type preservation: A new way forward. Palaios 27:288-292.

Page, C.D., Probst, C.W., 1981. Ammonium urate renal calculus in a raccoon. Journal of the American Veterinary Medical Association 179, 1259-1261.

Penel, G., Leroy, G., Rey, C., Bres, E., 1998. MicroRaman Spectral Study of the PO_4 and CO_3 Vibrational Modes in Synthetic and Biological Apatites. Calcified Tissue International 63, 475-481.

Piperno, M., 1976. Scoperta di una sepoltura doppia epigravettiana nella Grotta dell'Uzzo (Trapani). Kokalos, XXII–XXIII 720, 798-816.

Rehman, I., Smith, R., Hench, L., Bonfield, W., 1995. Structural evaluation of human and sheep bone and comparison with synthetic hydroxyapatite by FT-Raman spectroscopy. Biomedical Materials Research 29, 1287-1294.

Resnick, D., 2002. Diagnosis of bone and joint disorders. Saunders, Philadelphia.

Resnick, D., Niwayama, G., 1989. Diagnosis of Bone and Joint Disorders, 2nd ed. Saunders, Philadelphia.

Rivella, S., 2009. Ineffective erythropoiesis and thalassemias. Current Opinion in Hematology 16, 187-194.

Roberts, E., Rogers, R., 1997. Insect modification of dinosaur bones from the Upper Cretaceous of Madagascar. Journal of Vertebrate Paleontology 17, 71A.

Rothschild, B.M., 1982. Rheumatology: A primary care approach. Yorke Medical Press, New York.

Rothschild, B.M., 1987. Decompression syndrome in fossil marine turtles. Annals of the

Carnegie Museum 56, 253-358.

Rothschild, B.M., 1997. Porosity: A curiosity without diagnostic significance. American Journal of Physical Anthropology 104, 529-533.

Rothschild, B.M., 2013. Nondestructive, Epi-Illumination Surface Microscopic Characterization of Surface Discontinuity in Bone: A New Approach Offers a Descriptive Vocabulary and New Insights. The Anatomical Record 296, 580-589.

Rothschild, B.M., 2011. Pathology in saber tooth ecomorphs, in: Naples, V., Martin, L.D., Babiarz, J. (Eds.), Saber-toothed cats. John Hopkins Press, Baltiomore, pp. 35-41.

Rothschild, B.M., Martin, L.D., 2006. Skeletal Impact of Disease. Bulletin of the New Mexico Museum of Natural History and Science 33, 1-226.

Rothschild, B.M., Martin, L.D., Anderson, B., Olcott Marshall, A., Marshall, C.P., *in review*. Raman spectrographic documentation of Oligocene bladder stone.

Rothschild, B.M., Rothschild, C., 1999. Evolution of osseous/radiologic signs of tuberculosis, in: Palfi, G., Dutour, J., Hutas, D. (Eds.), Tuberculosis past and present. Golden Book Publisher, Ltd, Tuberculosis Foundation, Budapest, pp. 293-298.

Rothschild, B.M., Storrs, G.W., 2003. Decompression syndrome in plesiosaurs (Sauropterygia: Reptilia). Journal of Vertebrate Paleontology 23, 324-328.

Rothschild, B.M., Tanke, D., Carpenter, K., 1997. Tyrannosaurs suffered from gout. Nature 387, 357.

Rothschild, B.M., Tanke, D.H., Helbling, M., Martin, L.D., 2003. Epidemiologic study of tumors in dinosaurs. Naturwissenschaften 90, 495-500.

Rothschild, B.M., Woods, R., 1990. Symmetrical erosive disease in Archaic Indians: The origin of rheumatoid arthritis in the New World? Seminars in Arthritis and Rheumatism 19, 278-284.

Rothschild, B.M., Xiaoting, Z., Martin, L.D., 2012. Adaptations for marine habitat and the effect of Triassic and Jurssic predator pressure on development of decompression syndrome in ichthyosaurs. Naturwissenschaften 99, 443-448.

Rubin, M.A., Jasiuk, I., Taylor, J., Rubin, J., Ganey, T., Apkarian, R.P., 2003. TEM analysis of the nanostructure of normal and osteoporotic human trabecular bone. Bone 33, 270-282.

Rubin, R., Strayer, D., 2011. Rubin's Pathology, 6th ed. Lippincott Williams and Wilkins, New York.

Schlumberger, H.G., 1959. Synovial gout in the parakeet. Labratory Investigation 8, 1304-1318.

Schwaier, A., Weiss, H.J., van der Linden, J., 1979. Tupaias (tree shrews) - A new animal model for gallstone research. II. Influence of fat, sugar and cholesterol in bile composition. Research in Experimental Medicine 176, 157-172.

Sellés-Martínez, 1996. Concretion morphology, classification and genesis. Earth-Science Reviews 41, 177-210.

Shah, J., Whitfield, H.N., 2002. Urolithiasis through the ages. British Journal of Urology International 89, 801-810.

Shattock, J.G., 1905. A prehistoric or predynastic Egyptian calculus. Transactions of the Pathology Society of London 6, 275.

Sompolinsky, D., 1950. Urolithiasis in mink. Cornell Veterinarian 40, 367-376.

Sooy, T.E., Adams, W.M., Pitts, R.P., Beck, K.A., 1987. Balloon catheter dilation of alimentary tract strictures in the dog and cat. Veterinary Radiology and Ultrasound 28, 131-133.

Steinbock, R.T., 1989. Studies in ancient calcified soft tissues and organic concretions, II: urolithiasis (renal and urinary bladder stone disease). Journal of Paleopathology 3, 39.

Stewart, S., Shea, D.A., Tarnowski, C.P., Morris, M.D., Wang, D., Franceschi, R., Lin, D.-L., Keller, E., 2002. Trends in early mineralization of murine calvarial osteoblastic cultures: a Raman microscopic study. Journal of Raman Spectroscopy 33, 536-543.

Stodder, A., 1987. The physical antrhopology and mortuary practice of the Dolores Anasazi: An early Pueblo population in local and regional perspectives, in: Petersen, K., Orcutt, J. (Eds.), Dolores Archaeological Program Supporting Studies: Settlement and Environment. US Bureau of Reclammation Engineering and Research Center, Denver, pp. 309-504.

Straight, W.H., Davis, G.L., Skinner, C.W., Haims, A., McClennan, B.L., Tanke, D.H., 2009. Bone lesions in hadrosaurs: Computed tomographic imaging as a guide for paleohistologic and stable-isotopic analysis. Journal of Vertebrate Paleontology 29, 315-325.

Stroud, R.K., 1979. Nephrolithiasis in a harbor seal. Journal of the American Veterinary Medical Association 175, 924-925.

Sui, Z., Leong, P., Herman, I., 1992. Raman analysis of light-emitting porous silicon. Applied Physics Letters 60, 2086-2088.

Swinton, W., 1981. Sir Marc Armand Ruffer: One of the first palaeopathologists. Canadian medical Association Journal 124, 1388-1392.

Tanke, D.H., Rothschild, B.M., 2002. Dinosores: An annotated bibliography of dinosaur paleopathology and related topics. New Mexico Museum of Natural History and Science Bulletin 20, 1838-2001.

Thomas, D.B., Fordyce, R.E., Frew, R.D., Gordon, K.C., 2007. A rapid, non-destructive method of detecting diagenetic alteration in fossil bone using Raman spectroscopy. Journal of Raman Spectroscopy 38, 1533-1537.

Thomas, D.B., McGoverin, C.M., Fordyce, R.E., Frew, R.D., Gordon, K.C., 2011. Raman spectroscopy of fossil bioapatite - A proxy for diagenetic alteration of the oxygen isotope composition. Palaeogeography, Palaeoclimatology, Palaeoecology 310, 62-70.

Trueman, C., Chenery, C., Eberth, D.A., Spiro, B., 2003. Diagenetic effects on the oxygen isotope composition of bones of dinosaurs and other vertebrates recovered from terrestrial and marine sediments Journal of the Geological Society, London 160, 895-901.

Vann, R.D., Butler, F.K., Mitchell, S.J., Moon, R.E., 2011. Decompression illness. Lancet 377, 153-164.

von Endt, D., Ortner, D., 1982. Amino acid analysis of bone from a possible case of prehistoric iron deficiency from the American Southwest. American Journal of Physical Anthropology 59, 377-385.Waldron, T., 1995. Dr. R.W.Schufeldt. International Journal of Osteoarchaeology 5, 200.

Wopenka, B., Pasteris, J.D., 2005. A mineralogical perspective on the apatite in bone. Materials Science Engineering C 25, 131-143.

Yasar, M., Aslaner, A., Zengin, A., Ertas, E., 2005. Kehr sign with gastric bezoar: A rare case report. Internet Journal of Surgery 6, 2-6.

Yashima, M., Sakai, A., Kamiyama, T., Hoshikawa, A., 2003. Crystal structure analysis of Beta-tricalcium phosphate Ca3(PO4)2 by neutron powder diffraction. Journal of Solid State Chemistry 175, 272-277.

Zhou, X.S., Wu, J.G., Li, W.H., Xu, Y.Z., Weng, S.F., Soloway, R.D., Fu, X.B., Tian, W., Xu, Z., Shen, T., Xu, G.X., Wentrup-Byrne, E., 1997. A spectroscopic study of pigment gallstones in China. Biospectroscopy 3, 371-380.

Figures and Tables

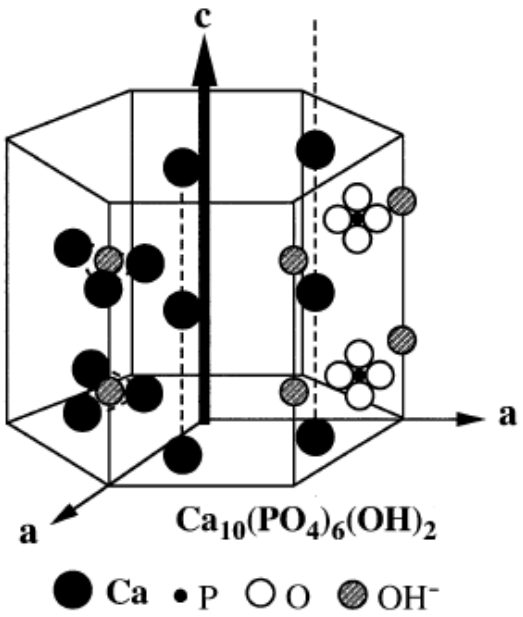

Figure 1: Crystal structure of Hydroxylapatite. Modified from Nakano et al., 2002.

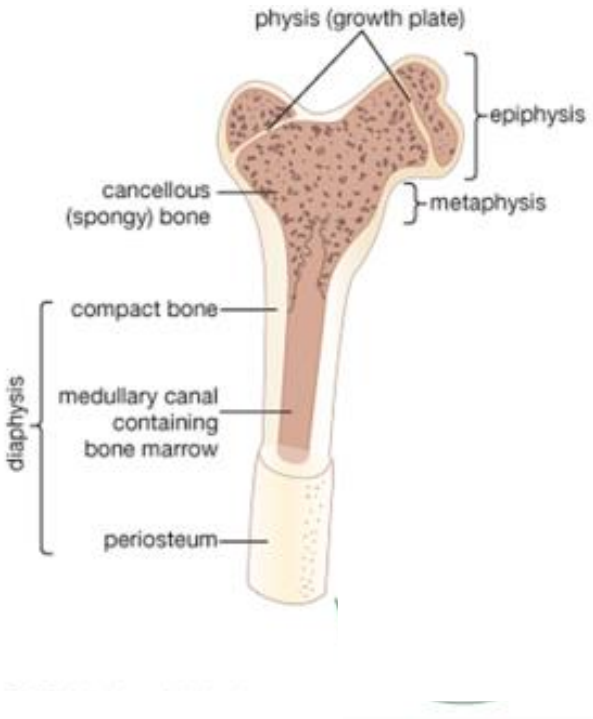

Figure 2: General diagram of long bone structure. Modified from Merriam-Webster (2013).

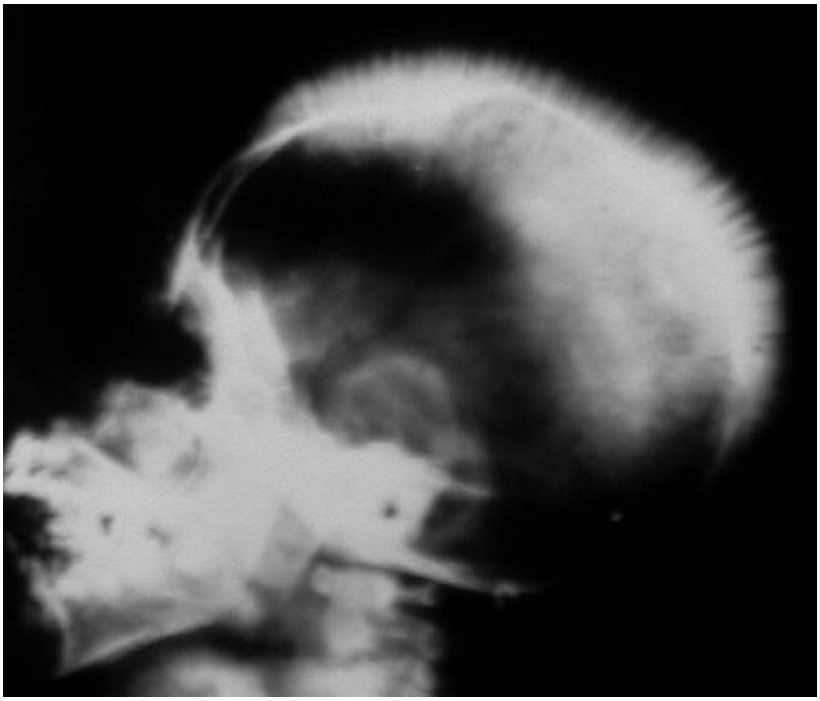

Figure 3: Porotic hyperostosis can produce a “hair on end” phenomenon, related to hemolytic anemias and sickle cell anemia, observed in a lateral X-ray of the skull. Modified from Rothschild and Martin, 2006.

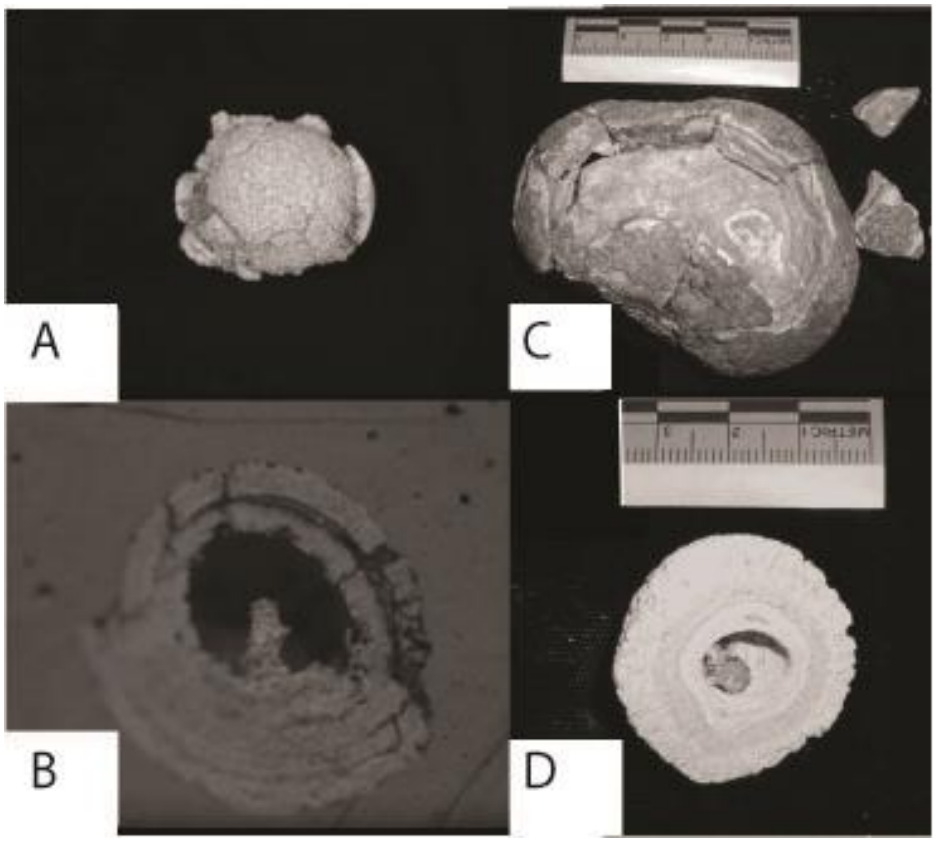

Figure 4: Oligocene bladder stone (KUVP 148307) (A,B), contrasted with (C) human (AFIP 5824) and (D) hog (AFIP 6072) bladder stones. External view (A,C). Cross section (B,D). Modified from Rothschild et al., *in review*.

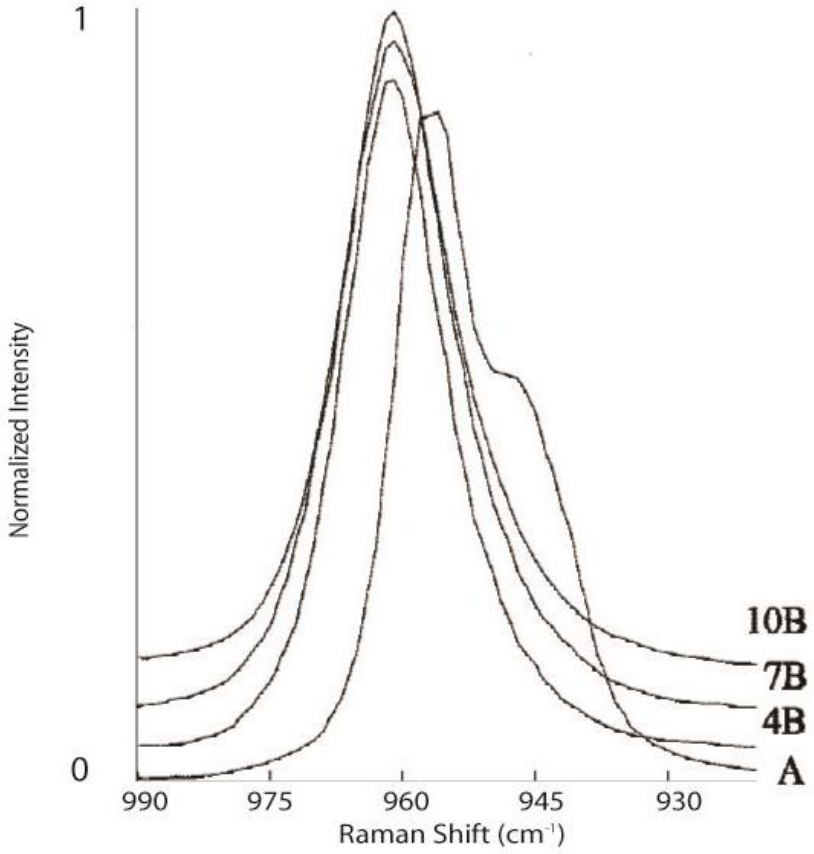

Figure 5: Changes in the ν_1 P-O symmetric stretching mode of thePO_4^{3-} tetrahedron in synthetic carbonated apatites. A. 5.8 wt% type A carbonated apatite 4B. 4.5 wt% type B carbonated apatite 7B. 7 wt% type B carbonated apatite. 10B 10 wt% type B carbonated apatite. Spectra collected with a 632 nm laser at 3 mW focused with a 100 x objective. Modified from Penel et al., 1998.

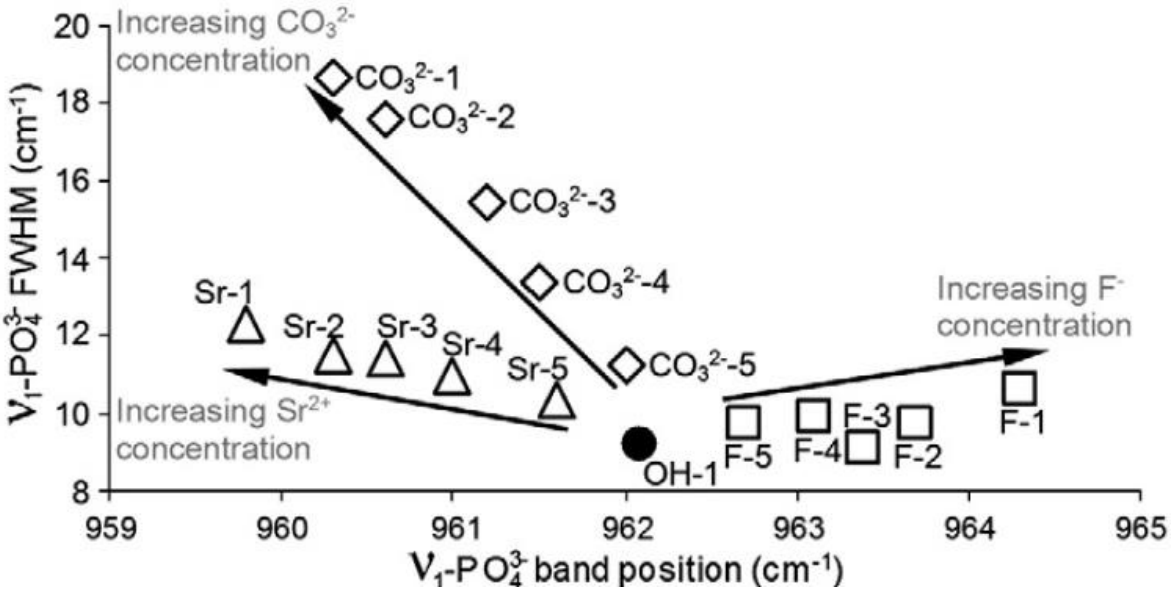

Figure 6: Effect of substitution on the ν_1-phosphate band position of synthetic apatites. Spectra were collected with a 1064 nm laser at 120 mW for 60 minutes. FWHM = Full width at half maximum intensity. Modified from from Thomas et al., 2011.

Figure 7: Dorsal view of porotic hyperostosis in a human skull from the Wedda site in Sri Lanka (KUNHM, teaching collection) (Modified from Rothschild, 2013).

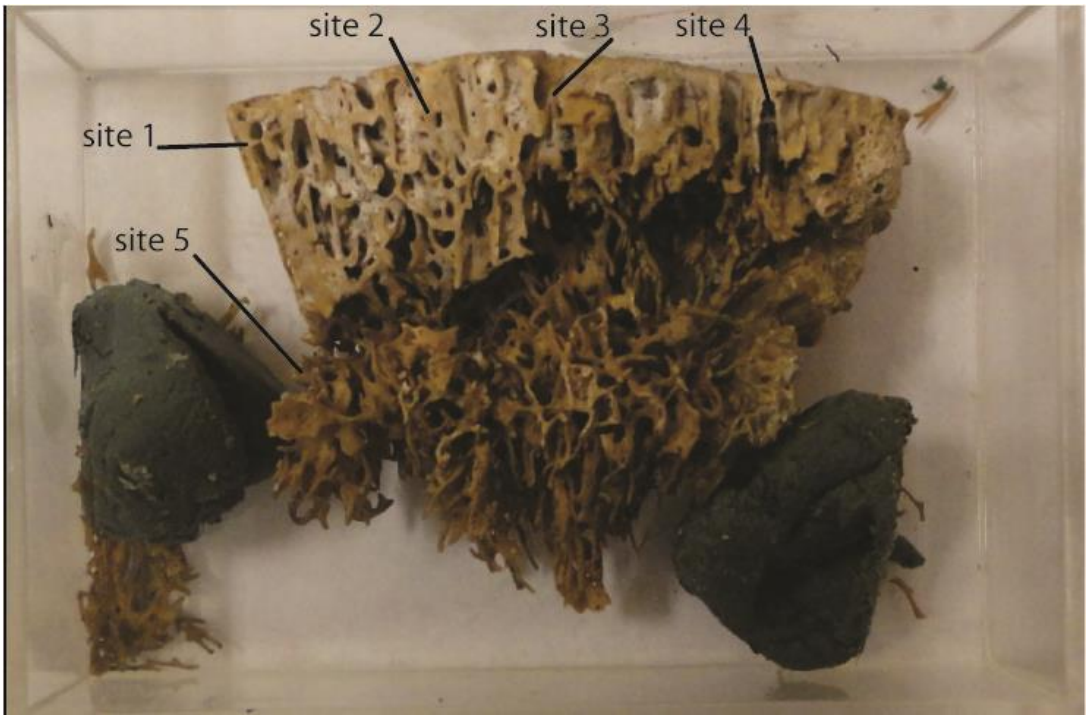

Figure 8: Human skull sample from the Wedda site in Sri Lanka (KUNHM, teaching collection)

Acquisition sites for Raman microspectroscopy are labeled.

Figure 9: Artiodactyl tibia presenting with osteomyelitis (KUNHM, teaching collection). Note the drain present within the swollen diaphysis. Scale bar is 1cm.

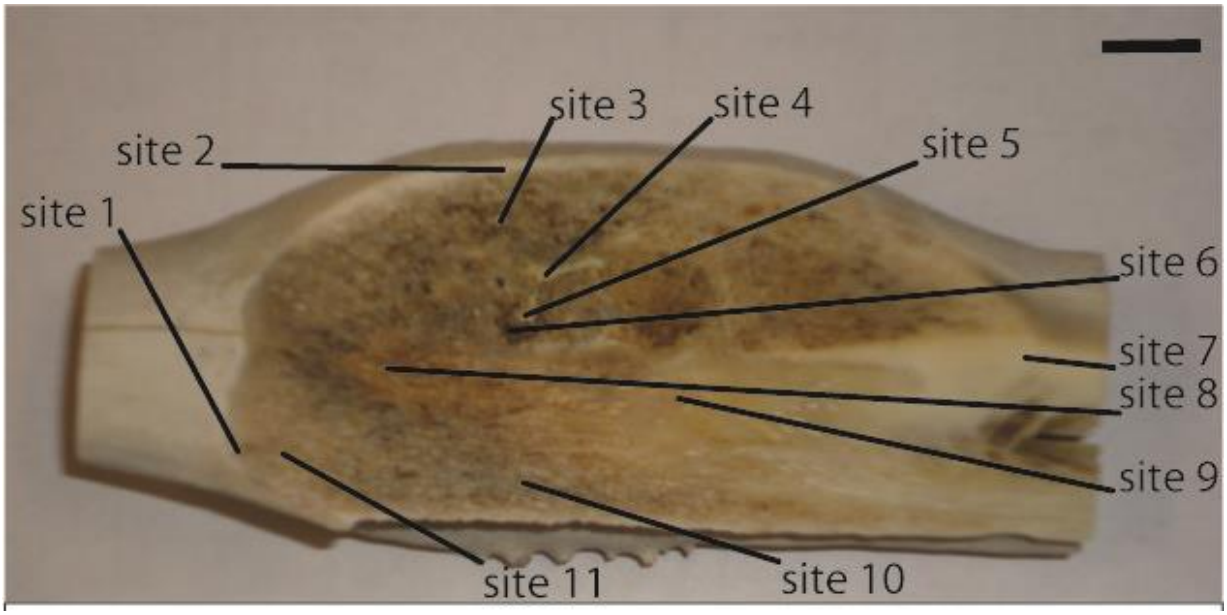

Figure 10: Artiodactyl tibia presenting with osteomyelitis (KUNHM, teaching collection) with spectral acquisition sites. Scale bar is 1cm.

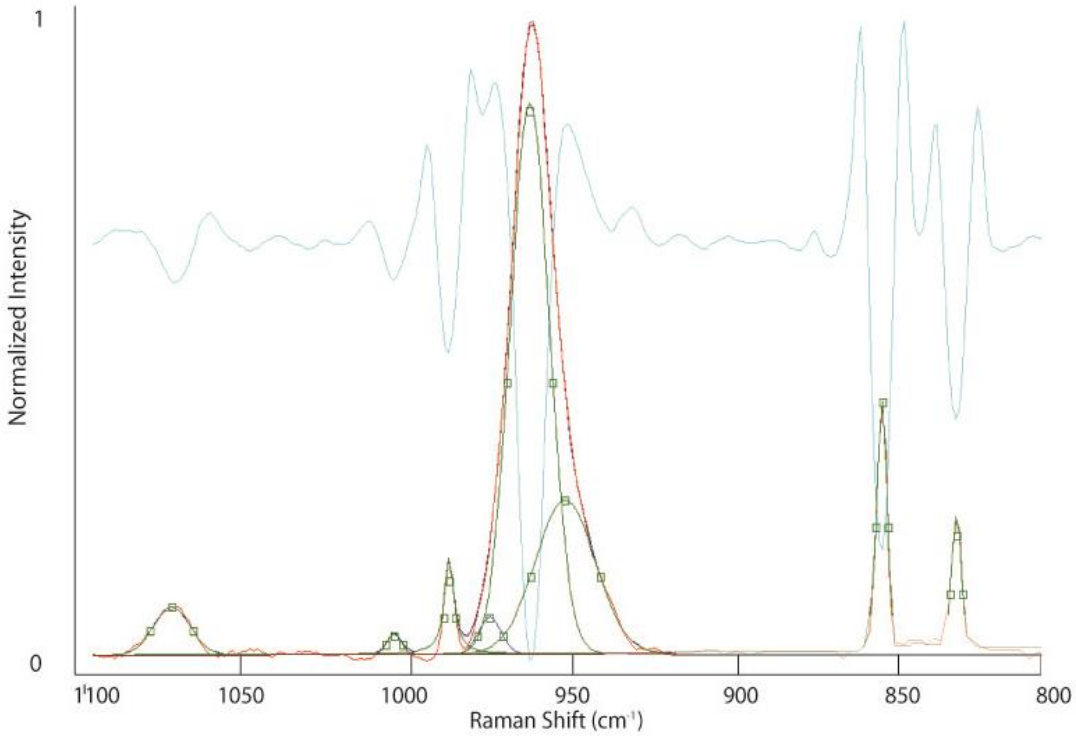

Figure 11: Example of a spectrum deconvoluted into 4 component Gaussian-Lorentzian bands, in GRAMS/AI v. 8. Raman spectrum obtained from artiodactyl sample (KUNHM, teaching collection) presenting with osteomyelitis site 2. Scans were collected with a 785 nm laser at 10% power focused with a 20x refractive glass objective lens for 15 accumulations lasting 10 s. 2nd derivative is shown in blue.

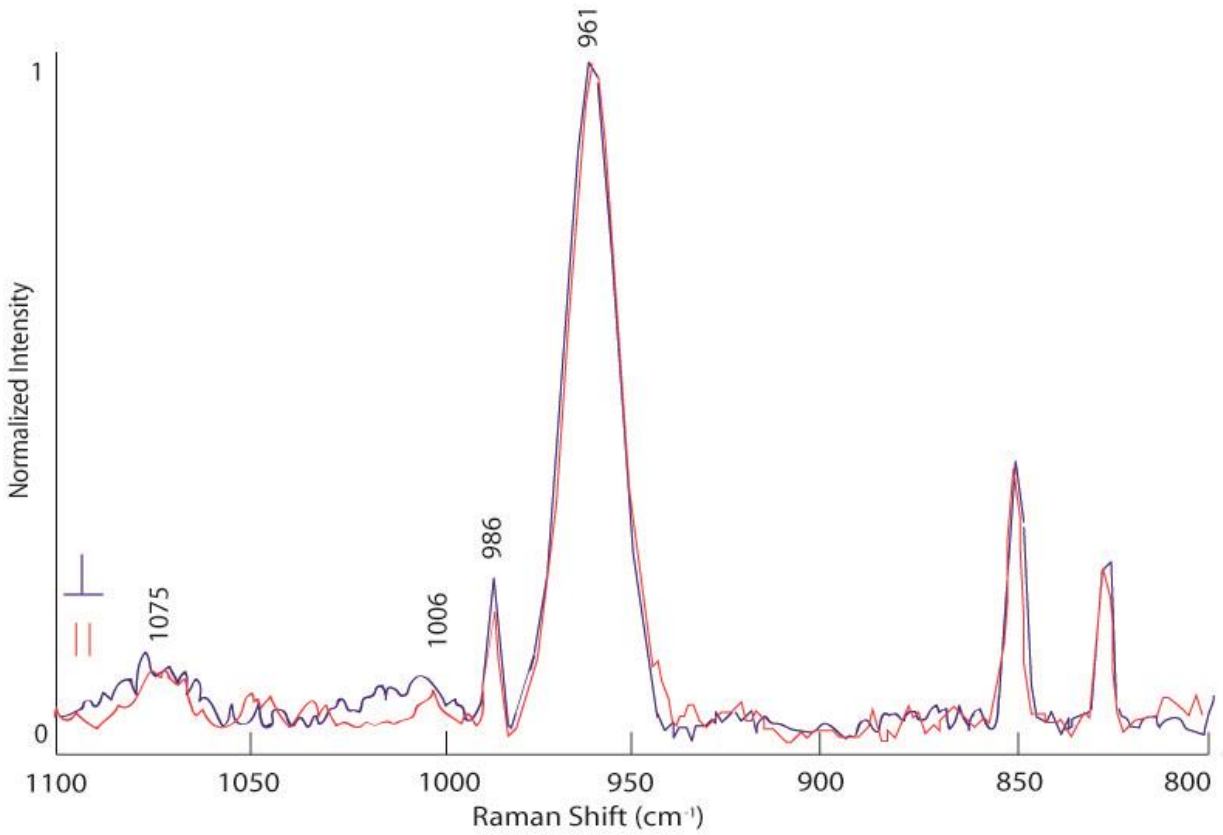

Figure 12: Porotic Hyperostosis sample (KUNHM, teaching collection) polarization experiment conducted at site 2. Scans were collected with a 785 nm laser at 10% power focused with a 10x refractive glass objective lens for 15 accumulations lasting 10 s.

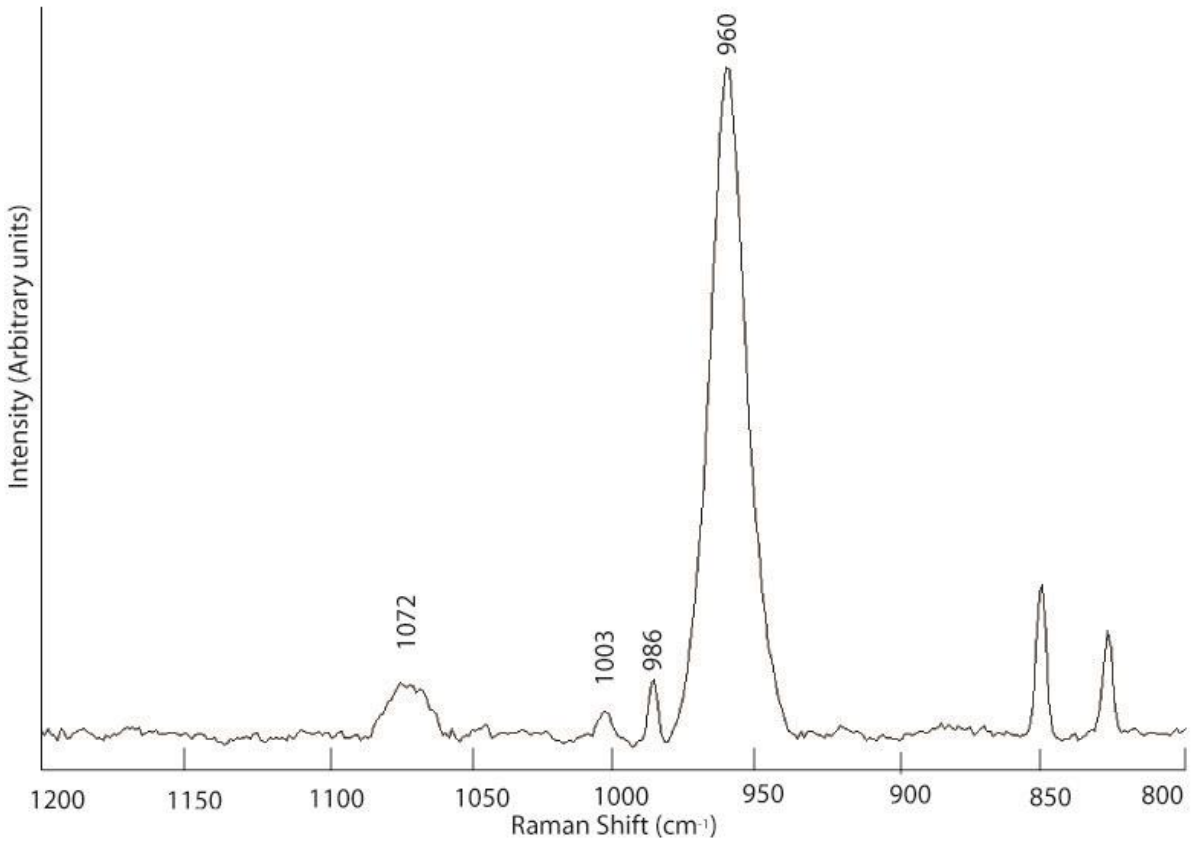

Figure 13: Porotic hyperostosis (KUNHM, teaching collection) site 1. Scans were collected with a 785 nm laser at 10% power focused with a 20x refractive glass objective lens for 15 accumulations lasting 10 s. The band at ~960 Δ cm^{-1} is assigned to the v_1 P-O symmetric stretching mode of the PO_4^{3-} tetrahedron in apatite (Penel et al., 1998). The band present at ~986 Δ cm^{-1} is assigned to the v_1 P-O symmetric stretching mode of the PO_4^{3-} tetrahedron in an apatite precursor such as dicalcium phosphate dihydrate ($CaHPO_4 \cdot 2H_2O$) (Stewart et al., 2002). The band at ~1003 Δ cm^{-1} is assigned to the v_1 P-O symmetric stretching mode of the PO_4^{3-} tetrahedron in HPO_4^{2-} (Penel et al., 1998). The band present at ~1072 Δ cm^{-1} corresponds to a combination of ν_3 P-O anti-symmetric stretching modes of the PO_4^{3-} tetrahedron and a ν_1 C=O symmetric stretching mode for CO_3^{2-} for type B substitutions in apatite (Awonusi et al., 2007).

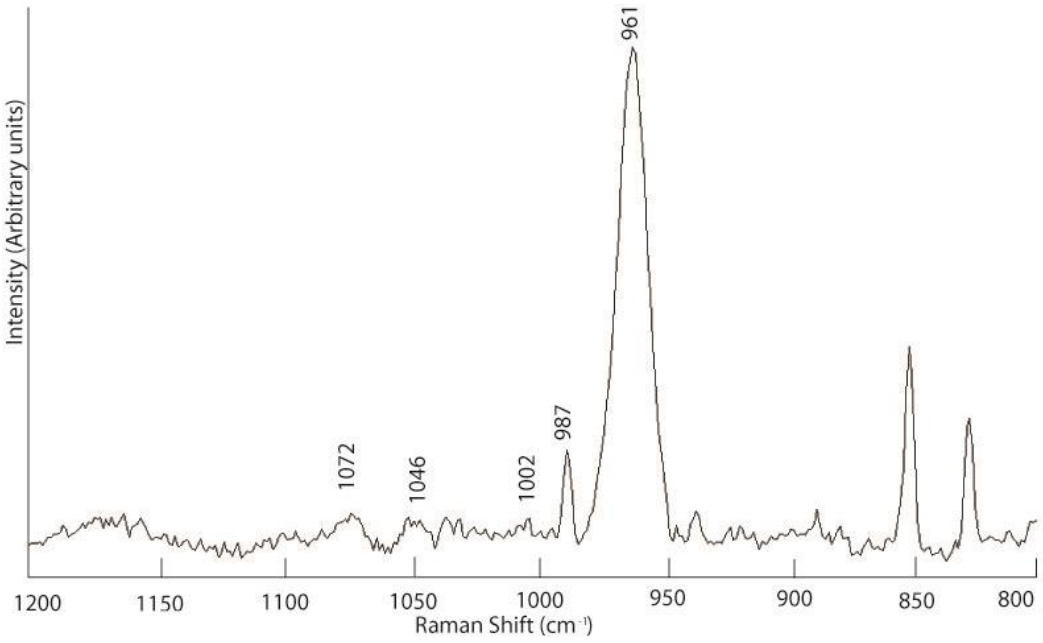

Figure 14: Raman spectrum obtained from porotic hyperostosis sample (KUNHM, teaching collection) site 2. Scans were collected with a 785 nm laser at 5% power focused with a 20x refractive glass objective lens for 1 accumulation lasting 20 s. The band at ~961 Δ cm^{-1} is assigned to the v_1 P-O symmetric stretching mode of the PO_4^{3-} tetrahedron in apatite (Penel et al., 1998). The band present at ~987 Δ cm^{-1} is assigned to the v_1 P-O symmetric stretching mode of the PO_4^{3-} tetrahedron in an apatite precursor such as dicalcium phosphate dihydrate ($CaHPO_4 \cdot 2H_2O$) (Stewart et al., 2002). The band at ~1002 Δ cm^{-1} is assigned to the v_1 P-O symmetric stretching mode of the PO_4^{3-} tetrahedron in HPO_4^{2-} (Penel et al., 1998). The band present at ~1072 Δ cm^{-1} corresponds to a combination of ν_3 P-O anti-symmetric stretching modes of the PO_4^{3-} tetrahedron and a ν_1 C=O symmetric stretching mode for CO_3^{2-} for type B substitutions in apatite (Awonusi et al., 2007). The band present at ~1046 corresponds to a ν_3 P-O anti-symmetric stretching mode in hydroxyapatite (Awonusi et al., 2007).

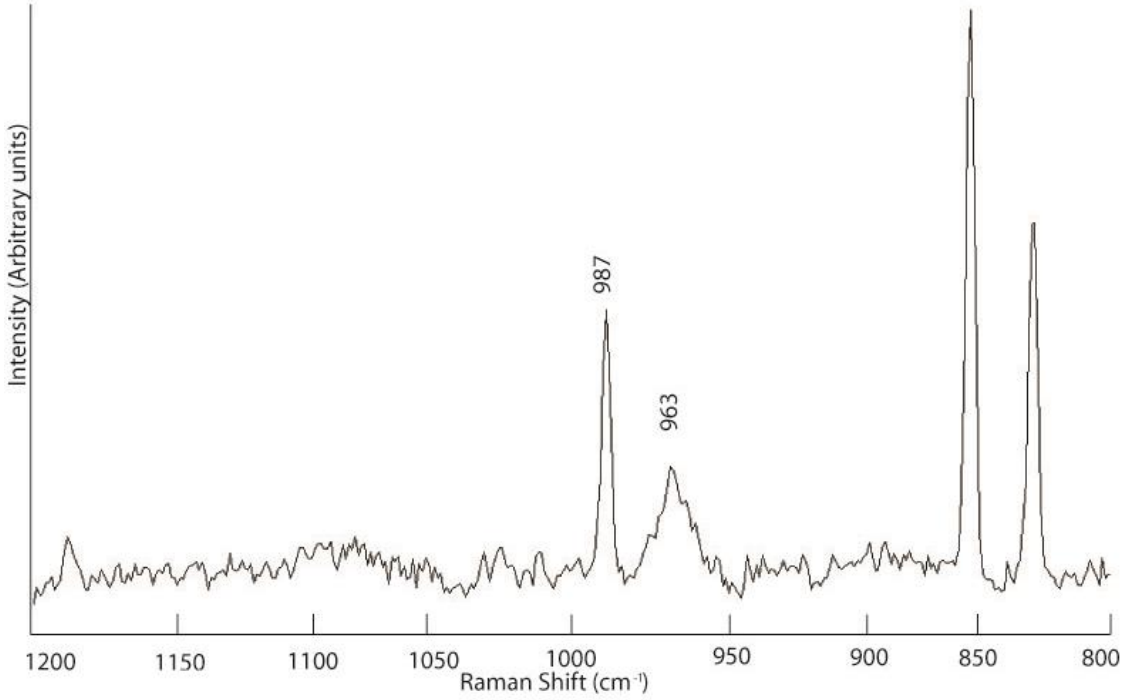

Figure 15: Raman spectrum obtained from Porotic Hyperostosis sample (KUNHM, teaching collection) site 3. Scans were collected with a 785 nm laser at 1% power focused with a 20x refractive glass objective lens for 15 accumulations lasting 30 s. The band at ~963 Δ cm^{-1} is assigned to the v_1 P-O symmetric stretching mode of the PO_4^{3-} tetrahedron in apatite (Penel et al., 1998). The band present at ~987 Δ cm^{-1} is assigned to the v_1 P-O symmetric stretching mode of the PO_4^{3-} tetrahedron in an apatite precursor such as dicalcium phosphate dihydrate ($CaHPO_4 \cdot 2H_2O$) (Stewart et al., 2002).

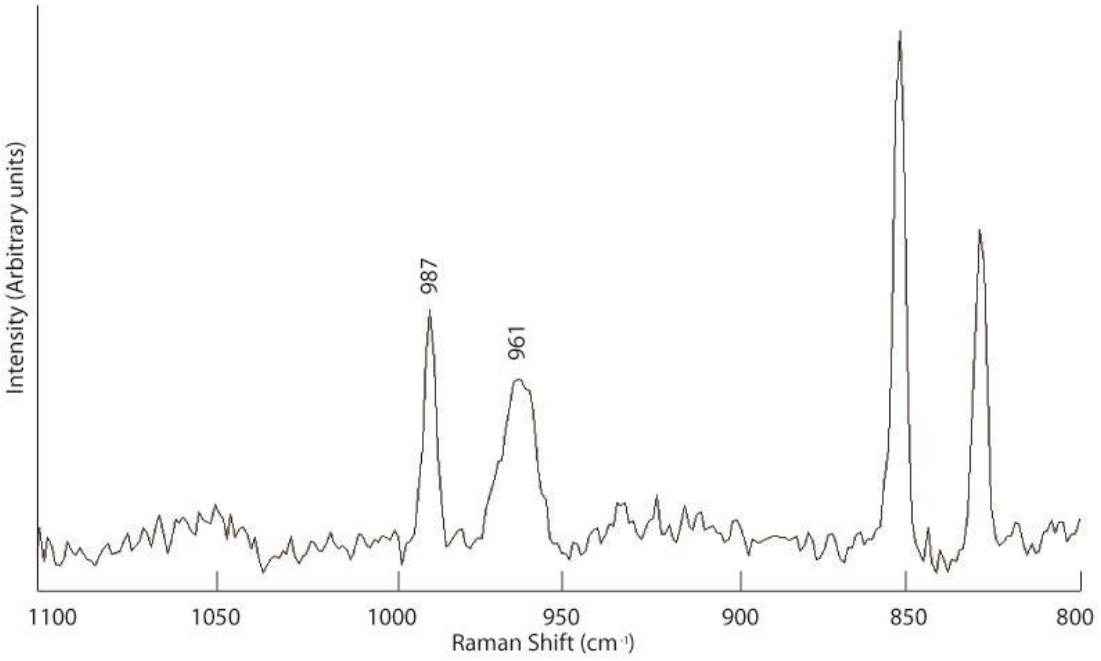

Figure 16: Raman specutrum collected from porotic hyperostosis sample (KUNHM, teaching collection) site 4. Scans were collected with a 785 nm laser at 1% power focused with a 20x refractive glass objective lens for 20 accumulations lasting 15 s. The band at ~961 Δ cm^{-1} is assigned to the v_1 P-O symmetric stretching mode of the PO_4^{3-} tetrahedron in apatite (Penel et al., 1998). The band present at ~987 Δ cm^{-1} is assigned to the v_1 P-O symmetric stretching mode of the PO_4^{3-} tetrahedron in an apatite precursor such as dicalcium phosphate dihydrate ($CaHPO_4 \cdot 2H_2O$) (Stewart et al., 2002).

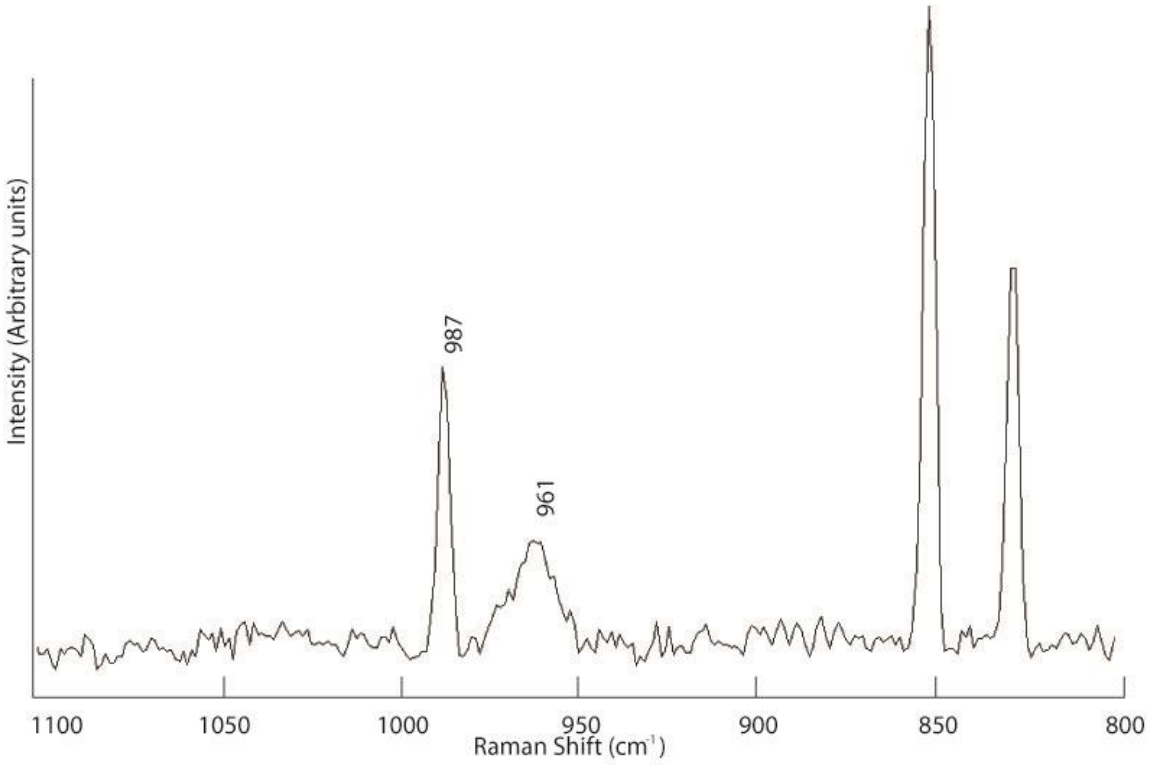

Figure 17: Raman spectrum collected from porotic hyperostosis sample (KUNHM, teaching collection) site 5. Scans were collected with a 785 nm laser at 1% power focused with a 20x refractive glass objective lens for 20 accumulations lasting 10 s. The band at ~961 Δ cm^{-1} is assigned to the v_1 P-O symmetric stretching mode of the PO_4^{3-} tetrahedron in apatite (Penel et al., 1998). The band present at ~987 Δ cm^{-1} is assigned to the v_1 P-O symmetric stretching mode of the PO_4^{3-} tetrahedron in an apatite precursor such as dicalcium phosphate dihydrate ($CaHPO_4 \cdot 2H_2O$) (Stewart et al., 2002).

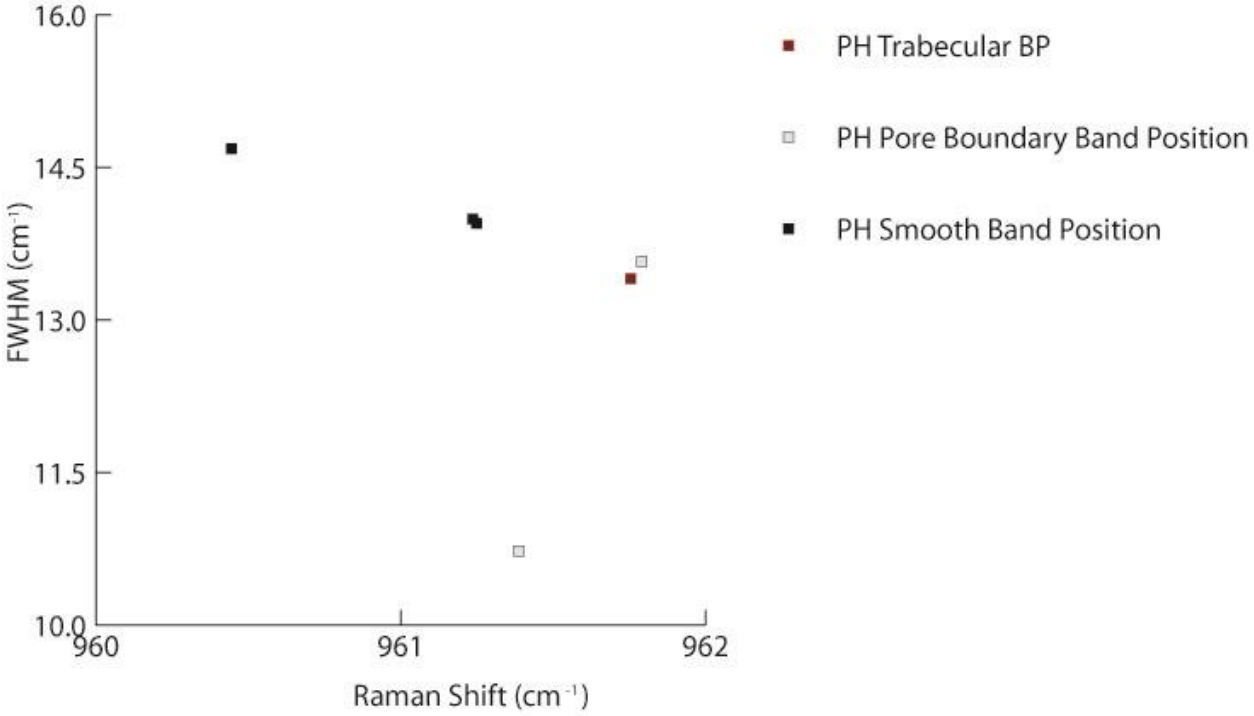

Figure 18: Full width at half maximum (FWHM) and band position data for the v_1 P-O symmetric stretching mode of the PO_4^{3-} tetrahedron in apatite (Penel et al., 1998) from a section of human skull presenting with porotic hyperostosis (PH) (KUNHM, teaching collection).

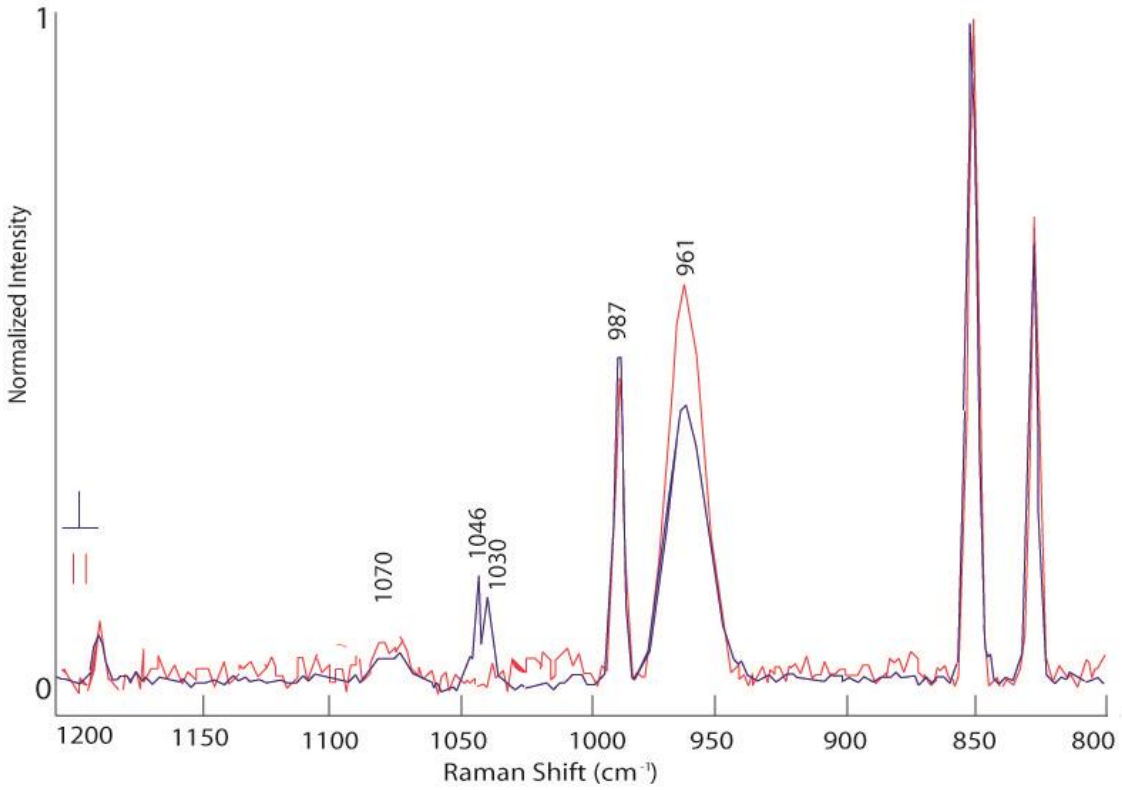

Figure 19: Results of polarization experiment conducted on the cortical bone of the artiodactyl sample (KUNHM, teaching collection). Spectra were collected with a 785 nm laser focused with a 10x refractive glass objective lens for 10 accumulations lasting 10 s. Spectra were then baseline corrected and normalized to the most intense band in WIRE version 3.3. These spectra indicate that these spectra are depolarized. Polarization effects change the intensity of the apatite ν_1 P-O symmetric stretching mode of the PO_4^{3-} tetrahedron in apatite, as well as ν_3 P-O anti-symmetric stretching modes of the PO_4^{3-} at ~1046 and 1030 Δ cm^{-1}.

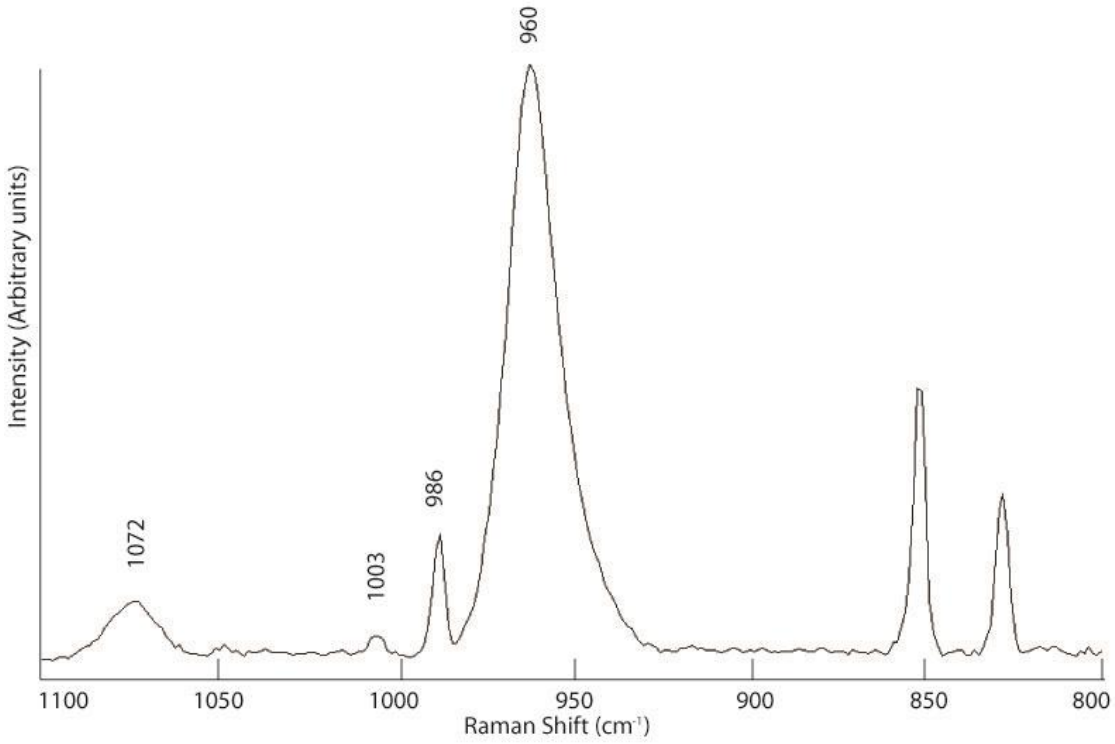

Figure 20: Raman spectrum obtained from artiodactyl sample (KUNHM, teaching collection) presenting with osteomyelitis site 1. Scans were collected with a 785 nm laser at 10% power focused with a 20x refractive glass objective lens for 10 accumulations lasting 10 s. The band at ~960 Δ cm^{-1} is assigned to the ν_1 P-O symmetric stretching mode of the PO_4^{3-} tetrahedron in apatite (Penel et al., 1998). The band present at ~986 Δ cm^{-1} is assigned to the ν_1 P-O symmetric stretching mode of the PO_4^{3-} tetrahedron in an apatite precursor such as dicalcium phosphate dihydrate ($CaHPO_4 \cdot 2H_2O$) (Stewart et al., 2002). The band at ~1003 Δ cm^{-1} is assigned to the ν_1 P-O symmetric stretching mode of the PO_4^{3-} tetrahedron in HPO_4^{2-} (Penel et al., 1998). The band present at ~1072 Δ cm^{-1} corresponds to a combination of ν_3 P-O anti-symmetric stretching modes of the PO_4^{3-} tetrahedron and a ν_1 C=O symmetric stretching mode for CO_3^{2-} for type B substitutions in apatite (Awonusi et al., 2007).

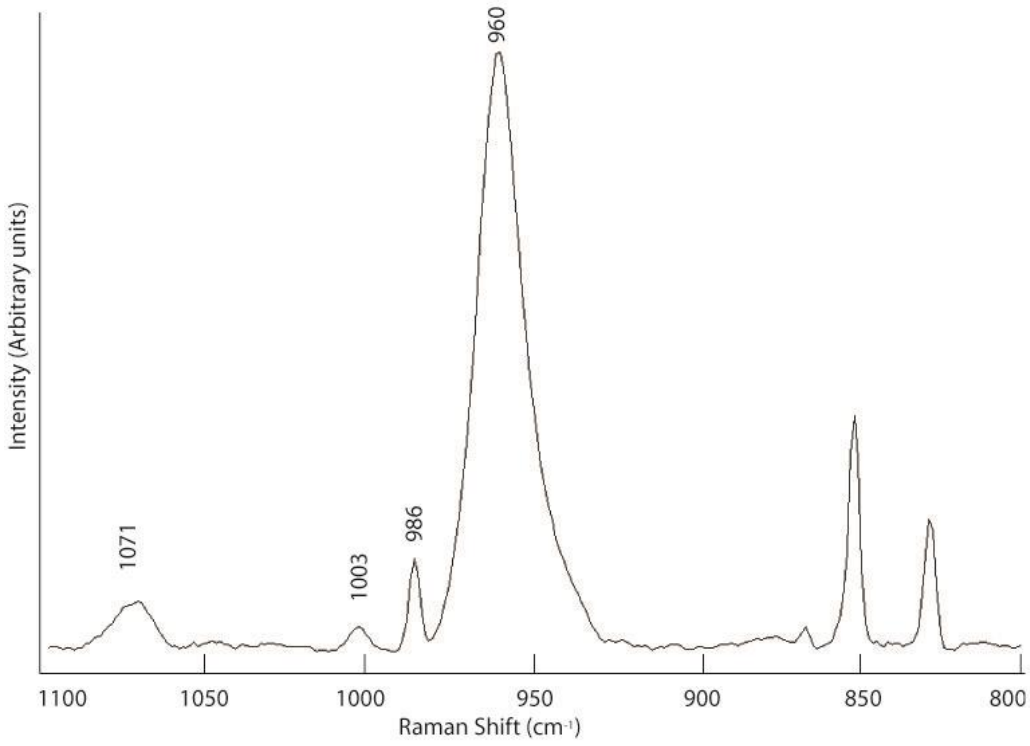

Figure 21: Raman spectrum obtained from artiodactyl sample (KUNHM, teaching collection) presenting with osteomyelitis site 2. Scans were collected with a 785 nm laser at 10% power focused with a 20x refractive glass objective lens for 15 accumulations lasting 10 s. The band at ~960 Δ cm^{-1} is assigned to the v_1 P-O symmetric stretching mode of the PO_4^{3-} tetrahedron in apatite (Penel et al., 1998). The band present at ~986 Δ cm^{-1} is assigned to the v_1 P-O symmetric stretching mode of the PO_4^{3-} tetrahedron in an apatite precursor such as dicalcium phosphate dihydrate ($CaHPO_4 \cdot 2H_2O$) (Stewart et al., 2002). The band at ~1003 Δ cm^{-1} is assigned to the v_1 P-O symmetric stretching mode of the PO_4^{3-} tetrahedron in HPO_4^{2-} (Penel et al., 1998). The band present at ~1071 Δ cm^{-1} corresponds to a combination of v_3 P-O anti-symmetric stretching modes of the PO_4^{3-} tetrahedron and a v_1 C=O symmetric stretching mode for CO_3^{2-} for type B substitutions in apatite (Awonusi et al., 2007).

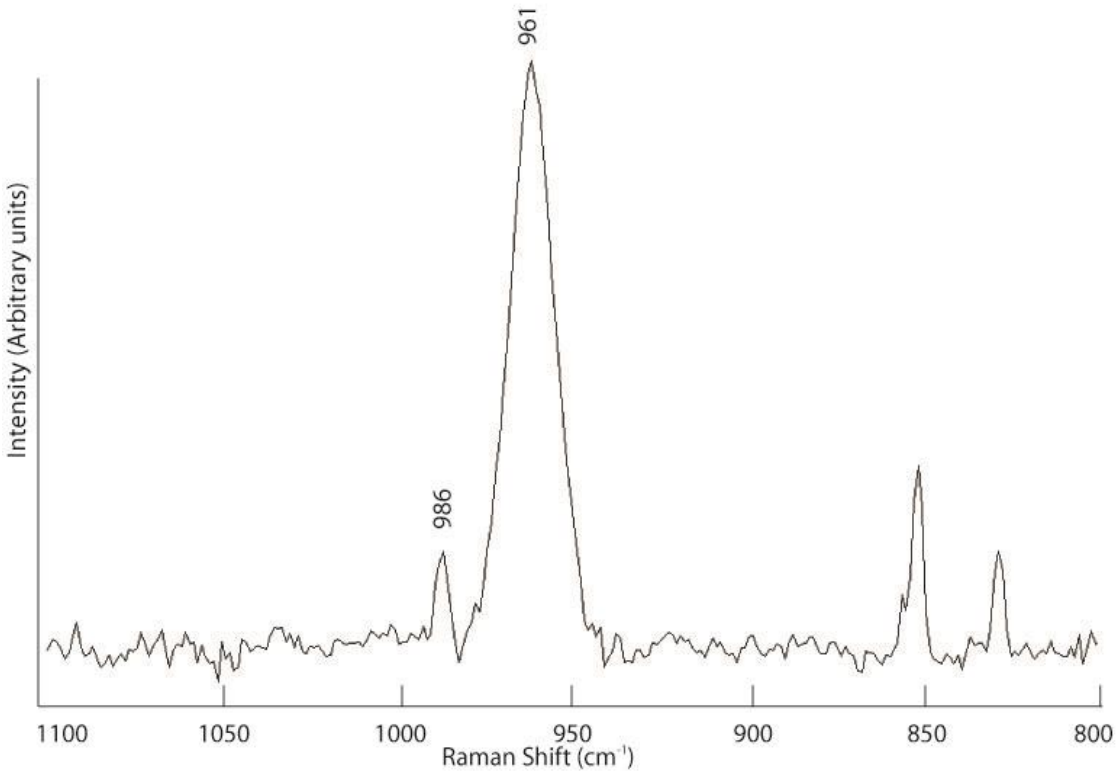

Figure 22: Raman spectrum obtained from artiodactyl sample (KUNHM, teaching collection) presenting with osteomyelitis site 3. Scans were collected with a 785 nm laser at 10% power focused with a 20x refractive glass objective lens for 15 accumulations lasting 10 s. The band at ~961 Δ cm^{-1} is assigned to the v_1 P-O symmetric stretching mode of the PO_4^{3-} tetrahedron in apatite (Penel et al., 1998). The band present at ~986 Δ cm^{-1} is assigned to the v_1 P-O symmetric stretching mode of the PO_4^{3-} tetrahedron in an apatite precursor such as dicalcium phosphate dihydrate ($CaHPO_4 \cdot 2H_2O$) (Stewart et al., 2002).

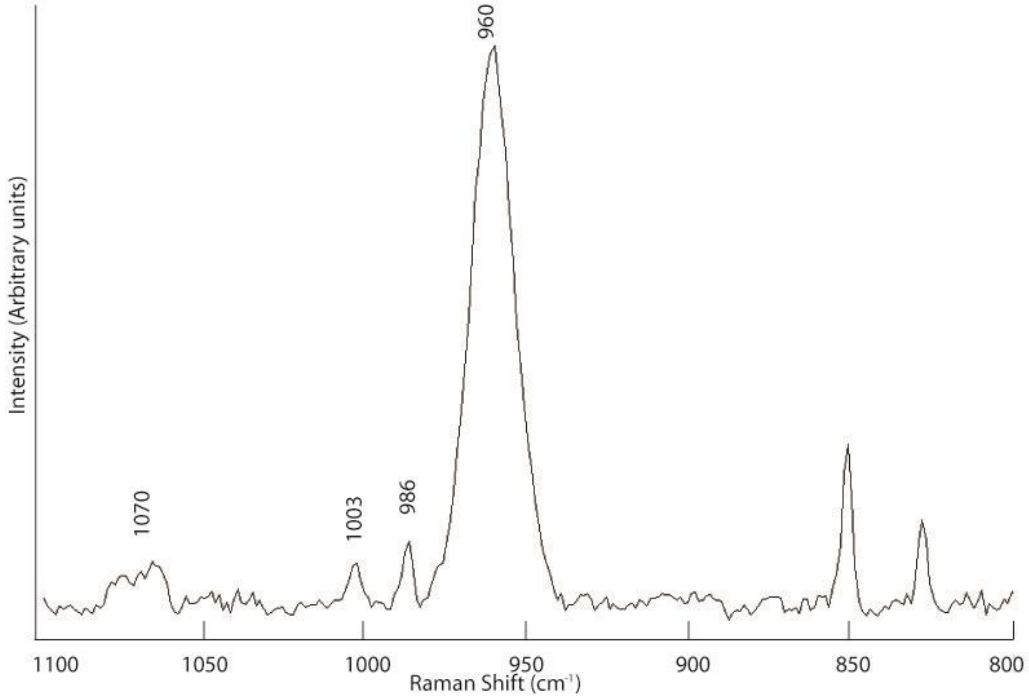

Figure 23: Raman spectrum obtained from artiodactyl sample (KUNHM, teaching collection) presenting with osteomyelitis site 4. Scans were collected with a 785 nm laser at 10% power focused with a 20x refractive glass objective lens for 15 accumulations lasting 10 s. The band at ~960 Δ cm^{-1} is assigned to the v_1 P-O symmetric stretching mode of the PO_4^{3-} tetrahedron in apatite (Penel et al., 1998). The band present at ~986 Δ cm^{-1} is assigned to the v_1 P-O symmetric stretching mode of the PO_4^{3-} tetrahedron in an apatite precursor such as dicalcium phosphate dihydrate ($CaHPO_4 \cdot 2H_2O$) (Stewart et al., 2002). The band at ~1003 Δ cm^{-1} is assigned to the v_1 P-O symmetric stretching mode of the PO_4^{3-} tetrahedron in HPO_4^{2-} (Penel et al., 1998). The band present at ~1070 Δ cm^{-1} corresponds to a combination of v_3 P-O anti-symmetric stretching modes of the PO_4^{3-} tetrahedron and a v_1 C=O symmetric stretching mode for CO_3^{2-} for type B substitutions in apatite (Awonusi et al., 2007).

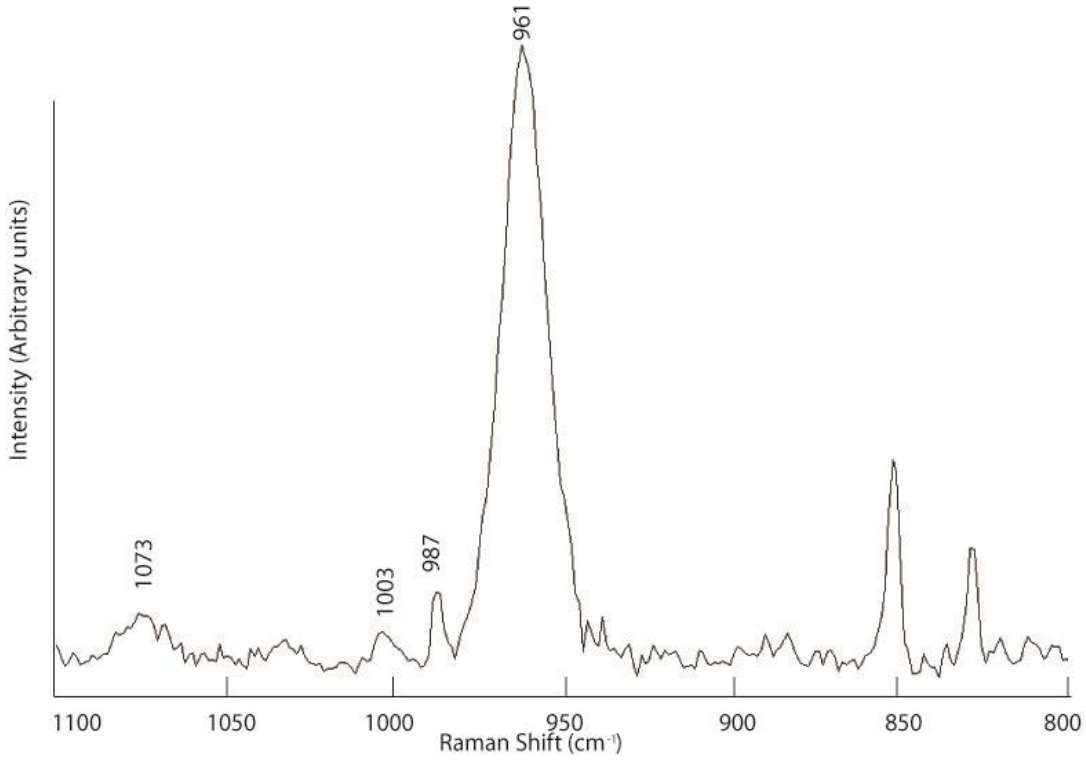

Figure 24: Raman spectrum obtained from artiodactyl sample (KUNHM, teaching collection) presenting with osteomyelitis site 5. Scans were collected with a 785 nm laser at 10% power focused with a 20x refractive glass objective lens for 15 accumulations lasting 10 s. The band at ~961 Δ cm^{-1} is assigned to the v_1 P-O symmetric stretching mode of the PO_4^{3-} tetrahedron in apatite (Penel et al., 1998). The band present at ~987 Δ cm^{-1} is assigned to the v_1 P-O symmetric stretching mode of the PO_4^{3-} tetrahedron in an apatite precursor such as dicalcium phosphate dihydrate ($CaHPO_4 \cdot 2H_2O$) (Stewart et al., 2002). The band at ~1003 Δ cm^{-1} is assigned to the v_1 P-O symmetric stretching mode of the PO_4^{3-} tetrahedron in HPO_4^{2-} (Penel et al., 1998). The band present at ~1073 Δ cm^{-1} corresponds to a combination of ν_3 P-O anti-symmetric stretching modes of the PO_4^{3-} tetrahedron and a ν_1 C=O symmetric stretching mode for CO_3^{2-} for type B substitutions in apatite (Awonusi et al., 2007).

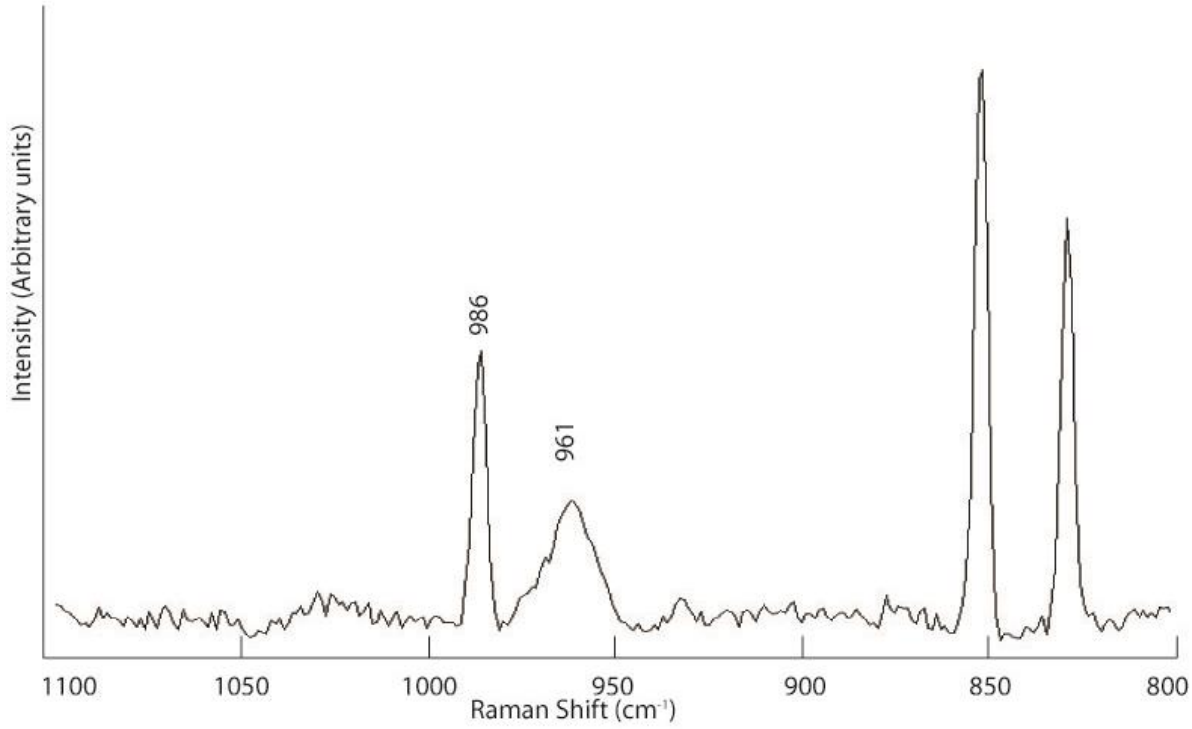

Figure 25: Raman spectrum obtained from artiodactyl sample (KUNHM, teaching collection) presenting with osteomyelitis site 6. Scans were collected with a 785 nm laser at 1% power focused with a 20x refractive glass objective lens for 20 accumulations lasting 20 s. The band at ~961 Δ cm^{-1} is assigned to the v_1 P-O symmetric stretching mode of the PO_4^{3-} tetrahedron in apatite (Penel et al., 1998). The band present at ~986 Δ cm^{-1} is assigned to the v_1 P-O symmetric stretching mode of the PO_4^{3-} tetrahedron in an apatite precursor such as dicalcium phosphate dihydrate ($CaHPO_4 \cdot 2H_2O$) (Stewart et al., 2002).

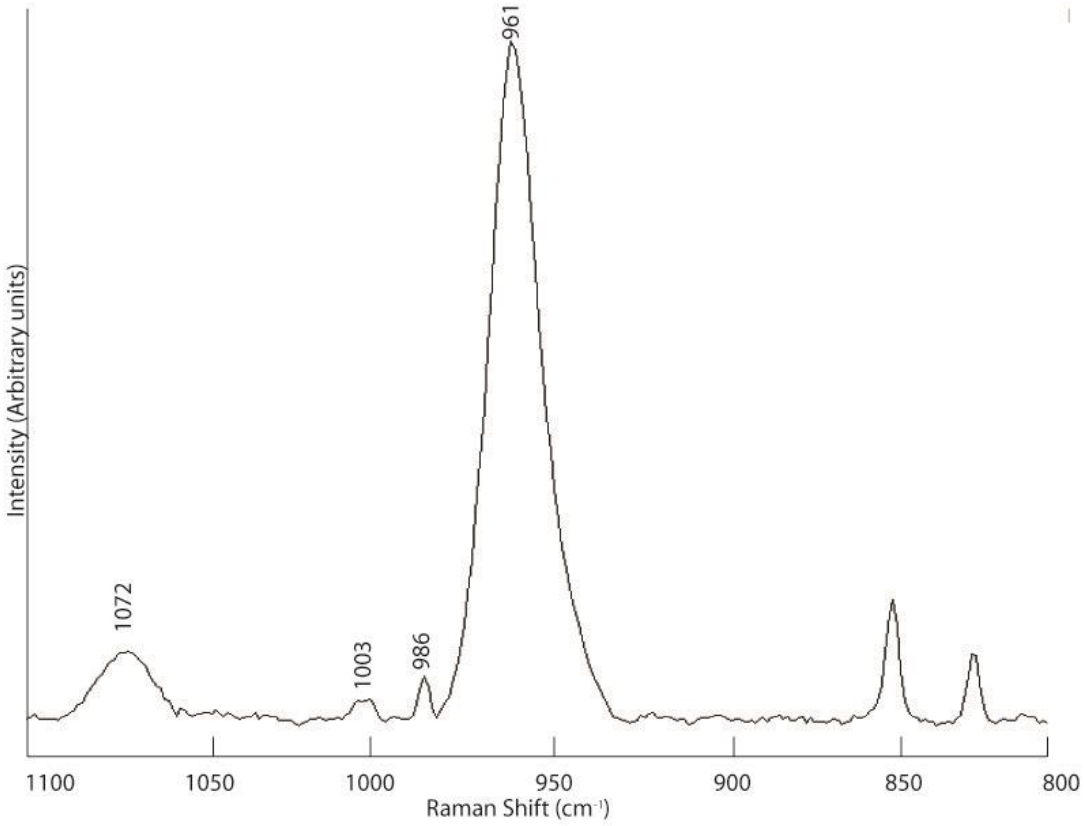

Figure 26: Raman spectrum obtained from artiodactyl sample (KUNHM, teaching collection) presenting with osteomyelitis site 7. Scans were collected with a 785 nm laser at 10% power focused with a 20x refractive glass objective lens for 15 accumulations lasting 10 s. The band at ~961 Δ cm^{-1} is assigned to the v_1 P-O symmetric stretching mode of the PO_4^{3-} tetrahedron in apatite (Penel et al., 1998). The band present at ~986 Δ cm^{-1} is assigned to the v_1 P-O symmetric stretching mode of the PO_4^{3-} tetrahedron in an apatite precursor such as dicalcium phosphate dihydrate ($CaHPO_4 \cdot 2H_2O$) (Stewart et al., 2002). The band at ~1003 Δ cm^{-1} is assigned to the v_1 P-O symmetric stretching mode of the PO_4^{3-} tetrahedron in HPO_4^{2-} (Penel et al., 1998). The band present at ~1072 Δ cm^{-1} corresponds to a combination of ν_3 P-O anti-symmetric stretching modes of the PO_4^{3-} tetrahedron and a ν_1 C=O symmetric stretching mode for CO_3^{2-} for type B substitutions in apatite (Awonusi et al., 2007).

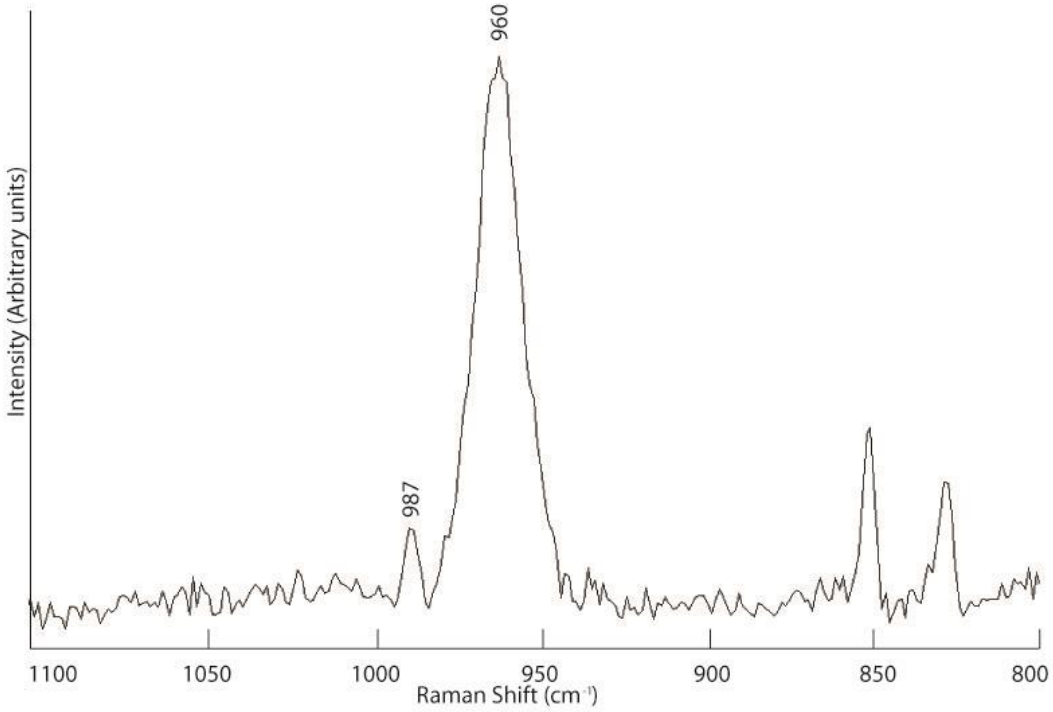

Figure 27: Raman spectrum obtained from artiodactyl sample (KUNHM, teaching collection) presenting with osteomyelitis site 8. Scans were collected with a 785 nm laser at 5% power focused with a 20x refractive glass objective lens for 15 accumulations lasting 10 s. The band at ~960 Δ cm^{-1} is assigned to the v_1 P-O symmetric stretching mode of the PO_4^{3-} tetrahedron in apatite (Penel et al., 1998). The band present at ~987 Δ cm^{-1} is assigned to the v_1 P-O symmetric stretching mode of the PO_4^{3-} tetrahedron in an apatite precursor such as dicalcium phosphate dihydrate ($CaHPO_4 \cdot 2H_2O$) (Stewart et al., 2002).

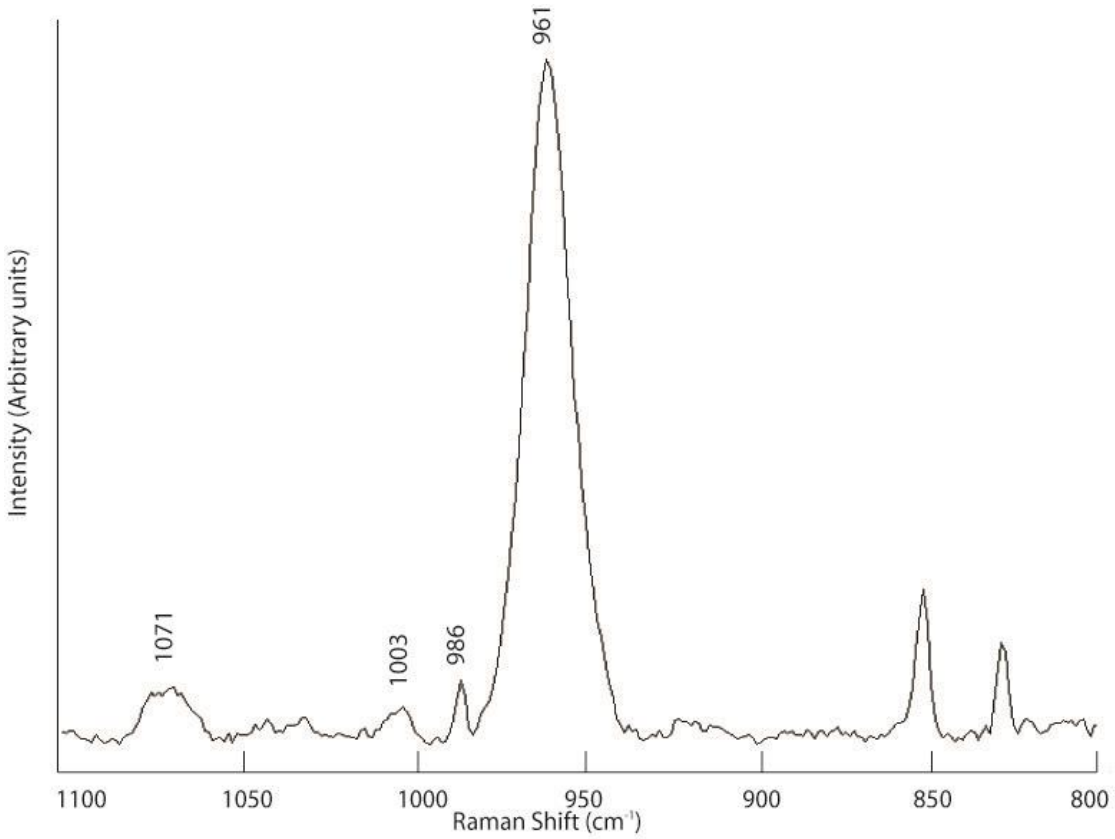

Figure 28: Raman spectrum obtained from artiodactyl sample (KUNHM, teaching collection) presenting with osteomyelitis site 9. Scans were collected with a 785 nm laser at 10% power focused with a 20x refractive glass objective lens for 10 accumulations lasting 10 s. The band at ~961 Δ cm^{-1} is assigned to the ν_1 P-O symmetric stretching mode of the PO_4^{3-} tetrahedron in apatite (Penel et al., 1998). The band present at ~986 Δ cm^{-1} is assigned to the ν_1 P-O symmetric stretching mode of the PO_4^{3-} tetrahedron in an apatite precursor such as dicalcium phosphate dihydrate ($CaHPO_4 \cdot 2H_2O$) (Stewart et al., 2002). The band at ~1003 Δ cm^{-1} is assigned to the ν_1 P-O symmetric stretching mode of the PO_4^{3-} tetrahedron in HPO_4^{2-} (Penel et al., 1998). The band present at ~1071 Δ cm^{-1} corresponds to a combination of ν_3 P-O anti-symmetric stretching modes of the PO_4^{3-} tetrahedron and a ν_1 C=O symmetric stretching mode for CO_3^{2-} for type B substitutions in apatite (Awonusi et al., 2007).

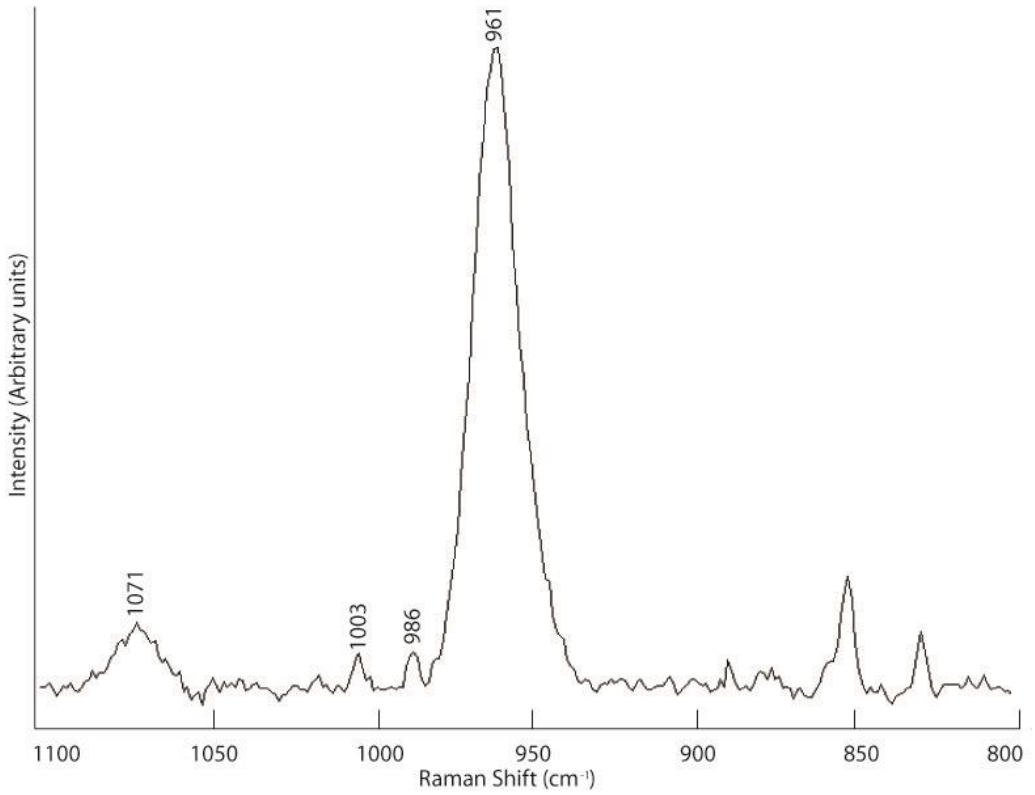

Figure 29: Raman spectrum obtained from artiodactyl sample (KUNHM, teaching collection) presenting with osteomyelitis site 10. Scans were collected with a 785 nm laser at 10% power focused with a 20x refractive glass objective lens for 15 accumulations lasting 10 s The band at ~961 Δ cm^{-1} is assigned to the ν_1 P-O symmetric stretching mode of the PO_4^{3-} tetrahedron in apatite (Penel et al., 1998). The band present at ~986 Δ cm^{-1} is assigned to the ν_1 P-O symmetric stretching mode of the PO_4^{3-} tetrahedron in an apatite precursor such as dicalcium phosphate dihydrate ($CaHPO_4 \cdot 2H_2O$) (Stewart et al., 2002). The band at ~1003 Δ cm^{-1} is assigned to the ν_1 P-O symmetric stretching mode of the PO_4^{3-} tetrahedron in HPO_4^{2-} (Penel et al., 1998). The band present at ~1071 Δ cm^{-1} corresponds to a combination of ν_3 P-O anti-symmetric stretching modes of the PO_4^{3-} tetrahedron and a ν_1 C=O symmetric stretching mode for CO_3^{2-} for type B substitutions in apatite (Awonusi et al., 2007).

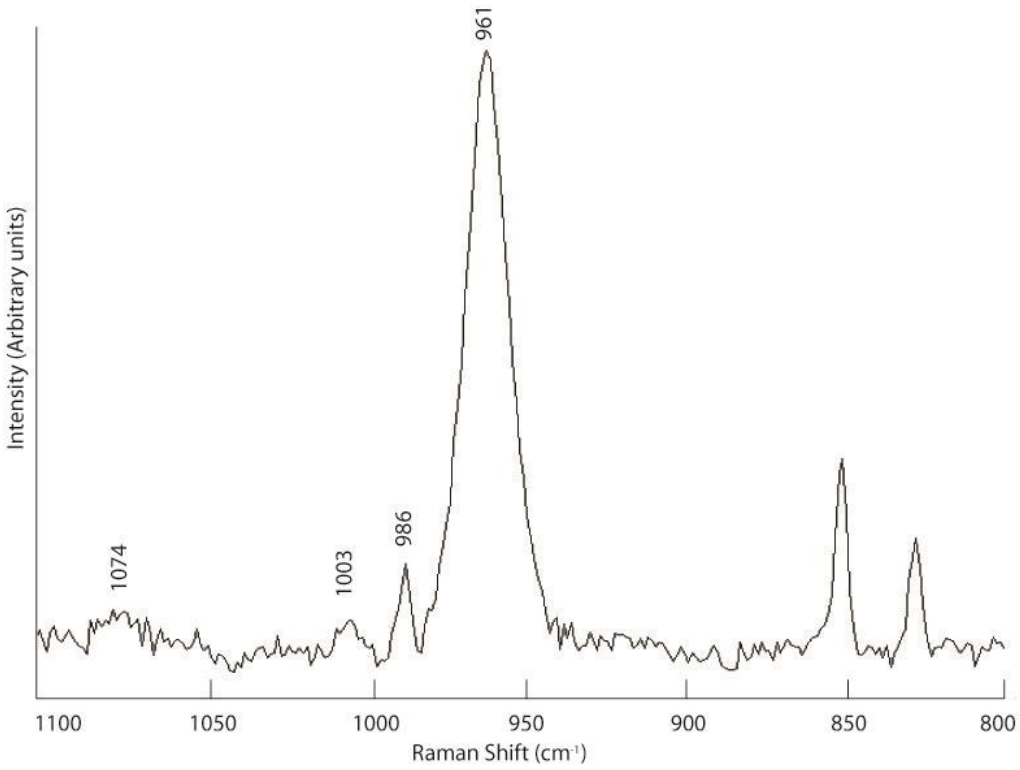

Figure 30: Raman spectrum obtained from artiodactyl sample (KUNHM, teaching collection) presenting with osteomyelitis site 11. Scans were collected with a 785 nm laser at 10% power focused with a 20x refractive glass objective lens for 15 accumulations lasting 10 s. The band at ~961 Δ cm^{-1} is assigned to the v_1 P-O symmetric stretching mode of the PO_4^{3-} tetrahedron in apatite (Penel et al., 1998). The band present at ~986 Δ cm^{-1} is assigned to the v_1 P-O symmetric stretching mode of the PO_4^{3-} tetrahedron in an apatite precursor such as dicalcium phosphate dihydrate ($CaHPO_4 \cdot 2H_2O$) (Stewart et al., 2002). The band at ~1003 Δ cm^{-1} is assigned to the v_1 P-O symmetric stretching mode of the PO_4^{3-} tetrahedron in HPO_4^{2-} (Penel et al., 1998). The band present at ~1074 Δ cm^{-1} corresponds to a combination of ν_3 P-O anti-symmetric stretching modes of the PO_4^{3-} tetrahedron and a ν_1 C=O symmetric stretching mode for CO_3^{2-} for type B substitutions in apatite (Awonusi et al., 2007).

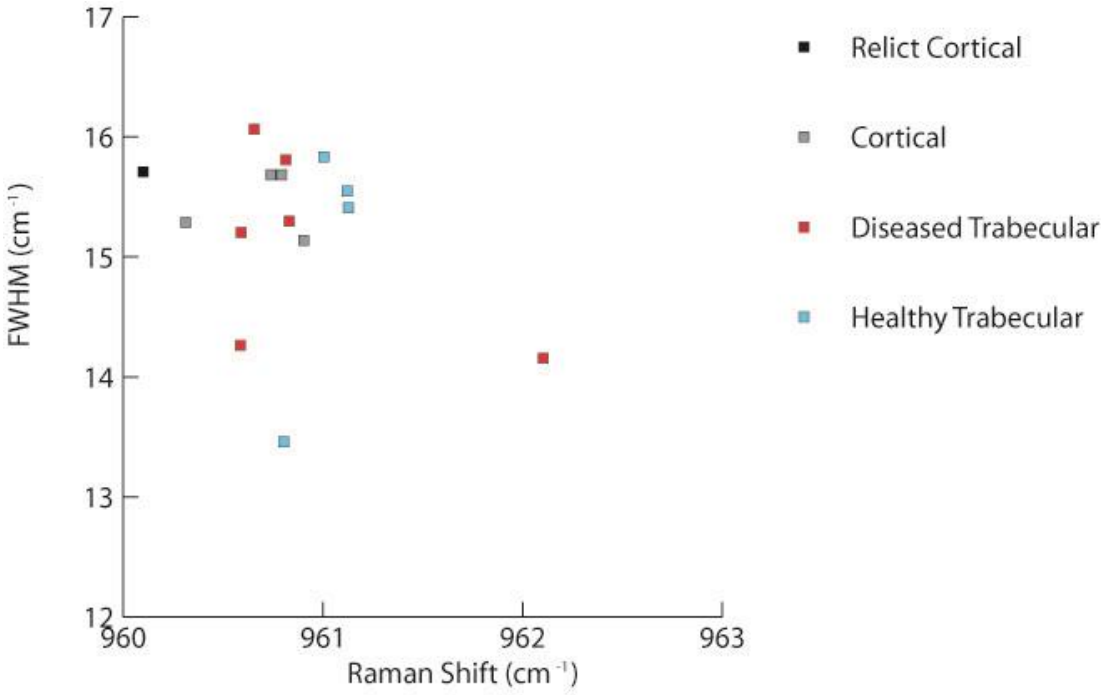

Figure 31: Full width at half maximum (FWHM) and band position data for the ν_1 P-O symmetric stretching mode of the PO_4^{3-} tetrahedron in an artiodactyl tibia presenting with osteomyelitis (KUNHM, teaching collection). Trabecular bone which appears diseased (red) does not vary significantly from healthy trabecular bone (blue). Values for cortical bone are shown in gray. Values for site 4, a dead fragment of cortical bone, are depicted in black.

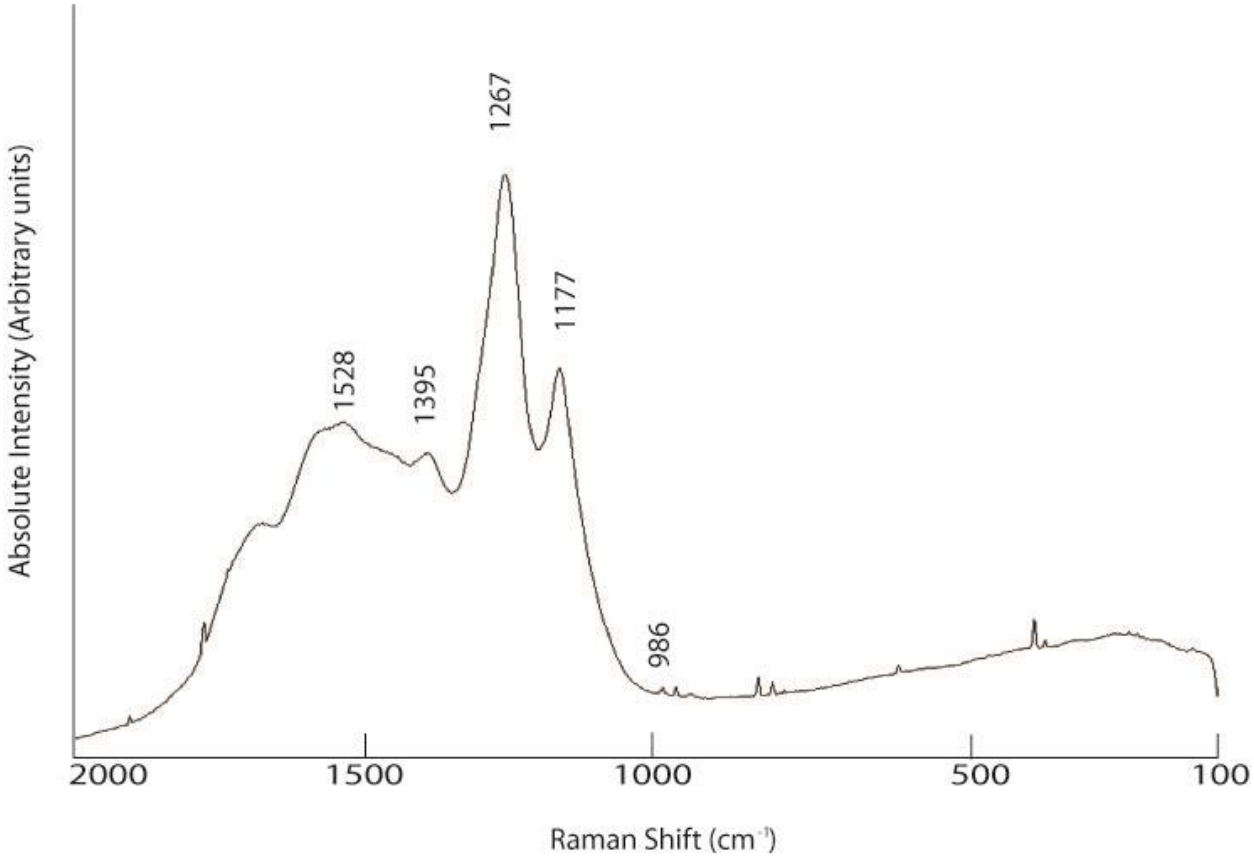

Figure 32: Raman spectrum obtained from the central phosphatic pillar of the urolith (KUVP 148307). Scans were collected with a 785 nm laser at 1% power focused with a 20x refractive glass objective lens for 10 accumulations lasting 10 s. Numerous bands associated with PAHs are present between 1100 and 1600 Δ cm^{-1} . The band at ~986 cm^{-1} is assigned to the ν_1 P-O symmetric stretching mode of the PO_4^{3-} tetrahedron in an apatite precursor such as dicalcium phosphate dihydrate (Stewart, 2002).

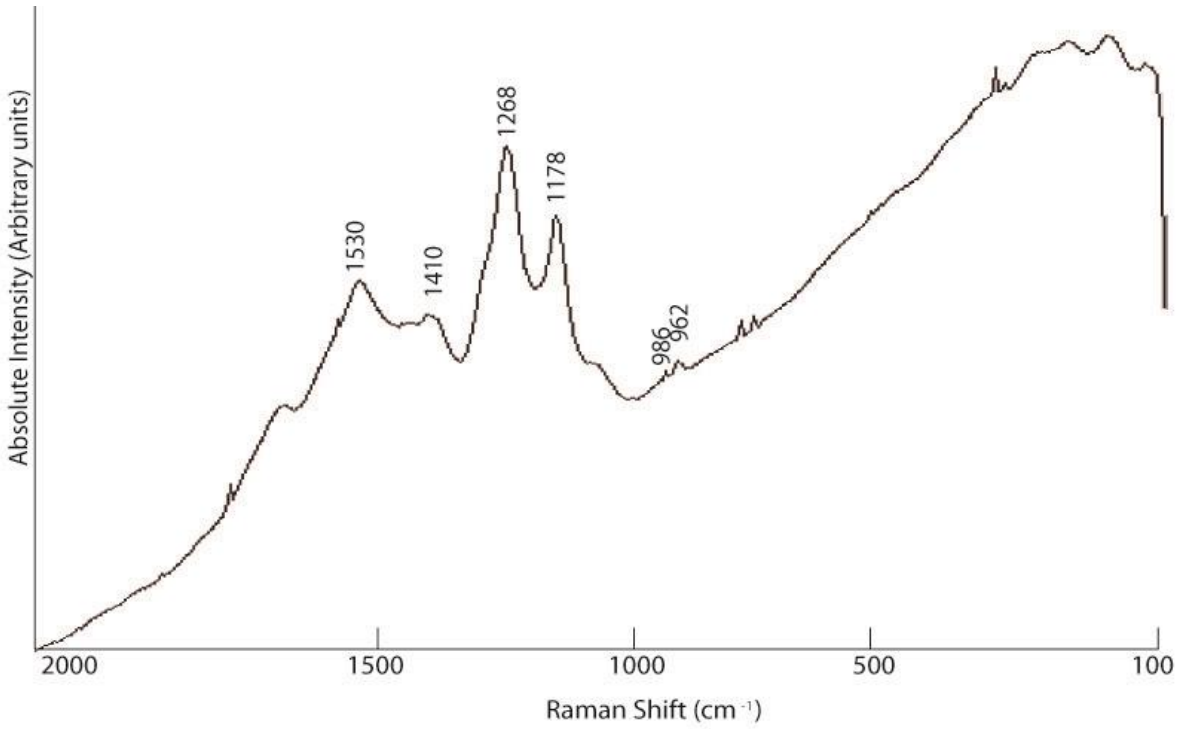

Figure 33: Raman spectrum obtained from the outermost layer of the urolith (KUVP 148307). Scans were collected with a 785 nm laser at 0.5% power focused with a 20x refractive glass objective lens for 10 accumulations lasting 10 s. Numerous bands associated with PAHs are present between 1100 and 1600 Δ cm^{-1} . The band at ~962 Δ cm^{-1} is assigned to the dominant ν_1 P-O symmetric stretching mode of the PO_4^{3-} tetrahedron in apatite (Penel et al., 1998). The band at ~986 cm^{-1} is assigned to a phosphate P-O symmetric stretching mode (Stewart et al., 2002).

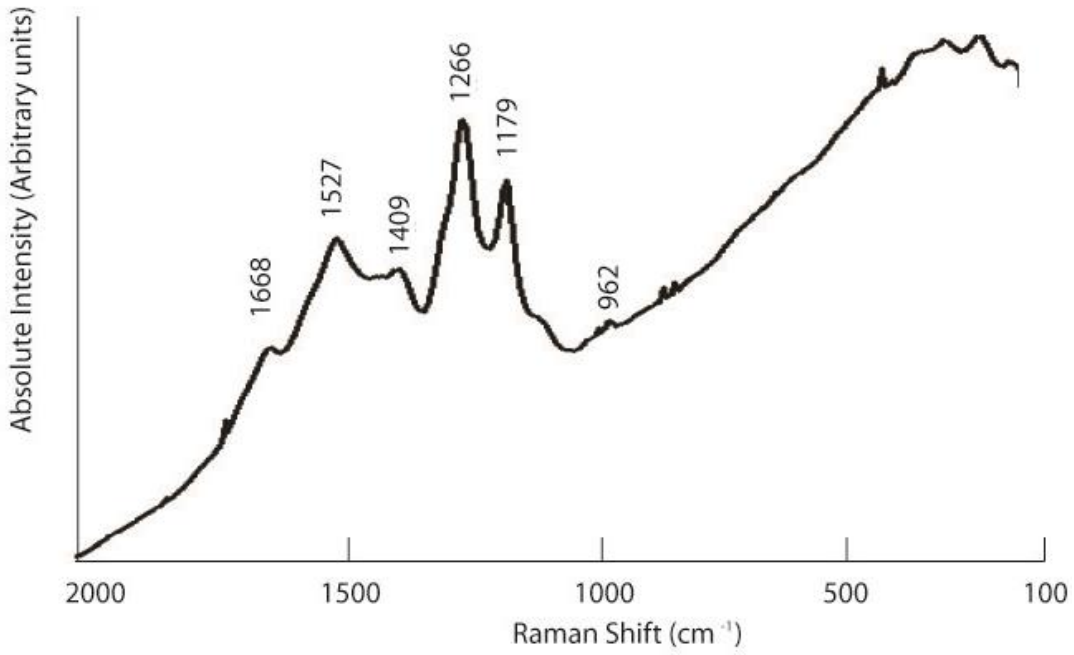

Figure 34: Raman spectrum obtained from one of the concentric layers of the urolith (KUVP 148307). Scans were collected with a 785 nm laser at 0.5% power focused with a 20x refractive glass objective lens for 10 accumulations lasting 10 s. Numerous bands associated with C-C and C=C stretching modes due to PAHs are present between 1100 and 1700 Δ cm^{-1}. The band at ~962 Δ cm^{-1} is assigned to the dominant ν_1 P-O symmetric stretching mode of the PO_4^{3-} tetrahedron in apatite (Penel et al., 1998).

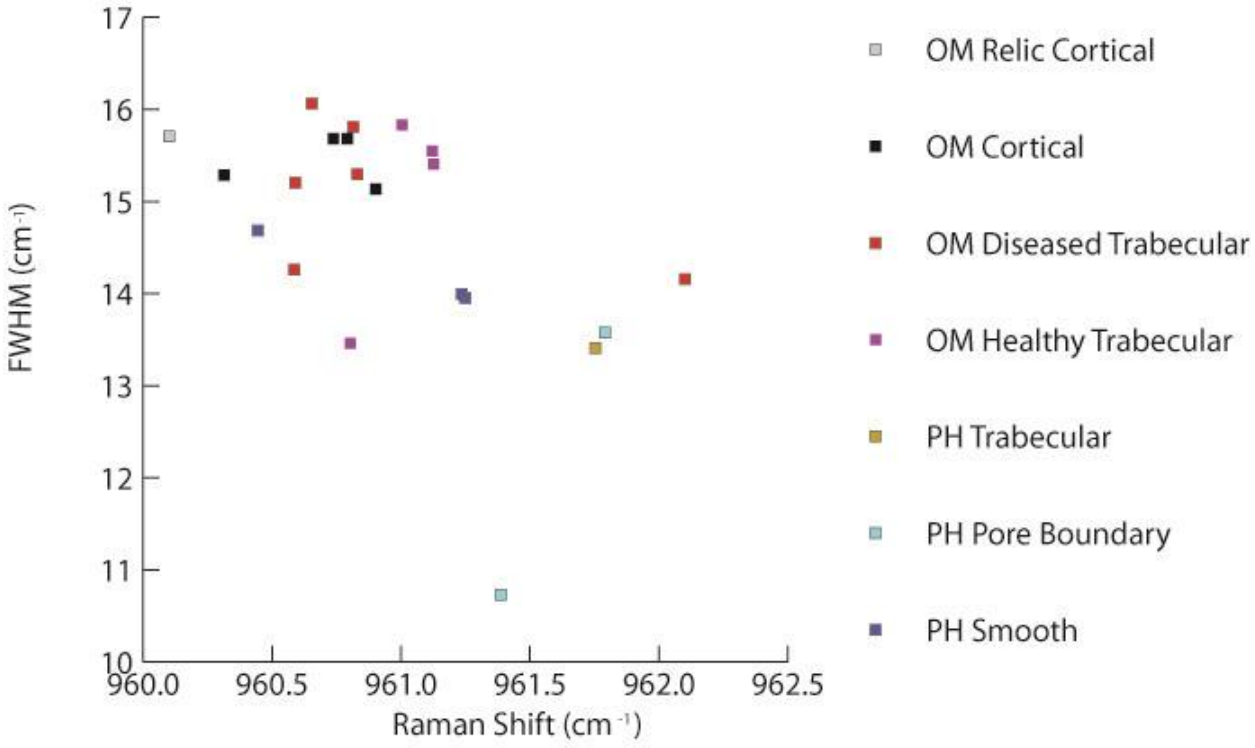

Figure 35: Full width at half maximum (FWHM) and band position data for the ν_1 P-O symmetric stretching mode of the PO_4^{3-} tetrahedron in apatite from an artiodactyl tibia presenting with osteomyelitis and a human skull presenting with porotic hyperostosis (KUNHM, teaching collection). PH = Porotic hyperostosis, OM = Osteomyelitis.

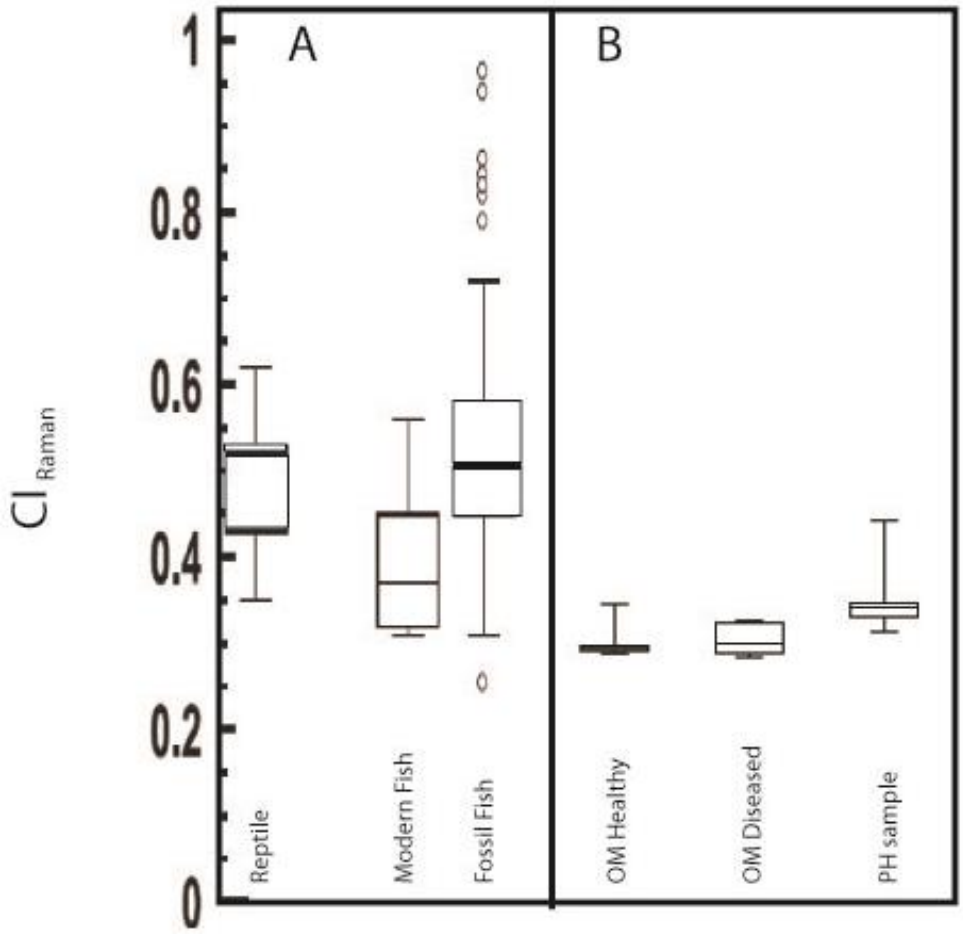

Figure 36: Representation of Crystallinity Index ($_{Raman)}$ of biogenic apatite samples according to different categories. CI_{Raman} relates the crystallinity of a sample to that of an average magmatic apatite, based on the Full Width at Half Maximum of the ν_1 P-O symmetric stretch mode of the PO_4^{3-} tetrahedron in apatite. Each box encloses 50% of the data with the median displayed as a line. The top and bottom lines represent +/- 25% limits for values which fall within an acceptable range, with circles indicating outliers. A. Data presented in Pucéat et al. (2004), collected with 514.5 and 632.8 nm lasers. B. Data derived from this study, collected with a 785 nm laser. OM = Osteomyelitis sample (KUNHM, teaching collection) PH = Porotic hyperostosis sample (KUNHM, teaching collection).

Table 1. Parameters for collection of Raman spectra.

Sample	Power level	# of Accumulations	Accumulation time
Porotic Hyperostosis	1-10%	1-20	10-30 s
Osteomyelitis	1-10%	10-20	10-20 s
Urolith	0.5-1%	10	10-15 s

Table 2. Deconvoluted band positions and Full Width at Half Maximum (FWHM) values for the v_1 P-O symmetric stretch mode of the PO_4^{3-} tetrahedron in apatite mode in apatite present in a human skull presenting with porotic hyperostosis (KUNHM, teaching collection). Crystallinity $Index_{Raman}$ was calculated following the procedure of Pucéat et al. (2004).

Location	Power level	Accumulation Time	# of Accumulations	Band position (Δ cm^{-1})	FWHM (cm^{-1})	Crystallinity $Index_{Raman}$
1	10%	10 s	15	960.44383	14.687331	0.334
2	5%	20 s	1	961.24865	13.951475	0.351
3	1%	30 s	15	961.79055	13.577273	0.361
4	1%	15 s	20	961.38708	10.729376	0.457
5	1%	10 s	20	961.75406	13.409069	0.365

Table 3. Band positions and Full Width at Half Maxima (FWHM) for the ν_1 P-O symmetric stretch mode of the PO_4^{3-} tetrahedron in apatite present in an artiodactyl tibia presenting with osteomyelitis (KUNHM, teaching collection). Crystallinity $Index_{Raman}$ was calculated following the procedure of Pucéat et al. (2004).

Location	Power level	Accumulation Time	# of Accumulations	Band position (Δ cm^{-1})	FWHM (cm^{-1})	Crystallinity $Index_{Raman}$
1	10%	10 s	10	960.90271	15.136623	0.324
2	10%	10 s	15	960.31307	15.285491	0.321
3	10%	10 s	15	960.5895	15.204006	0.322
3	5%	10 s	15	960.58655	14.26195	0.344
4	10%	10 s	15	960.10043	15.708059	0.312
5	10%	10 s	15	960.81351	15.80805	0.310
6	1%	20 s	20	962.10163	14.155305	0.346
7	10%	10 s	15	960.73844	15.683642	0.312
7	10%	10 s	15	960.79264	15.682471	0.312
8	5%	10 s	15	960.65441	16.062717	0.305
9	10%	10 s	10	960.82996	15.298276	0.320
10	10%	10 s	10	961.00358	15.833583	0.309
10	5%	10 s	10	960.80255	13.463846	0.364
11	10%	10 s	15	961.12143	15.547474	0.315
11	10%	10 s	15	961.12654	15.408178	0.318

Table 4. Relative intensities of the ν_1 P-O symmetric stretch mode of the PO_4^{3-} tetrahedron in apatite to the ν_1 P-O symmetric stretch mode of the PO_4^{3-} tetrahedron in dicalcium phosphate dihydrate for a human skull presenting with porotic hyperostosis (KUNHM, teaching collection).

Location	Power level	Accumulation Time	# of Accumulations	Ratio of ~960 Δ cm^{-1} band intensity to ~985 Δ cm^{-1} band intensity
1	10%	10 s	15	15.22
2	5%	20 s	1	6.598
3	1%	30 s	15	0.362
4	1%	15 s	20	0.738
5	1%	10 s	20	0.352

Acknowledgements

Funding was provided for this project through the Paleontological Society's Ellis L. Yochelson award. I would like to acknowledge Randol Wehrbein and Craig Marshall for assistance with Raman spectroscopy and data processing, Lenore Barbian for facilitating examination of the AFIP collection she curates and to David Burnham and Ali Nabavizadeh for image development of the urolith. I would also like to acknowledge Bruce Rothschild for helpful comments on chapter 3.

Special thanks are extended to Alison Olcott Marshall for guidance throughout this project.

Appendix I

Konservat-Lagerstätten from deltaic and brackish environments.

DEPOSIT	AGE	ENVIRONMENT	PRIMARY MODE OF PRESERVATION	EXAMPLE REFERENCES	LOCATION
Gilboa	Devonian	Deltaic	Sandstone casts of plants, Flexible organic compressions	Allison and Briggs, 1991b	USA
Rhenish Massif (Alken, Hombach)	Devonian	Deltaic	Dark/shiny impressions associated with pyrite	Wehrmann et al., 2010	Germany
Bear Gulch	Carboniferous	Brackish/ deltaic	organic remains, phosphatic and cartiligenous fossils, molds	Williams, 1983	USA
Blanzy Montceau	Carboniferous	Lacustrine or Deltaic	Siderite nodules	Allison and Briggs, 1991b	France
Carbondale Gp (Linton Fm Mecca and Logan quarries)	Carboniferous	Swamp/ Deltaic	Calcified cartilage fragments, cartilage fragments	Rigby and von Bitter, 2005	USA
Castlecomer Fauna	Carboniferous	Brackish or freshwater (swamp/ estuary)	Carbonaceous compressions (cuticle)	Orr et al., 2008	Ireland
Glencartholm	Carboniferous	Deltaic	Organic residues, bones	Allison and Briggs, 1991b	UK
Granton	Carboniferous	Deltaic	Phosphatized	Allison, 1988b	UK
Hamilton	Carboniferous	Estuary/ Deltaic	Articulated skeletons with dark carbonized bacterial film outlining fossil	Allison and Briggs, 1991b	USA
Mazon Creek/ Francis Creek	Carboniferous	Deltaic	Molds in siderite concretions	Selden and Nudds, 2004	USA
Grès à Voltzia	Triassic	Deltaic	Phosphatized	Selden and Nudds, 2004	France

Additional References:

Orr, P.J., Briggs, D.E.G., Kearns, S.L., 2008. Taphonomy of Exceptionally Preserved Crustaceans from the Upper Carboniferous of Southeastern Ireland. Palaios 23, 298-312.

Rigby, J., von Bitter, P., 2005. Sponges and associated fossils from the Pennsylvanian

Carbondale Formation of northwestern Illinois. Journal of Paleontology 79, 460-468.

Wehrmann, A., Wilde, V., Schindler, E., Brocke, R., Schultka, S., 2010. High resolution facies analysis of a Lower Devonian deltaic marine-terrestrial transition (Nellenköpfchen Formation, Rheinisches Schiefergebirge, Germany): implications for small-scale fluctuations of coastal environments. Neues Jahrbuch für Geologie und Paläontologie - Abhandlungen 256, 317-334.

Williams, L.A., 1983. Deposition of the Bear Gulch Limestone - a Carboniferous Plattenkalk From Central Montana. Sedimentology 30, 843-860.

Appendix II

Representative *Konservat-Lagerstätten* from lacustrine and riverine environments

DEPOSIT	AGE	ENVIRONMENT	PRIMARY MODE OF PRESERVATION	EXAMPLE REFERENCE	LOCATION
Achanarras	Devonian	Lacustrine	Dark Carbonaceous film	Newman, 2003	UK
Canowindra	Devonian	Lacustrine or Riverine	Impressions	Johnson, 2009	Australia
Rhynie Chert	Devonian	Lacustrine or Riverine	Silicification or coalified then silicified	Selden and Nudds, 2004	UK
Blanzy Montceau	Carboniferous	Lacustrine or Deltaic	Siderite nodules	Allison and Briggs, 1991b	France
East Kirkton	Carboniferous	Lacustrine	Organic residues	Allison and Briggs, 1991a	UK
Odernheim (Meisenheim Fm)	Permian	Lacustrine	Articulated skeletons and calcified cartilage, only calcified tissue preserved	Sanchez et al., 2010	Germany
Culpeper (Bull Run Fm)	Triassic	Lacustrine	Impressions	Gore, 1986	USA
Solite Quarry	Triassic	Shallow Lacustrine	Silvery compressions; articulated skeletons with impressions of soft tissue	Fraser et al., 1996	USA
Crato	Cretaceous	Lacustrine	Phosphatized, Pyritized (oxidized to Goethite)	Selden and Nudds, 2004	Brazil
Jehol Biota (Yixian and Jiufotang fm)	Cretaceous	Lacustrine and Terrestrial Lahars	Pyritized, Articulated skeletons surrounded by carbonaceous dark stain	Jiang et al., 2011; Wang et al., 2012	China
Montsech	Cretaceous	Lacustrine	Presumed organic (not well studied) and molds	Allison and Briggs, 1991b	Spain
Geiseltal	Eocene	Lacustrine	Siliceous	Allison and Briggs, 1991a	Germany
Green River	Eocene	Lacustrine	Impressions/soft tissue outlines	Allison and Briggs, 1991a	USA

Messel	Eocene	Lacustrine	Skeletal with bacterial films fossilized in siderite	Allison and Briggs, 1991a; O'Brien et al., 2008	Germany
Horsefly	Eocene	Lacustrine	No published taphonomic data found	Allison and Briggs, 1991b	Canada
Bechlejovice	Oligocene	Lacustrine	Skeleton enclosed in a black carbonaceous outline	McNamara et al., 2010	Czech Republic
Canyon Ferry	Oligocene	Lacustrine	Compressions and impressions in diatomaceous mats or ash	O'Brien et al., 2008	USA
Enspel	Oligocene	Lacustrine	Skeleton enclosed in a carbonaceous bacterial film with multiple mineralogies	O'Brien et al., 2008	Germany
Florissant	Oligocene	Lacustrine	Compressions and impressions in diatomaceous mats or ash	Allison and Briggs, 1991b	USA
Rott	Oligocene-Miocene	Lacustrine	No published taphonomic data found	Petrulevičius et al., 2011	Germany
Barstow	Miocene	Lacustrine	Microcrystalline silica	Allison and Briggs, 1991b	USA
Clarkia	Miocene	Lacustrine	Compressions with nearly unaltered plant biochemistry	Allison and Briggs, 1991b	USA
Foulden Maar (Otego)	Miocene	Lacustrine	Carbonaceous compressions of plants; articulated fish	Lindqvist and Lee, 2009	New Zealand
Libros	Miocene	Lacustrine	Skeleton enclosed in a black carbonaceous outline - sulphurization	McNamara et al., 2009	Spain
Ribesalbes	Miocene	Lacustrine	Skeleton enclosed in a black carbonaceous outline - sulphurization	McNamara et al., 2010	Spain
Shanwang	Miocene	Lacustrine	Carbonaceous plant	O'Brien et al., 2008	China

			compressions; skeletons with dark shadows of carbonaceous remains		
Kabutoiwa	Miocene	Lacustrine	No published taphonomic data found	Allison and Briggs, 1991b	Japan
Oeningen	Miocene	Lacustrine	No published taphonomic data found	Allison and Briggs, 1991b	Germany
Banks Island	Miocene/Pliocene	Riverine	3D Conifers, in situ labile biomolecules	Witkowski et al., 2012	Canada
Willershausen	Pliocene	Lacustrine	Calcium carbonate concretions containing intact or nearly intact arthropod cuticle	Allison and Briggs, 1991b	Germany
Shiobara	Pleistocene	Lacustrine	Skeleton enclosed in a black carbonaceous outline	McNamara et al., 2010	Japan

Additional References:

Fraser, N., Grimaldi, D., Olsen, P. and Axsmith, B., 1996. A Triassic Lagerstatte from eastern North America. Nature 380, 615-619.

Gore, P.J.W., 1986. Triassic Notostracans in the Newark Supergroup, Culpeper Basin, Northern Virginia. Journal of Paleontology 60, 1086-1096.

Jiang, B., Fürsich, F. T., Sha, J., Wang, B., and Niu, Y., 2011. Early Cretaceous volcanism and its impact on fossil preservation in Western Liaoning, NE China. Palaeogeography, Palaeoclimatology, Palaeoecology 302, 255-269.

Johnson, D., 2009. The Geology of Australia. Cambridge University Press, Port Melbourne.

Lindqvist, J.K., and Lee, D.E., 2009. High-frequency paleoclimate signals from Foulden Maar, Waipiata Volcanic Field, southern New Zealand: An Early Miocene varved lacustrine diatomite deposit. Sedimentary Geology 222, 98-110.

McNamara, M.E., Orr, P.J., Kearns, S.L., Alcala, L., Anadon, P., Molla, E.P., 2009. Soft-Tissue Preservation in Miocene Frogs from Libros, Spain: Insights into the Genesis of Decay Microenvironments. Palaios 24, 104-117.

McNamara, M., Orr, P.J., Kearns, S.L., Alcala, L., Anadon, P., Penalver-Molla, E., 2010. Organic preservation of fossil musculature with ultracellular detail. Publications of the Royal Society B-Biological Sciences 277, 423-427.

Newman, M.J., 2003. A new naked jawless vertebrate from the Middle Devonian of Scotland. Palaeontology 45, 933-941.

O'Brien, N.R., Meyer, H.W.and Harding, I.C., 2008. The role of biofilms in fossil preservation, Florissant Formation, Colorado. Geological Society of America Special Papers 435, 19-31.

Petrulevičius, J.F., Wappler, T., Nel, A., Rust, J., 2011. The diversity of Odonata and their endophytic ovipositions from the Upper Oligocene Fossillagerstätte of Rott (Rhineland, Germany). ZooKeys 130, 67-89.

Sanchez, S., De Ricqlès, A., Schoch, R. & Steyer, J. S. 2010. Developmental plasticity of limb bone microstructural organization in Apateon: histological evidence of paedomorphic conditions in branchiosaurs. Evolution & Development 12, 315-328.

Wang, B., Zhao, F.C., Zhang, H.C., Fang, Y., Zheng, D.R., 2012. Widespread Pyritization of Insects in the Early Cretaceous Jehol Biota. Palaios 27, 708-712.

Witkowski, C., Gupta, N.S., Yang, H., Leng, Q., Williams, C.J., Briggs, D.E.G., Summons, R.E., 2012. Molecular Preservation of Cenozoic Conifer Fossil Lagerstatten from Banks Island, the Canadian Arctic. Palaios 27, 279-287.

Appendix III

Precambrian *Konservat-Lagerstätten*

DEPOSIT	AGE	ENVIRONMENT	PRIMARY MODE OF PRESERVATION	EXAMPLE REFERENCE	LOCATION
Lakhanda	Tonian	Marine	BST	German and Podkovyrov, 2011	Russia
Miroedikha	Tonian	Marine	BST	Butterfield, 1995	Russia
Wynniatt	Cryogenian	Marine	BST	Butterfield, 1995	Canada
Liuliobei/Juliaquo	Cryogenian	Marine	BST	Butterfield, 1995	China
Svanbergfjellet	Cryogenian	Marine	BST	Butterfield, 2004	Svalbard
Algeria	Ediacaran	Marine	Impressions	Narbonne, 1998; Bertrand-Sarfati et al., 1995	Algeria
Amadeus Basin (Inc. Deep Well and Laura Creek)	Ediacaran	Marine	Impressions	Narbonne, 1998	Australia
Arkhangelsk Region (Onega Peninsula, near Syuzma, near the White Sea)	Ediacaran	Marine	Impressions	Grazhdankin, 2004	Russia
Avalon Penninsula (St. John Group, Newfoundland)	Ediacaran	Marine	Impressions	Allison and Briggs, 1991a	Canada
Briscal Fm	Ediacaran	Marine	Impressions	Bottjer, 2002	Canada
Cariboo Mountains (Isaac Fm)	Ediacaran	Marine	Impressions	Narbonne, 1998	Canada
Charnwood Forest	Ediacaran	Marine	Impressions	Narbonne, 2005	UK
Conception Group (Newfoundland)	Ediacaran	Marine	Impressions	Narbonne, 2005	Canada
Denying (Dengying, excluding Gaojiashan member described below)	Ediacaran	Marine	Diagenetic calcspars, Possible BST	Anderson et al., 2011; Shen et al., 2009	China
Doushantuo	Ediacaran	Marine	Phosphatized	Xiao et al., 1998	China
Drook Fm (Newfoundland, Below Mistaken	Ediacaran	Marine	Impressions	Narbonne, 2005; Narbonne and	Canada

Point)				Gehling, 2003	
Ediacara Hills (Flinders Ranges, Rawnsley Quartzite)	Ediacaran	Marine	Impressions	Allison and Briggs, 1991a	Australia
Fermeuse Fm. (Newfoundland)	Ediacaran	Marine	Impressions	Narbonne, 2005	Canada
Gaojiashan (a member of the Dengying Fm)	Ediacaran	Marine	Pyritized, BST	Cai et al., 2012	China
Great Basin (Wood Canyon Fm and Stirling quartzite, Death Valley, Montgomery Mountains, Nopah Range, Funeral Mountains, Resting Springs and Spring Mountains)	Ediacaran	Marine	Impressions	Hagadorn and Waggoner, 2000	USA
Innerelv Member (Finnmark)	Ediacaran	Marine	Impressions	Narbonne, 2005	Norway
Khatyspyt Fm. (Olenek, Siberia)	Ediacaran	Marine	Molds and "taphonomic phantoms" of carbonaceous films	Grazhdankin et al., 2008	Russia
Miaohe (Duoshantuo)	Ediacaran	Marine	Algae carbonaceous compressions; mold/cast	Xiao et al., 2002	China
Mistaken Point Fm	Ediacaran	Marine	Impressions	Allison and Briggs, 1991a	Canada
Mt. Skinner	Ediacaran	Marine	Impressions and casts	Narbonne, 1998	Australia
Namibia (Nama group, Kuibis and Schwarzrand subgroups, Huns Member)	Ediacaran	Marine	Molds/casts	Narbonne, 1998	Namibia
Sonora	Ediacaran	Marine	Impressions	McMenamin, 1996	Mexico
Podolia (Bernashev member, Valdai, Mogilev Fm, Yampol beds, Dzhurzhev mbr, Nagoryany Fm.)	Ediacaran	Marine	Impressions	Narbonne, 1998	Ukraine
Sheepbed Fm. (Sekwi Brook)	Ediacaran	Marine	Impressions	Narbonne, 1998	Canada
Trepassey Fm	Ediacaran	Marine	Impressions	Bottjer, 2002	Canada

Verkhovka Fm (Near White Sea)	Ediacaran	Marine	Impressions	Narbonne, 2005	Russia
Windermere Supergroup (Twitya Fm, Goz siltstone, Miette group, McKenzie Mountains, Rocky Mountains, Wernecke Mountains)	Ediacaran	Marine	Impressions	Narbonne, 2005	Canada
Urals (Riphean)	Ediacaran	Marine	No published taphonomic data found	Narbonne, 1998	Russia
Yenisey River (Igarka-Turukhansk)	Ediacaran	Marine	No published taphonomic data found	Narbonne, 1998	Russia

Additional References:

Bertrand-Sarfati, J., Moussine-Pouchkine, A., Amard, B. and Ahmed, A.A.K., 1995. First Ediacaran fauna found in western Africa and evidence for an Early Cambrian glaciation. Geology 23, 133-136.

Bottjer, D.J., 2002. Enigmatic Ediacaran fossils: Ancestors or Aliens?, in: Bottjer, D.J., Etter, W., Hagadorn, J.W. and Tang, C.M. (Ed.), Exceptional Fossil Preservation: A Unique View on the Evolution of Marine Life Columbia University Press, New York.

Butterfield, N.J., 2004. A vaucheriacean alga from the middle Neoproterozoic of Spitsbergen: implications for the evolution of Proterozoic eukaryotes and the Cambrian explosion. Paleobiology 30, 231-252.

German, T.N., Podkovyrov, V.N., 2011. The role of cyanobacteria in the assemblage of the Lakhanda Microbiota. Paleontological Journal 45, 320-332.

Grazhdankin, D., 2004. Patterns of distribution in the Ediacaran biotas: facies versus biogeography and evolution. Paleobiology 30, 203-221.

Grazhdankin, D.V., Balthasar, U., Nagovitsin, K.E., Kochnev, B.B., 2008. Carbonate-hosted Avalon-type fossils in arctic Siberia. Geology 36, 803-806.

McMenamin, M.A.S., 1996. Ediacaran biota from Sonora, Mexico. Proceedings of the National Academy of Science, USA 93, 4990-4993.

Narbonne, G.M., Gehling, J., 2003. Life after snowball: The oldest complex Ediacaran fossils. Geology 31, 27-30.

Shen, B., Xiao, S., Zhou, C., Yuan, X., 2009. Yangtziramulus zhangi New genus and species, a carbonate-hosted macrofossil from the Ediacaran Dengying Formation in the Yangtze Gorges area, South China. Journal of Paleontology 83, 575-587.

Xiao, S., Yuan, X., Steiner, M., Knoll, A.H., 2002. Macroscopic carbonaceous compressions in a terminal Proterozoic shale: A systematic reassessment of the Miaohe biota, south China. Journal of Paleontology 76, 347-376.

Xiao, S., Zhang, Y. and Knoll, A.H., 1998. Three-dimensional preservation of algae and animal embryos in a Neoproterozoic phosphorite. Nature 391, 553-558.

Appendix IV

Rate of *Konservat-Lagerstätten* formation and

estimated marine sulfate concentration with data ranges

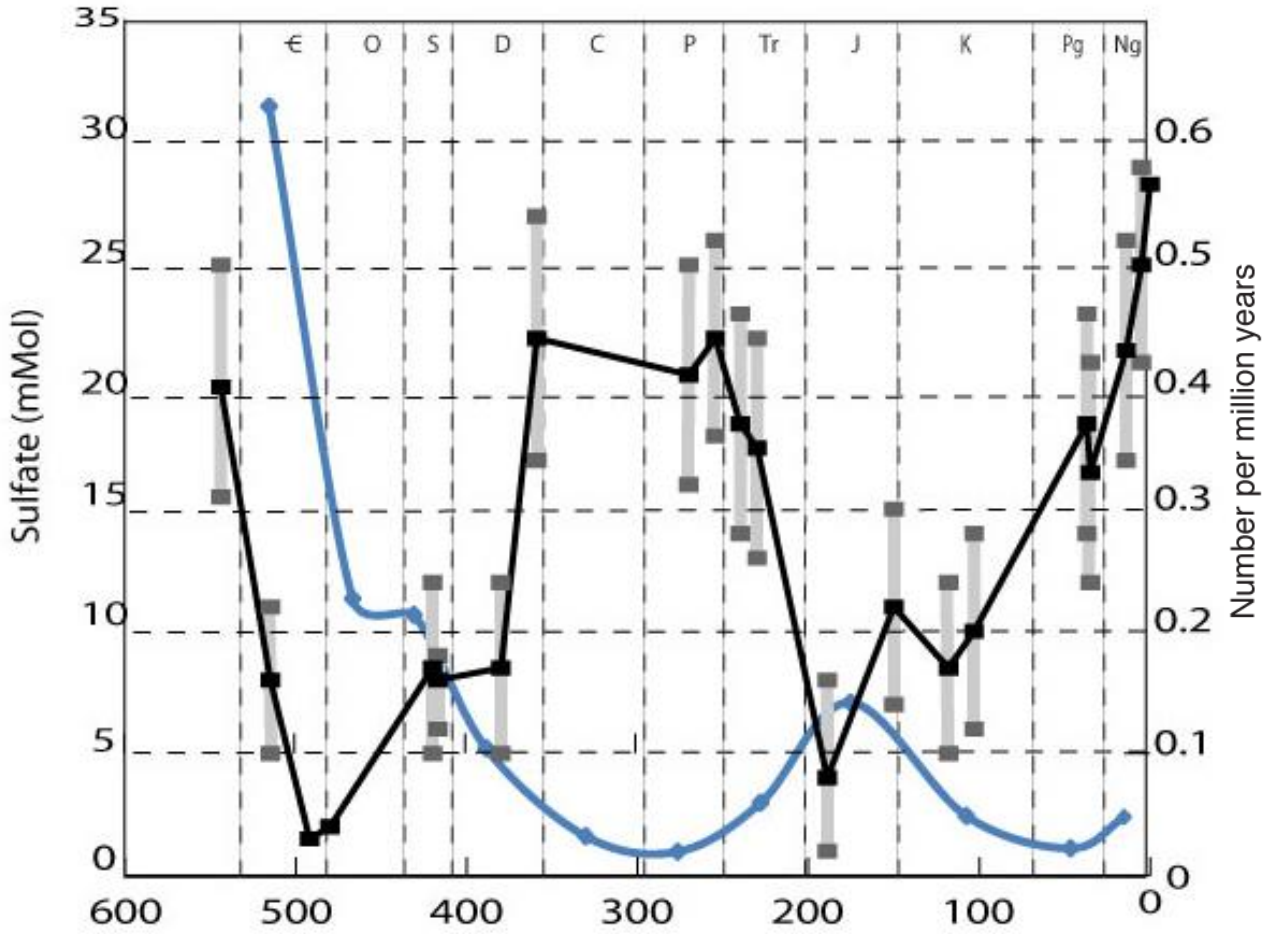

Figure A-IV 1: Rate of *Konservat-Lagerstätten* formation (black) and estimated marine sulfate concentration (blue). Ranges for observed sulfate data are indicated in gray. Data from Lowenstein et al., 2003 (some data previously reported in Horita et al., 2002), Gill et al., 2007, Newton et al., 2010 , Gill et al., 2011 and Thompson and Kah, 2012.

Appendix V

2nd Derivative plots for Raman Spectra obtained from an artiodactyl tibia suffering from osteomyelitis (KU Natural History Museum, teaching collection).

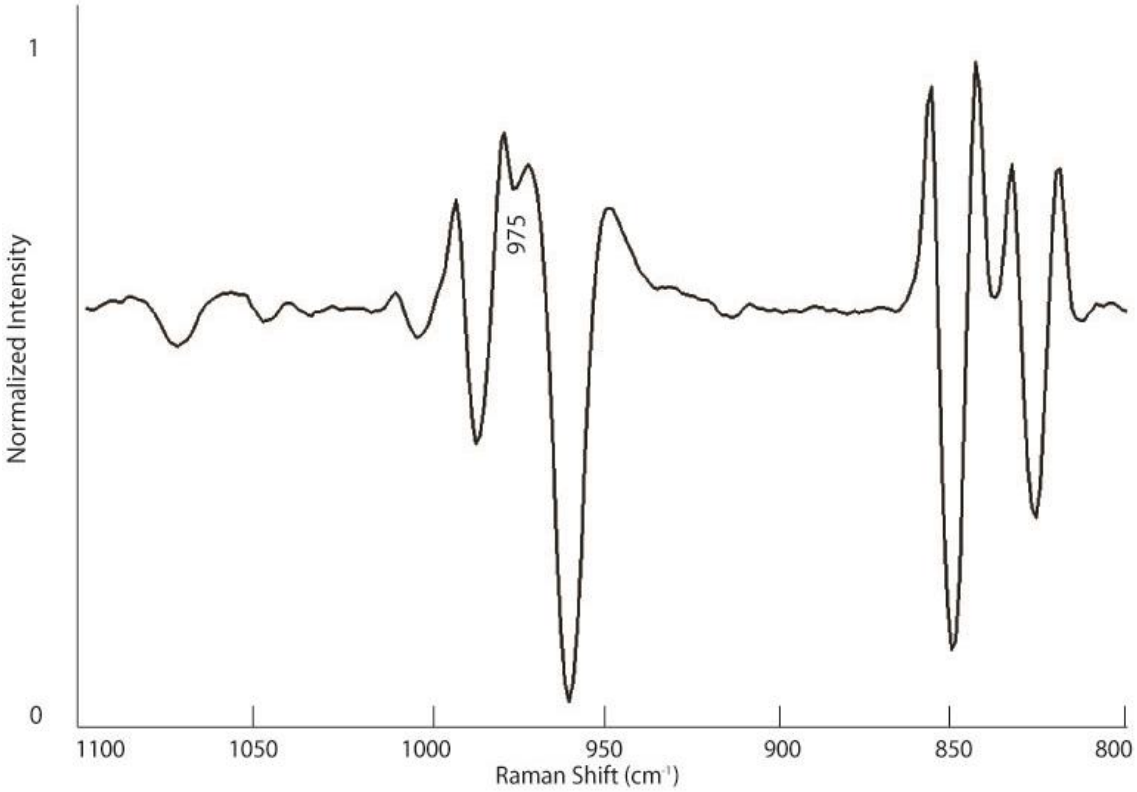

Site 1. Scans were collected with a 785 nm laser at 30 mW focused with a 20x refractive glass objective lens for 10 accumulations lasting 10 s. Baseline corrections were performed in GRAMS/AI version 8 using a multi-point linear level only function before 2nd Derivative plots were generated in GRAMS/Ai version 8.

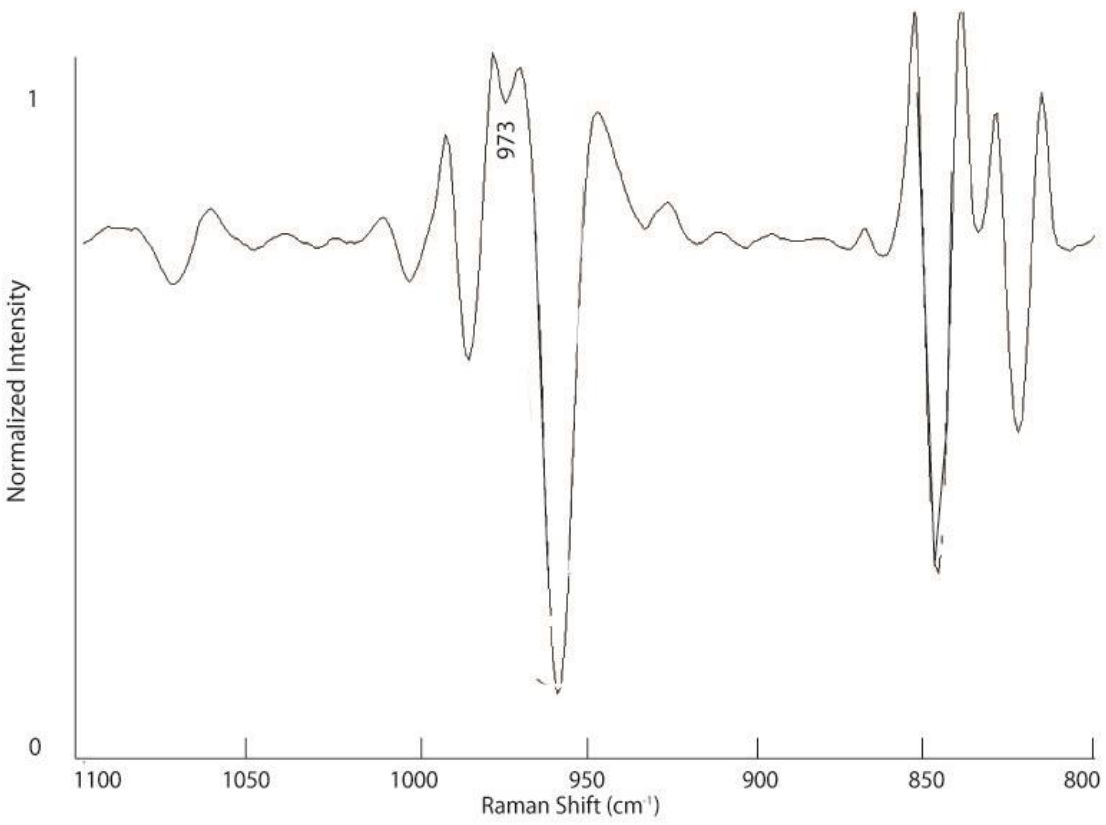

Site 2. Scans were collected with a 785 nm laser at 30 mW focused with a 20x refractive glass objective lens for 15 accumulations lasting 10 s. Baseline corrections were performed in GRAMS/AI version 8 using a multi-point linear level only function before 2nd Derivative plots were generated in GRAMS/Ai version 8.

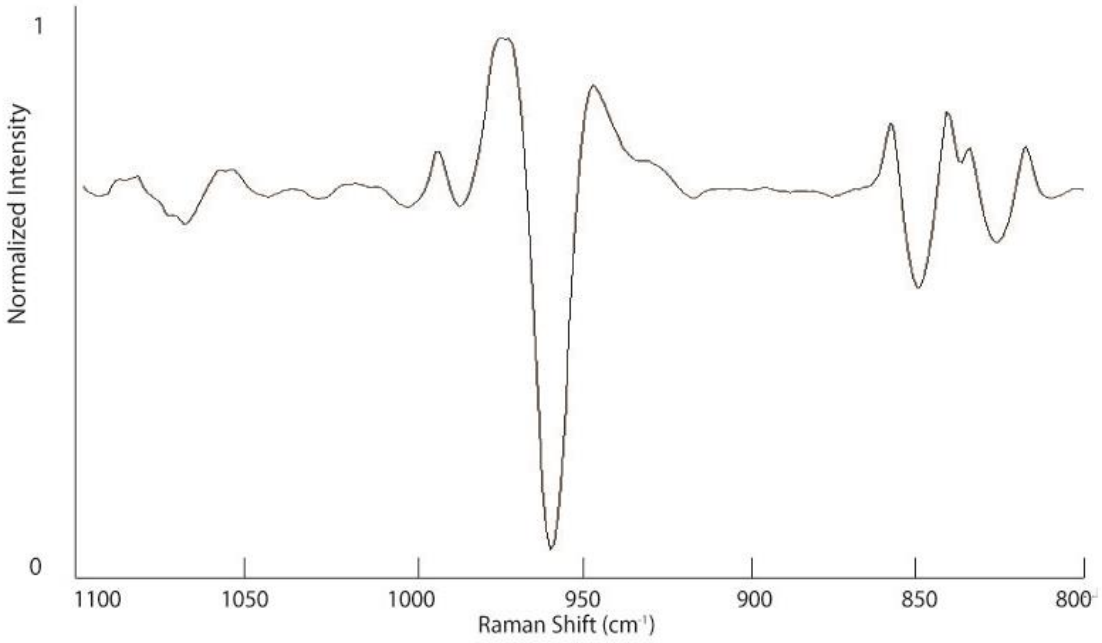

Site 7. Scans were collected with a 785 nm laser at 30 mW focused with a 20x refractive glass objective lens for 15 accumulations lasting 10 s. Baseline corrections were performed in GRAMS/AI version 8 using a multi-point linear level only function before 2nd Derivative plots were generated in GRAMS/Ai version 8.

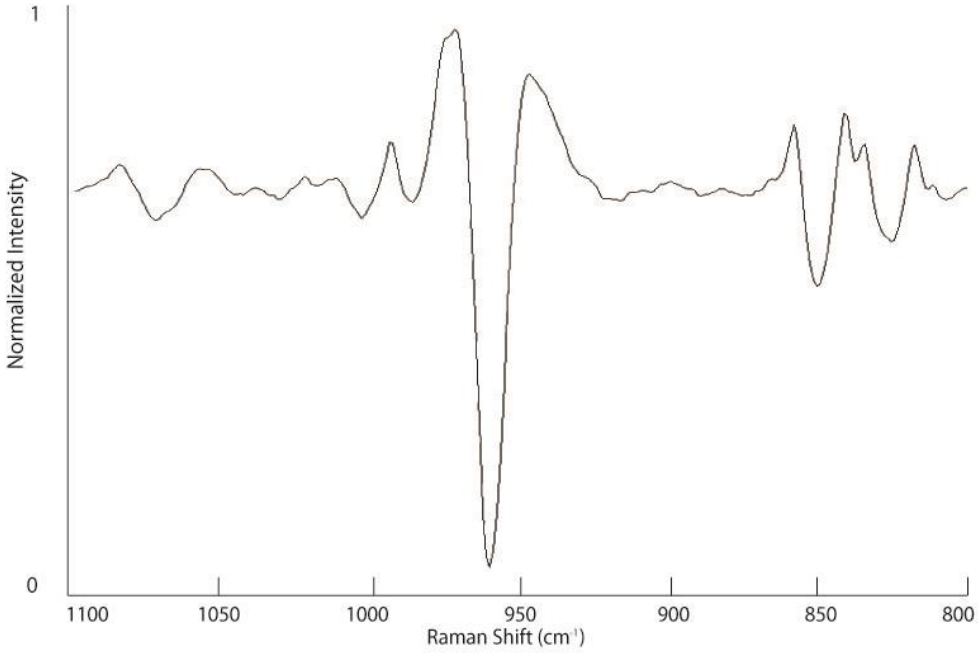

Site 9. Scans were collected with a 785 nm laser at 30 mW focused with a 20x refractive glass objective lens for 10 accumulations lasting 10 s. Baseline corrections were performed in GRAMS/AI version 8 using a multi-point linear level only function before 2nd Derivative plots were generated in GRAMS/Ai version 8.

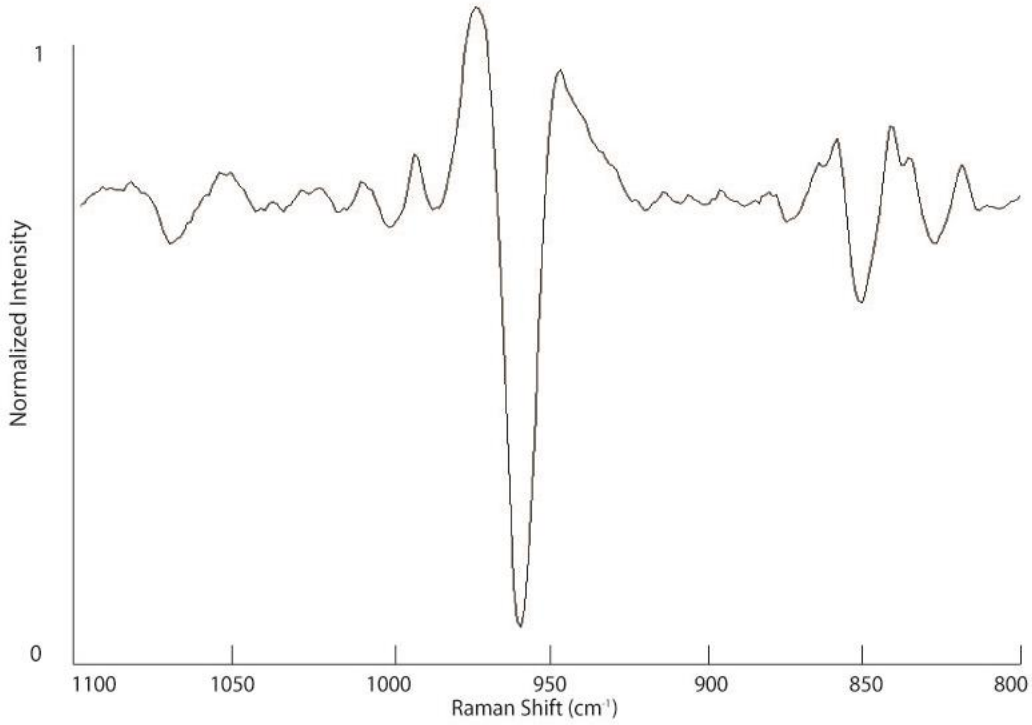

Site 10. Scans were collected with a 785 nm laser at 30 mW focused with a 20x refractive glass objective lens for 15 accumulations lasting 10 s. Baseline corrections were performed in GRAMS/AI version 8 using a multi-point linear level only function before 2nd Derivative plots were generated in GRAMS/Ai version 8.

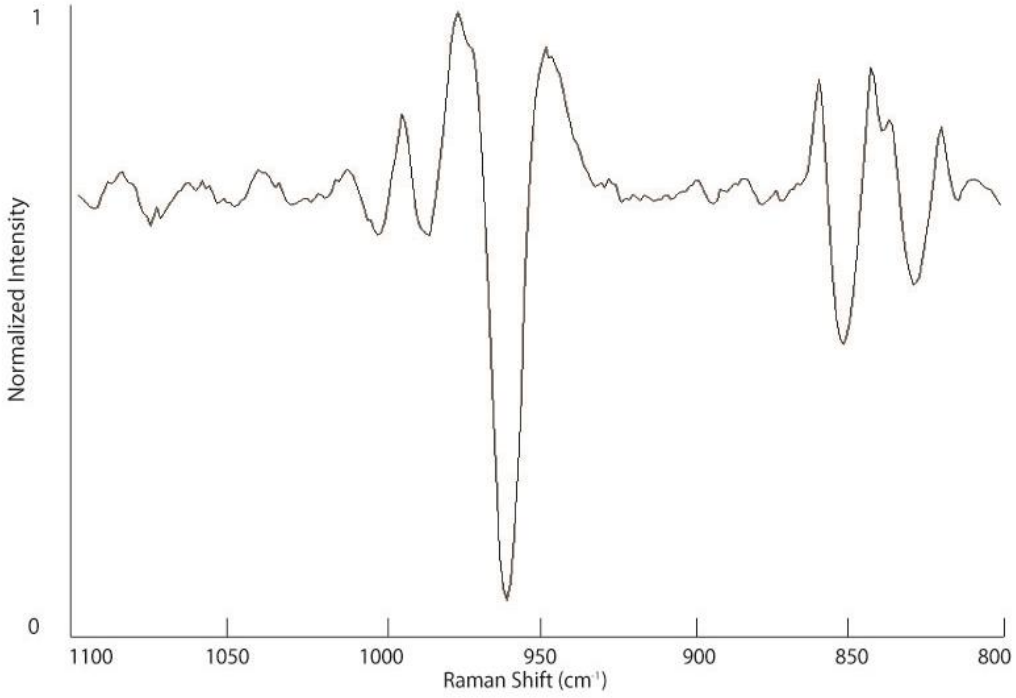

Site 11. Scans were collected with a 785 nm laser at 30 mW focused with a 20x refractive glass objective lens for 15 accumulations lasting 10 s. Baseline corrections were performed in GRAMS/AI version 8 using a multi-point linear level only function before 2nd Derivative plots were generated in GRAMS/Ai version 8.

Appendix VI

Differential diagnosis for non-uniform, non-spherical calcific masses

Location	Description	Consideration
Rim		Nephrocalcinosis
		Intracystic (within bladder wall) cancer
		Echinococcus
		Calcified abscess
		Mesenteric cyst
		Ureteral
		Vascular calcification
Central		
	Irregular	Renal cell carcinoma
		Osteosarcoma
		Metastatic cancer
	Wedge-Shaped	Papillary necrosis
	Amorphous	Tuberculosis
		Leiomyoma
		Carcinoid
		Dermoid cyst
		Calcified ovarian fibroma
		Fecolith
	Linear	Shistosomiasis
	Staghorn	Infection
		Xanthogranulomatosis

Modified from Rothschild et al., in review. Derived from Dyer et al., 1998 and Komar and Buikstra, 2003.

Additional References:

Komar, D., Buikstra, J.E., 2003. Differential diagnosis of a prehistoric biological object from the Koster (Illinois) site. International Journal of Osteoarchaeology 13, 157-164.